Investigating the effects of *Bacillus subtilis* endospore surface reactivity on low-temperature aqueous geochemical systems

Zoë R. Harrold

A dissertation

submitted in partial fulfillment of the

requirements for the degree of

Doctor of Philosophy

University of Washington

2014

Reading Committee:

Drew Gorman-Lewis, Ph.D., Chair

Ronald Sletten, Ph.D.

Bruce Nelson, Ph.D.

Program Authorized to Offer Degree:

Earth and Space Science

University of Washington

ABSTRACT

Investigating the effect of *Bacillus subtilis* endospore surface reactivity
on low-temperature aqueous geochemical systems

Zoë R. Harrold

Chair of the Supervisory Committee:
Drew Gorman-Lewis, Ph.D.
Earth and Space Sciences

Microbes are a ubiquitous component in water-rock systems including ground and surface waters, soils, mid-ocean ridge hydrothermal systems, and deep sedimentary basins. Microbial envelopes provide complex organic surfaces that serve as a physical interface between cellular and geochemical processes and thus represent a confluence of the bio-, hydro- and litho-spheres. As an intrinsic component in water-rock systems, microbes have the capacity to influence geochemical cycling in their surroundings through surface mediated pathways. This dissertation utilizes *Bacillus subtilis* endospores, a metabolically dormant cell type, to isolate and quantify the effects of bacterial endospore surfaces on low-temperature aqueous geochemical processes including ion adsorption and silicate weathering rates.

Chapter 2 outlines novel methods describing *B. subtilis* endospore growth and harvesting as well as a quality control technique enabling quantification of endospore harvest purity using bright-field and fluorescence microscopy imaging in conjunction with automated cell counting software. The resultant average endospore purity was 88±11% (1σ error, n=22) with a median value of 93%.

Chapter 3 couples potentiometric titration and isothermal titration calorimetry (ITC) analyses to quantify *B. subtilis* endospore-proton adsorption. We modeled the potentiometric titration and ITC data using four- and five-site non-electrostatic surface complexation models (NE-SCM). Log Ks and site concentrations describing endospore surface protonation are statistically equivalent to *B. subtilis* cell surface protonation constants while enthalpies are more exothermic. The thermodynamic parameters defined in this study provide insight on molecular scale spore surface protonation reactions and provide a robust chemical framework for modeling and predicting endospore-metal adsorption behavior in systems not directly studied in the lab.

Chapter 4 investigates the *B. subtilis* endospore adsorption capacity of two major elements: magnesium (Mg) and silica (Si). We measure Mg and Si adsorption as a function of solution pH, adsorbate to adsorbent ratio and in systems containing both Mg and Si. NE-SCMs described in Chapter 3 provide a framework for modeling endospore-Mg. Mg adsorption to the endospore surface increases with increasing pH, adsorbent to adsorbate ratio and high concentrations of total Si. Si adsorption was negligible under all conditions studied. These findings suggest direct endospore-Mg adsorption is more likely to influence geochemical processes than endospore- Si adsorption.

In Chapter 5, *B. subtilis* endospores are used to isolate and quantify the effects of bacterial surface reactivity on the rate of forsterite (Mg_2SiO_4) dissolution at circumneutral pH. Assays utilizing homogeneous and dialysis bound mineral powder compare the influence of direct, spore-mineral and indirect, spore-ion interactions on forsterite dissolution rate. We show that endospore surface reactivity enhances forsterite dissolution rates through both direct and indirect pathways and as a function of endospore concentration.

To my grandmother, Frances Rhodes,

and my mother and father, Yvonne and James Harrold

ACKNOWLEDGEMENTS

I would like to express my deepest gratitude to Dr. Drew Gorman-Lewis for his guidance and support over the course of my Ph.D. Dr. Gorman-Lewis' expertise in surface reactivity and creative approach to experimentation is further complimented by his patient-, humble- and positive-nature. I am truly fortunate to have learned from and worked with such an adept scientist and could not have asked for a better mentor to lead me through the Ph.D. process.

I would also like to thank my committee members Dr. Ronald Sletten and Dr. Bruce Nelson for their support over the years. The opportunity to serve as a field-assistant in Greenland under Dr. Sletten provided me with a renewed interest in academia and inspired my ongoing curiosity for sub-glacial geomicrobiology and polar research. Dr. Nelson's encouragement and enthusiasm for my work have provided me with a sense of excitement for research and have been instrumental to my success at the University of Washington. Feedback and suggestions from both Dr. Sletten and Dr. Nelson helped make this body of work a success. I would also like to recognize Dr. John Baross, my Graduate School Representative, for his thoughtful contributions and readiness to help.

Additional thanks to my brothers, David and Andrew Harrold, for helping me find humor and light in all things; to my extended family for all their encouragement; and to my grandmother, Frances Rhodes, whose adventurous life as a pioneer for women's progress has inspired me since childhood. Finally, I would like to thank my parents, James and Yvonne Harrold, for their unending support over the past 28 years. It is with their guidance and encouragement that I have learned to seek out and find excitement in challenging endeavours.

Table of Contents

LIST OF FIGURES

LIST OF TABLES

Chapter 1: Introduction

Microbes are intrinsic to nearly all water-rock systems including soils (Siala et al., 1974), ground-water (Alfreider et al., 1997), deep-sea hydrothermal vents (Sogin et al., 2006), hot springs (Phoenix et al., 2003), subglacial lakes (Skidmore, 2011) and even the driest environments such as the Atacama Desert (Barros et al., 2008). Whitman et al. (1998) estimate the global abundance of prokaryotes ranges from 4-6 x 10^{30} cells and is equivalent to 60 -100 % of total terrestrial plant biomass. Unlike terrestrial plants and other multicellular organisms, however, the physiology of single celled microbes effectively maximizes their surface area to volume ratio. This configuration evolved in part to facilitate the exchange of nutrients and waste products between the cell and surrounding medium. The repercussions of microbial physiology go beyond cellular efficiency by providing a highly reactive, complex organic surface in most environmental media. Chemical reactions occurring at the cell wall have the capacity to promote or inhibit bacterial metabolism and thus viability as well as directly affect aqueous geochemical processes occurring within the hydro- and lithospheres. Consequently, the microbial surface serves as the physical interface between cellular and geochemical processes and represents a physical confluence of the bio-, hydro- and lithospheres. Understanding how and to what extent bacterial cell walls influence geochemical processes is integral to grasping the impact of microbes on regional and global geochemical cycles.

Extensive research over the past 30 years has expanded our understanding of vegetative cell-surface reactivity (e.g. Alessi and Fein, 2010; Beveridge and Murray, 1980; Borrok et al., 2004; Gorman-Lewis et al., 2006). Studies of *Bacillus subtilis*, a model gram-positive bacterial species, have provided a detailed structural model of the primary polymer making up the gram-positive cell wall, peptidoglycan. Other components of bacterial cell walls include lipopolysacharides, proteins and techoic acids. Each of these cell wall components hosts an array of proton active organic acid moieties also known as functional groups. The capacity and

pH range of cell surface proton adsorption is typically determined via potentiometric titration (e.g. Borrok et al., 2004; Fein et al., 2005). Data for a variety of bacterial species indicate cell surface protonation occurs over a range of environmentally relevant, alkaline to acidic, pH. Complimentary calorimetric data, which measures the heat of protonation, provides a measure of protonation enthalpies (Gorman-Lewis et al., 2006). The development of surface complexation models based on balance chemical equations and their application to bacterial surface protonation has enabled the deconvolution of potentiometric titration and calorimetric data (e.g. Gorman-Lewis et al., 2006). Results of these studies provide valuable insight on the chemical identity of proton active organic acid moieties on the cell surface. Commonalities between the surfaces of a variety of bacterial species include the presence of carboxyl and phosphate groups (e.g. Beveridge and Murray, 1980; Borrok et al., 2005; Gorman-Lewis et al., 2006; Kelly et al., 2001). Findings also indicate the presence of proton active hydroxyl, amine and sulfhydryl moieties (Cox et al., 1999; Fein et al., 2005; Pokrovsky et al., 2008).

Some members within the Firmicute phylum, including the Bacillus and Clostridium genera, are capable of forming a metabolically dormant cell-type known as endospores. Endospores function to preserve the bacterium DNA when cells are exposed to environmental stresses such as low nutrient supplies or desiccation (Nicholson, 2002). It is likely that endospores are a common and perhaps prolific component of natural microbial consortia due to temporal and spatial variations in a variety of environmental parameters, such as periodic wetting and drying and irregular nutrient fluxes, that make cellular growth unfavorable. Indeed, a study by Siala et al. (1974) showed endospores constituted up to 50 % of the microbial population in an acidic soil sample. Endospore formers and their endospores have been identified in a range of environments including soils (Hong et al., 2009; Siala et al., 1974), regoliths, rock varnishes and aqueous systems (e.g. Nicholson, 2002). Despite their prevalence and our detailed understanding of vegetative cell surface adsorption, the surface reactivity of bacterial endospores is poorly constrained. This dissertation provides a detailed investigation of

endospore surface reactivity by isolating *B. subtilis* endospores and measuring and modeling their surface reactivity, major element adsorption potential and influence on forsterite mineral dissolution rate.

Unlike the vegetative cell surface, endospores are enveloped within a tough proteinaceous coat. This coat is one of the many defense mechanisms enabling endospores to persist in unfavorable conditions (Driks, 1999, 2002; Nicholson et al., 2002). The number and composition of proteins within the coat varies across endospore species and as a function of growth medium (Driks, 2002). Endospore surface reactivity is likely associated with the proton active functional groups of amino acids making up coat proteins. The most prevalent amino acids within the *B. subtilis* endospore coat are glutamic acid, aspartic acid, cysteine, lysine and tyrosine (Bhattacharyya and Bose, 1967; Pandey and Aronson, 1979). Glutamic and aspartic acid both host carboxyl functional groups while cysteine, lysine and tyrosine host thiol, amine and phenol functional groups, respectively. The reactivity of organic acid moieties within a protein structure can be heavily influenced by the tertiary and quaternary structures of the protein (Li et al., 2005; Thurlkill et al., 2006). Proton active amino acid functional groups embedded deep within a complex protein may even be rendered unreactive with respect to the bulk solution. It is therefore necessary to study endospore surface reactivity to determine which organic acid functional groups interact with and adsorb aqueous species.

Our current understanding of endospore surface reactivity is limited to a few studies regarding surface protonation and metal adsorption. Electrophoretic mobility studies for a variety of endospores report the development of a negatively charged surface electric field with increasing solution pH, suggesting deprotonation of organic acid moieties like those found on vegetative cell surfaces (Douglas, 1954, 1957). Potentiometric titration data for marine *Bacillus* sp. SG-1 indicate surface protonation occurs over a pH range loosely corresponding to the pK_a of carboxyl and phosphate groups (He and Tebo, 1998). He and Tebo (1998) show endospores of the marine *Bacillus* species SG-1 are capable of adsorbing Cu. Revis et al. (1997) measured Pb,

Hg, Cr, As, Cd, Ba and Sr adsorption onto *B. megaterium* endospores. Soft lewis acids such as Hg and Pb exhibited a higher adsorption affinity with the *B. megaterium* endospore surface (Revis et al., 1997). These findings may indicate the presence of adsorption sites characterized as soft lewis bases, such as sulfhydryl groups, in accordance with hard and soft, Lewis acid and base (HSAB) theory, where soft (hard) acids form stronger bonds with soft (hard) bases. Most research investigating endospore-metal interactions, however, focuses on their ability to irreversibly oxidize Mn(II) and precipitate Mn(IV)-oxides (e.g. Bargar et al., 2000; Francis and Tebo, 2002). The chemical identity of organic acid moieties responsible for endospore adsorption is largely unknown.

Endospore surfaces exhibit hydrophobic properties in addition to the presence of charged, hydrophilic reactive sites. Two-phase separatory solutions effectively isolate endospores from their vegetative cell counterpart by concentrating them in an organic top phase. The partitioning of endospores into the organic phase indicates the endospore surface is more hydrophobic than vegetative cells (Doyle et al., 1984; Sacks and Alderton, 1961). Endospores also adhere better to both hydrophobic and hydrophilic surfaces than their vegetative cell counterparts (Rönner et al., 1990). Consequently, it is possible that both hydrophobic and hydrophilic reactions drive endospore surface adsorption. This chemical dichotomy makes endospore surfaces an intriguing and complex component in water-rock systems.

Investigating endospore surface reactivity requires milligrams of pure biomass free of cells and cell lysis products capable of adsorbing H^+ and metals. Challenges associated with endospore growth and isolation pose a barrier to focused endospore surface reactivity studies. Bacterial endospores develop within a host cell when exposed to unfavorable conditions (Gould and Hurst, 1969). Growing cultures under such conditions can inhibit initial cellular growth and lead to small biomass yields. Other approaches require multiple aseptic additions and the transfer of established cultures into sporulation medium (Donnellan et al., 1964); processes that

increases the risk of culture contamination. Further complications arise after sporulated cells undergo lysis and release large quantities of potentially reactive cellular material into suspension. Incomplete sporulation results in vegetative cell contamination. Chapter 2 of this dissertation provides a method for *B. subtilis* endospore growth and isolation with a semi-automated approach for determining the purity of an endospore harvest. These methods enable research regarding endospore surface reactivity by providing a substantial endospore biomass with low cell contamination. Ch. 2 is published in the Journal of Microbiological Methods (Harrold et al., 2011). Methodology contributions and manuscript edits from Dr. Drew Gorman-Lewis as well as extensive lab assistance from Mikaela Hertel helped make this paper a success.

Chapter 3 addresses our lack of knowledge regarding endospore surface reactivity by coupling potentiometric titration and isothermal titration calorimetry data describing *B. subtilis* endospore surface protonation. Results from potentiometric titration data are processed based on the proton mass balance of the system and modeled according to non-electrostatic surface complexation modeling (NE-SCM) theory. NE-SCMs are built on balanced chemical equations describing discrete adsorption sites on the adsorbate surface. This modeling approach is ideal for describing the reactivity of complex surfaces such as the endospore coat, where a range of organic acid moieties with varying pK_a values are likely responsible for surface protonation behavior. NE-SCM model outputs include best-fit reactive site concentrations and log K values corresponding to discrete reactive sites on the endospore surface. Parallel calorimetric data are modeled based on the protonation NE-SCM and constrain the enthalpies and entropies of protonation for each discrete site. Best-fit log K values, enthalpies and entropies describing discrete protonation sites provide thermodynamic constraints on the chemical identity of adsorption sites on the endospore surface. NE-SCMs are also applicable to macro-scale systems not directly studied in the laboratory, unlike commonly used empirical models, such as distribution coefficients (K_D) (Bethke and Brady, 2000). Results from Ch. 3 provide the most robust chemical description of the organic acid moieties responsible for *B. subtilis* endospore

surface reactivity to date. This work is published in Geochimica et Cosmochimica Acta (Harrold and Gorman-Lewis, 2013). Dr. Drew Gorman-Lewis provided significant contributions and support regarding experimental design, mathematical modeling approach and manuscript editing, all of which contributed to the success of this publication.

The reactivity of microbial surfaces extends beyond protonation to include elemental and molecular adsorption reactions. The nature of these reactions depends on the chemical identity of surface bound organic acid moieties and the adsorbing species. Surface complexation reactions between aqueous components and the cell surface include both inner-sphere and outer-sphere complexes. Surface complexes may also be characterized by ionic or covalent bond formation. The presence of multiple aqueous elemental or molecular components can lead to complex speciation or ternary complexes that enhance or inhibit cell surface adsorption (Alessi and Fein, 2010; Gorman-Lewis et al., 2005). Geochemical factors influencing cell wall adsorption include, but are not limited to, ionic strength, pH of the aqueous medium and the presence of other chelators (e.g. Borrok and Fein, 2005; Fein and Delea, 1999; Gorman-Lewis et al., 2005). Such adsorption reactions have the capacity to concentrate and alter the aqueous activities of trace and major elements.

Many fundamental low-temperature aqueous geochemical processes are driven by the activities of major elements. Aqueous silica (Si) and common metals such as iron (Fe), magnesium (Mg) and calcium (Ca) are among the most important major elements associated with both primary mineral dissolution and a wide range of secondary precipitates. Major cations such as Mg^{2+} and Ca^{2+} readily adsorb to a range of microbial surfaces while direct silica adsorption onto the *B. subtilis* cell wall is negligible. Iron oxide coated microbial surfaces, however, support subsequent silica adsorption (Fein et al., 2002). Other researches have also indicated ternary metal-silica adsorption complexes as the main driver of microbial-silica adsorption (Urrutia and Beveridge, 1993; Urrutia and Beveridge, 1994). These findings corroborate the silicic or clay-like coatings found on *in situ* microbes, which develop in

association with iron oxides (Konhauser et al., 1993; Konhauser et al., 1994; Urrutia and Beveridge, 1994). Surface based mineral precipitation may contribute to microfossil formation and microbial preservation in the geologic record.

Chapter 4 investigates the affinity of *B. subtilis* endospore –Si and –Mg adsorption to better evaluate the influence of endospores on low-temperature aqueous geochemical systems and compare their surface reactivity to vegetative cells. This body of work assesses Mg and Si adsorption over a wide range of pH and adsorbent to adsorbate ratios as well as adsorption behavior in aqueous systems containing both Mg and Si. Mg –endospore adsorption data is modeled based on the NE-SCM described in Ch. 3.

The rate of primary mineral dissolution is a fundamental low-temperature aqueous geochemical process capable of both controlling and being controlled by the activity of aqueous major ions. Organic acids, such as those identified on the endospore surface, have the capacity to enhance primary silicate dissolution rates (e.g. Bennett et al., 1988; Olsen and Rimstidt, 2008). Dissolution rate enhancement occurs through direct, organic acid- mineral surface adhesion by binding with the mineral and lowering the activation energy of dissolution (e.g. Bennett, 1991; Olsen and Rimstidt, 2008). Indirect pathways increase dissolution kinetics when organic acids complex with and lower the activity of mineral dissolution products, shifting the chemical system further from equilibrium (Bennett et al., 1988; Hutchens et al., 2006).

Traditionally viewed as an abiotic process, mineral dissolution is now known to increase in the presence of microbes (e.g. Rogers and Bennett, 2004). Microbially enhanced dissolution is primarily associated with metabolic processes or the production and release of organic acids. Studies investigating the effect of microbes on mineral dissolution rate, however, inherently include any effects associated with microbial surface reactivity. The few studies aimed at isolating the effects of microbial surface reactivity on mineral dissolution rates encountered significant complications associated with cellular metabolism and cell lysis (Lee and Fein, 2000;

Pokrovsky et al., 2009; Wightman and Fein, 2004). The affect of microbial cell surface reactivity on mineral dissolution rate remains enigmatic.

Endospores are an ideal candidate for isolating the effects of microbial surface reactivity on mineral dissolution rate due to their metabolic dormancy and structural integrity in the absence of nutrients. Chapter 5 utilizes *B. subtilis* endospores as a tool for quantifying both direct and indirect influences of microbial surface reactivity on the rate of forsterite (Mg_2SiO_4) dissolution. Similarities between endospore and cell surface reactivity, determined in Ch. 3 and 4, make *B. subtilis* endospores a first order proxy for a wide range of vegetative cells. Results from Chapter 5 have implications regarding microbe-mineral interactions in a wide range of microbe-water-rock systems. Manuscript feedback in addition to experimental and analytical advice from Dr. Drew Gorman-Lewis was instrumental to the formulation of Chapters 4 and 5. Chapters 4 and 5 are slated for submission to a peer-reviewed journal within the year.

References

Alessi, D.S., Fein, J.B., 2010. Cadmium adsorption to mixtures of soil components: Testing the component additivity approach. Chemical Geology 270, 186-195.

Alfreider, A., Krossbacher, M., Psenner, R., 1997. Groundwater samples do not reflect bacterial densities and activity in subsurface systems. Water Research 31, 832-840.

Bargar, J.R., Tebo, B.M., Villinski, J.E., 2000. In situ characterization of Mn(II) oxidation by spores of the marine Bacillus sp strain SG-1. Geochimica Et Cosmochimica Acta 64, 2775-2778.

Barros, N., Feijóo, S., Salgado, J., Ramajo, B., García, J.R., Hansen, L.D., 2008. The Dry Limit of Microbial Life in the Atacama Desert Revealed by Calorimetric Approaches. Engineering in Life Sciences 8, 477-486.

Bennett, P.C., 1991. Quartz dissolution in organic-rich aqueous systems. Geochimica et Cosmochimica Acta 55, 1781-1797.

Bennett, P.C., Melcer, M.E., Siegel, D.I., Hassett, J.P., 1988. The dissolution of quartz in dilute aqueous solutions of organic acids at 25°C. Geochimica et Cosmochimica Acta 52, 1521-1530.

Bethke, C.M., Brady, P.V., 2000. How the Kd Approach Undermines Ground Water Cleanup. Ground Water 38, 435-443.

Beveridge, T.J., Murray, R.G., 1980. Sites of metal deposition in the cell wall of Bacillus subtilis. Journal of Bacteriology 141, 876-887.

Bhattacharyya, P., Bose, S.K., 1967. Amino acid composition of cell wall and spore coat of Bacillus subtilis in relation to mycobacillin production. Journal of Bacteriology 94, 2079-2080.

Borrok, D., Fein, J.B., Kulpa, C.F., 2004. Proton and Cd adsorption onto natural bacterial consortia: Testing universal adsorption behavior. Geochimica Et Cosmochimica Acta 68, 3231-3238.

Borrok, D., Turner, B.F., Fein, J.B., 2005. A universal surface complexation framework for modeling proton binding onto bacterial surfaces in geologic settings. Am J Sci 305, 826-853.

Borrok, D.M., Fein, J.B., 2005. The impact of ionic strength on the adsorption of protons, Pb, Cd, and Sr onto the surfaces of Gram negative bacteria: testing non-electrostatic, diffuse, and triple-layer models. Journal of Colloid and Interface Science 286, 110-126.

Cox, J.S., Smith, D.S., Warren, L.A., Ferris, F.G., 1999. Characterizing Heterogeneous Bacterial Surface Functional Groups Using Discrete Affinity Spectra for Proton Binding. Environmental Science & Technology 33, 4514-4521.

Donnellan, J.E., Jr., Nags, E.H., Levinson, H.S., 1964. Chemicall defined, synthetis media for sporulation and for germination and growth of *Bacillus subtilis*. Journal of Bacteriology 87, 332-336.

Douglas, H.W., 1954. Electrophoretic Studies on Bacterial Spores.

Douglas, H.W., 1957. Electrophoretic studies on spores and vegitative cells of certain strains of B. *megaterium*, B. *subtilis*, and B. *cereus*. Journal of applied Bacteriology 20, 390-403.

Doyle, R.J., Nedjat-Haiem, F., Singh, J.S., 1984. Hydrophobic characteristics ofBacillus spores. Current Microbiology 10, 329-332.

Driks, A., 1999. Bacillus subtilis spore coat. Microbiology and Molecular Biology Reviews 63, 1-20.

Driks, A., 2002. Maximum shields: the assembly and function of the bacterial spore coat. Trends in Microbiology 10, 251-254.

Fein, J.B., Boily, J.-F., Yee, N., Gorman-Lewis, D., Turner, B.F., 2005. Potentiometric titrations of Bacillus subtilis cells to low pH and a comparison of modeling approaches. Geochimica et Cosmochimica Acta 69, 1123-1132.

Fein, J.B., Delea, D., 1999. Experimental study of the effect of EDTA on Cd adsorption by Bacillus subtilis: a test of the chemical equilibrium approach. Chemical Geology 161, 375-383.

Fein, J.B., Scott, S., Rivera, N., 2002. The effect of Fe on Si adsorption by Bacillus subtilis cell walls: insights into non-metabolic bacterial precipitation of silicate minerals. Chemical Geology 182, 265-273.

Francis, C.A., Tebo, B.M., 2002. Enzymatic Manganese(II) Oxidation by Metabolically Dormant Spores of Diverse Bacillus Species. Appl. Environ. Microbiol. 68, 874-880.

Gorman-Lewis, D., Elias, P.E., Fein, J.B., 2005. Adsorption of Aqueous Uranyl Complexes onto Bacillus subtilis Cells. Environmental Science & Technology 39, 4906-4912.

Gorman-Lewis, D., Fein, J.B., Jensen, M.P., 2006. Enthalpies and entropies of proton and cadmium adsorption onto Bacillus subtilis bacterial cells from calorimetric measurements. Geochimica et Cosmochimica Acta 70, 4862-4873.

Gould, G.W., Hurst, A., 1969. The bacterial spore. Academic Press, London, New York,.

Harrold, Z.R., Gorman-Lewis, D., 2013. Thermodynamic analysis of Bacillus subtilis endospore protonation using isothermal titration calorimetry. Geochimica et Cosmochimica Acta 109, 296-305.

Harrold, Z.R., Hertel, M.R., Gorman-Lewis, D., 2011. Optimizing Bacillus subtilis spore isolation and quantifying spore harvest purity. Journal of Microbiological Methods 87, 325-329.

He, L.M., Tebo, B.M., 1998. Surface charge properties of and Cu(II) adsorption by spores of the marine Bacillus sp. strain SG-1. Applied and Environmental Microbiology 64, 1123-1129.

Hong, H.A., To, E., Fakhry, S., Baccigalupi, L., Ricca, E., Cutting, S.M., 2009. Defining the natural habitat of Bacillus spore-formers. Research in Microbiology 160, 375-379.

Hutchens, E., Valsami-Jones, E., Harouiya, N., Charat, C., Oelkers, E.H., McEldoney, S., 2006. An Experimental Investigation of the Effect of *Bacillus megaterium* on Apatite Dissolution. Geomicrobiology Journal 23, 177 - 182.

Kelly, S.D., Boyanov, M.I., Bunker, B.A., Fein, J.B., Fowle, D.A., Yee, N., Kemner, K.M., 2001. XAFS determination of the bacterial cell wall functional groups responsible for complexation of Cd and U as a function of pH. Journal of Synchrotron Radiation 8, 946-948.

Konhauser, K.O., Fyfe, W.S., Ferris, F.G., Beveridge, T.J., 1993. Metal sorption and mineral precipitation by bacteria in two Amazonian river systems: Rio Solimoes and Rio Negro, Brazil. Geology 21, 1103-1106.

Konhauser, K.O., Schultze-Lam, S., Ferris, F.G., Fyfe, W.S., Longstaffe, F.J., Beveridge, T.J., 1994. Mineral precipitation by epilithic biofilms in the speed river, ontario, Canada. Appl Environ Microbiol 60, 549-553.

Lee, J.-U., Fein, J.B., 2000. Experimental study of the effects of Bacillus subtilis on gibbsite dissolution rates under near-neutral pH and nutrient-poor conditions. Chemical Geology 166, 193-202.

Li, H., Robertson, A.D., Jensen, J.H., 2005. Very fast empirical prediction and rationalization of protein pKa values. Proteins: Structure, Function, and Bioinformatics 61, 704-721.

Nicholson, W.L., 2002. Roles of Bacillus endospores in the environment. Cellular and Molecular Life Sciences 59, 410-416.

Nicholson, W.L., Fajardo-Cavazos, P., Rebeil, R., Slieman, T.A., Riesenman, P.J., Law, J.F., Xue, Y.M., 2002. Bacterial endospores and their significance in stress resistance. Antonie Van Leeuwenhoek International Journal of General and Molecular Microbiology 81, 27-32.

Olsen, A.A., Rimstidt, D.J., 2008. Oxalate-promoted forsterite dissolution at low pH. Geochimica et Cosmochimica Acta 72, 1758-1766.

Pandey, N.K., Aronson, A.I., 1979. Properties of the *Bacillus subtilis* spore coat. Journal of Bacteriology 137, 1208-1218.

Phoenix, V.R., Konhauser, K.O., Ferris, F.G., 2003. Experimental study of iron and silica immobilization by bacteria in mixed Fe-Si systems: implications for microbial silicification in hot springs. Canadian Journal of Earth Sciences 40, 1669-1678.

Pokrovsky, O.S., Pokrovski, G.S., Feurtet-Mazel, A., 2008. A structural study of cadmium interaction with aquatic microorganisms. Environmental Science & Technology 42, 5527-5533.

Pokrovsky, O.S., Shirokova, L.S., Bezeneth, P., Schott, J., Golubev, S.V., 2009. Effect of organic ligands and heterotrophic bacteria on wollastonite dissolution kinetics. American Journal of Science 309, 731-772.

Revis, N.W., Hadden, C.T., Edenborn, H., 1997. Removal of dissolved heavy metals and radionuclides by microbial spores, Proceedings: VI International World Congress on Waste Management, p. 14.

Rogers, J.R., Bennett, P.C., 2004. Mineral stimulation of subsurface microorganisms: release of limiting nutrients from silicates. Chemical Geology 203, 91-108.

Rönner, U., Husmark, U., Henriksson, A., 1990. Adhesion of bacillus spores in relation to hydrophobicity. Journal of Applied Microbiology 69, 550-556.

Sacks, L.E., Alderton, G., 1961. Behavior of bacterial spores in aqueous polymer two-phase systems. Journal of Bacteriology 82, 331-341.

Siala, A., Hill, I.R., Gray, T.R.G., 1974. Populations of Spore-forming Bacteria in an Acid Forest Soil, with Special Reference to Bacillus subtilis. J Gen Microbiol 81, 183-190.

Skidmore, M., 2011. Microbial communities in Antarctic subglacial aquatic environments. Geophysical Monograph Series 192, 61-81.

Sogin, M.L., Morrison, H.G., Huber, J.A., Welch, D.M., Huse, S.M., Neal, P.R., Arrieta, J.M., Herndl, G.J., 2006. Microbial diversity in the deep sea and the underexplored "rare biosphere". Proceedings of the National Academy of Sciences 103, 12115-12120.

Thurlkill, R.L., Grimsley, G.R., Scholtz, J.M., Pace, C.N., 2006. pK values of the ionizable groups of proteins. Protein Science 15, 1214-1218.

Urrutia, M.M., Beveridge, T.J., 1993. Mechanism of silicate binding to the bacterial cell wall in *Bacillus subtilis*. Journal of Bacteriology 175, 1936-1945.

Urrutia, M.M., Beveridge, T.J., 1994. Formation of fine-grained metal and silicate precipitates on a bacterial surface (*Bacillus subtilis*). Chemical Geology 116, 261-280.

Whitman, W.B., Coleman, D.C., Wiebe, W.J., 1998. Prokaryotes: The unseen majority. Proceedings of the National Academy of Sciences 95, 6578-6583.

Wightman, P.G., Fein, J.B., 2004. The effect of bacterial cell wall adsorption on mineral solubilities. Chemical Geology 212, 247-254.

Chapter 2: Optimizing *Bacillus subtilis* spore isolation and quantifying spore harvest purity

2.1 Abstract

Investigating the biochemistry, resilience and environmental interactions of bacterial endospores often requires a pure endospore biomass free of vegetative cells. Numerous spore isolation methods, however, neglect to quantify the purity of the final endospore biomass. To ensure low vegetative cell contamination we develop a quality control technique that enables rapid quantification of endospore harvest purity. This method quantifies spore purity using brightfield and fluorescence microscopy imaging in conjunction with automated cell counting software. We applied this method to *Bacillus subtilis* endospore harvests isolated using a two phase separation method that utilizes mild chemicals. The average spore purity of twenty-two harvests was 88 ± 11 % (error is 1σ) with a median value of 93 %. A spearman coefficient of 0.97 correlating automated and manual bacterial counts confirms the accuracy of software generated data.

2.2 Introduction

Bacterial endospores are ubiquitous in the environment, play an integral role in the bacterial life cycle and may influence biogeochemical cycles (De Vrind et al., 1986; He and Tebo, 1998; Nicholson, 2002; Nicholson et al., 2002). Investigating the biochemistry, resilience and environmental interactions of endospores requires a pure endospore biomass free of vegetative cells. Unlike culturing vegetative cells, generating a pure bacterial endospore, here after referred to as spore, biomass that is free of vegetative cells, deemed “cells”, is more difficult. Complications arise when not all cells sporulate, the spore does not completely shed the

encasing cell material, or residual cell debris remains in the culture. Methods to produce a pure spore crop and quantify the amount of cell contamination in the final spore biomass are necessary for research including spore coat protein isolation, survival rates, spore germination triggers and surface reactions.

Numerous procedures have been used to address the issue of producing pure spore crops. These methods utilize special mediums that promote sporulation in bacterial cultures. Sporulation can be induced when endospore-forming bacteria become carbon, nitrogen and sometimes phosphorous limited, or when GTP concentrations are reduced (Harwood and Cutting, 1990). Nutrient limitation is achieved through natural exhaustion of the growth medium or by transferring cells to a nutrient limited sporulation broth. Defined, complex mediums requiring autoclaving, filtration and sterile additions are used to achieve bacterial sporulation in most methods. One exception is the commercially available Difco Sporulation Medium (Harwood and Cutting, 1990). Many of the accepted Multi-step sporulation medium preparations and cell transfer methods, however, can be time consuming and may increase the risk of culture contamination.

Many separation methods use chemicals such as lysozyme and EDTA to lyse cells and remove cellular material from the spore coat (Goldman and Tipper, 1978; He and Tebo, 1998; Rosson and Nealson, 1982). Recommendations for foam floatation include raising the suspension pH to 11.5 or an acetone treatment to facilitate *B. subtilis* spore separation (Boyles and Lincoln, 1958). While these techniques may suffice for some research goals, exposure to these chemicals and extreme pH may alter spore coat proteins or spore viability resulting in experimental errors.

A method devised by Sacks and Alderton (1961) utilizes mild chemicals to separate spores from cells based on the more hydrophobic behavior of spore surfaces. A two phase solution is generated using polyethylene glycol 4000 (PEG 4000) and a strong potassium phosphate buffer. In the suspension, spores are concentrated in the top organic (PEG 4000)

phase while cells and cell debris collect at the interface and in the bottom electrolyte. This separation process is ideal for investigations that require isolating a significant mass of spores without damaging the spore surface and removal of the separation solution by dilution and repeated washing. Sacks and Alderton (1961) recommend multiple additions and extractions of equilibrated PEG 4000 solution. While effective, the multiple extractions make this process very time and resource intensive. This separation technique is known to be successful; however, to our knowledge no work has been done to quantify its effectiveness.

Regardless of the separation method used it is likely that some residual vegetative cells contaminate the spore extracts. For many experiments it is prudent to determine the amount of cell contamination in each purified spore harvest. One method utilizes colony counts to determine spore versus cell partitioning. This technique involves heat treating a bacterial suspension to kill vegetative cells then incubating the suspension on agar plates to produce visible colonies which are then compared to colony counts from a non-heat treated suspension. Colony counts resulting from the untreated bacterial suspension correspond to total cell and spore counts, while heat treated plate counts are representative of viable spore concentrations (Siala et al., 1974). This technique is time consuming and dependent on cell and spore viability which may introduce errors in determining the degree of cell contamination in a purified spore biomass. Additional errors may arise from incomplete extermination of cells within the heat treated biomass. Despite the importance of spore purity for subsequent investigations many researchers neglect to conduct a thorough analysis quantifying the level of purity achieved in the final spore biomass and used in experiments (Boyles and Lincoln, 1958; He and Tebo, 1998; Revis et al., 1997; Rosson and Nealson, 1982; Sacks and Alderton, 1961).

In this research we utilize Tripticase Soy Broth (TSB), a commercially available growth medium, to generate a substantial *Bacillus subtilis* spore biomass. Spore isolation is achieved using Sacks and Alderton's (1961) two-phase extraction system for *B. subtilis* spore separation and streamlined by eliminating the need for additional organic phase extractions. To determine

the percent of spores within the purified spore biomass we develop a method to quantify cell contamination using the common Schaffer-Fulton (Schaeffer and Fulton, 1933) differential staining technique for spores and cells in conjunction with microscopy imaging and image processing.

2.3 Methods

2.3.1 Spore Separation

Bacillus subtilis cultures maintained on 3 % trypticase soy broth (TSB) and 0.5 % yeast extract agar plates were inoculated into test tubes with 3.5 ml of 3 % TSB and 0.5 % yeast extract. Following 24 h of incubation at 37 °C the cultures were transferred to 1 or 2 L volumes of 0.3 % TSB in a 1 tube to 1 L ratio. Large broth cultures were incubated at 37 °C for 6 d. On the sixth day the bacterial biomass was harvested via centrifugation at 6000 *g* for 15 m and transferred into 50 mL falcon tubes. The biomass was washed three times by suspending it in 30 mL of 0.1 M NaCl and vortexing for 1 m. Between each wash the biomass was pelleted by centrifugation at 10,000 *g* for 5 m and the supernatant discarded. Following the third wash, biomass from 1 L of growth was suspended in 5 ml of 18 MΩ cm^{-1} water.

15 ml of biomass suspension, equivalent to 3 L of biomass growth, was added to a two phase extraction system containing 11.18 % w/v PEG 4000, 34 % v/v 3M potassium phosphate buffer (1.76 M K_2HPO_4, 1.24 M KH_2PO_4) and 50 % v/v 18 MΩ cm^{-1} water (Sacks and Alderton, 1961) with a final volume of 200 mL. Sacks and Alderton (1961) observed particulates from the combined solutions collecting at the interface of the two-phase extraction system. Reagent filtration is recommended if the extraction requires a blank interface (Sacks and Alderton, 1961). Our procedure, however, avoids interface removal. Consequently, interfacial contamination was irrelevant and we did not filter the reagents.

To homogenize the two phases we mixed the solution vigorously for approximately 15 m and subsequently induced phase separation via centrifugation at 100 *g* for 2 m. A high concentration of *B. subtilis* spores collect in the top phase near the interface (Sacks and Alderton, 1961). We carefully siphoned off approximately 60 mL, or 80 %, of the top organic phase with a vacuum bulb to achieve maximum biomass while minimizing uptake of the interface.

We diluted the extracted top phase with 500 ml of de-ionized (DI) water and pelleted the spore biomass by centrifugation at 6,000 *g* for 30 minutes. The resulting pellet was washed five times as previously described to remove any residual PEG 4000 from the spores. On the final wash we removed 50 µl of spore suspension for use in quantifying the percent cell contamination. A final wet weight was determined after two 30 m centrifugation cycles at 6100 *g*.

2.3.2 Contamination Quantification

The 50 µL spore suspension aliquot was diluted 3 to 10 times with 0.1 M NaCl to yield bacterial counts between 20 and 400 cells per field of view at 1000 X magnification. 10 µL of the diluted spore suspension was used to make smears on ethanol cleaned glass slides. Dried smears were heat fixed and stained with malachite green and safranin according to the Schaeffer-Fulton method (Schaeffer and Fulton, 1933). Spores were stained first by flooding the heat fixed slide with a 5 % w/v malachite green stain and heated over a beaker of boiling water for 5 m. We rinsed off excess malachite green stain after the slide cooled and flooded the smear in a 0.6 % w/v safranin stain for 30 s. A final, 5 m rinse step removed residual malachite green and safranin stain from the smear.

This method stains spores a blue-green color while vegetative cells are dyed red. Viewed under a light microscope it is easy to differentiate cells from spores based on color. When observed with a mercury lamp light source and 546 nm excitation / 590 nm emission filter both the spores and cells fluoresced red. In most cases cells and spores fluoresced more brightly than

excess stain or debris on the slides. We took both bright-field and fluorescent microscopy images of the same field of view at 1000 X magnification using a Zeiss Axiostar *plus* microscope equipped with a Neofluar 100 X oil immersion lens and a Zeiss AxioVison camera. Ten randomly chosen fields of view were imaged from a single smear for each purified spore harvest.

The total number of spores and cells, termed total counts, were determined from the fluorescent images either manually or using CellC (Selinummi et al., 2005). CellC is image processing software designed to count cells in microscopy images based on the intensity of cells relative to the background (Selinummi et al., 2005). The CellC program can be downloaded for free at *http://sites.google.com/site/cellcsoftware/*. We optimized the CellC analysis by comparing manual total counts to those generated by CellC and adjusting the image analysis parameters to generate the smallest deviation between the hand and automated counts (Table 2.1). All ten fluorescent images from a smear were batch analyzed based on an intensity threshold chosen to best enumerate the total count in the first image.

Table 2.1 CellC parameters and the corresponding input values used for batch fluorescent image analysis.

CellC Parameter	**Input**
Background correction	On
Automatic intensity threshold (figure 1)	Off; batch dependent, 0.28 – 0.70
Automatic intensity threshold (figure 2)	(NA)
Divide cell clusters into single cells	0.95
Cluster division algorithm	Cell Shape
Use micrometers instead of pixels[a]	1pixel = 0.064516μm
Fill holes of cells	Off
Auto removal of over/undersized cells	Off
Type of Image	Fluorescence Microscopy

[a] Specific to microscope objective

Cells were counted manually in the bright-field images and included spores with significant portions of safranin stained cell material adhered to their surface. Percent spores (%S) in the final purified spore biomass was determined from the difference between the sum of

the cells counted in each of the ten brightfield images (C) and the sum of total (spores and cells) counts (T) in the ten fluorescence images, divided by the sum of total counts (Eq. 2.1).

Eq. 2.1 $$\%S = \frac{(T-C)}{T} \times 100$$

We tested the repeatability of this method by quantifying the percent spore concentration for 8 separate smears made from the same purified spore suspension.

2.4 Results and Discussion

While many researchers use a specialized sporulation media or defined chemical medium to generate spores (Berlin et al., 1963; Boyles and Lincoln, 1958; Harwood and Cutting, 1990; Roth et al., 2010) we use a dilute commercially available growth media. With an incubation time of 6 days *B. subtilis* cells in 0.3 % TSB undergo extensive sporulation and many shed their host cell material. This growth process provides a simple method to induce sporulation and generate milligrams of spore biomass without the use of a specialized medium or more complex chemically defined mediums. It also eliminates the need for sterile solution or cell transfers that can increase the risk of culture contamination.

The average yield following spore purification was 40 mg spores per L of *B. subtilis* growth. Spore yield is dependent on numerous factors including the concentration of spores produced in the growth culture, the biomass to extraction solution ratio and the distribution of spores within the top phase of the extraction solution. Stepwise removal and centrifugation of the top organic phase provided qualitative evidence suggesting spores are not evenly distributed in the top phase of the extraction solution and instead tend to concentration closer to the two-phase interface. This is in agreement with findings from Sacks and Alderton (1961) for *B. subtilis* spore extraction. Due to multiple factors influencing the final spore concentration and

uneven distribution of spores within the top extraction phase it is not possible to determine the percent of total spores isolated in the final purified biomass.

Our adjustments to the two phase extraction protocol originally outlined by Sacks and Alderton (1961) included a specified ratio of sporulated, unprocessed *B. subtilis* biomass to two phase extraction solution volume. Changing this ratio will likely change the final purity of a single, top phase extraction due to finite cell and spore carrying capacities within the organic, electrolytic and interfacial solution phases. We also reduced the recommended 1500 *g* centrifugation step used to separate the organic and electrolyte phase (Sacks and Alderton, 1961) to 100*g*. This centrifugation step simply speeds up the separation of the two phases. High speed centrifugation was unnecessary to achieve the observed results. With these adaptations a single top phase extraction step is capable of producing a high purity *B. subtilis* spore biomass.

We purified twenty-two spore crops and quantified their spore concentrations based on both manual and automated CellC total counts (spores and cells). Percent spores were calculated using manually determined cell counts that included safranin stained cells and spores with significant safranin stained material still attached. This provides a conservative, low-end, value for the spore purity within each harvest. Manually counting the cells within a set of ten brightfield images takes approximately 10 m when using a counting tool that records a number at each point clicked on an image (e.g. Photoshop counting tool). The low occurrence of cells within a purified spore harvest makes this portion of the spore quantification method rapid and on par with the time required to take 10 images of the slide. The overall time saved by avoiding regrowth steps and manual colony counting is significant.

The medcouple (MC), a measure of data skewness that ranges from 1 to -1 with 0 describing a Gaussian distribution, was calculated for both the CellC and manually derived percent spore data to determine the proper statistical tests for summarizing and relating the two data sets (Brys et al., 2004; Hubert and Van der Veeken, 2008). For manually and CellC determined percent spore purity data (n=22) we calculated MC values of -0.54 and -0.62

respectively. These negative MC values indicate a highly left skewed data set. Manual and CellC generated total counts from batch image analyses had MC values of 0.44 and 0.40, respectively, indicating right skewed data. The MC values describing our data warrant the use of non-parametric statistical analyses which do not assume Gaussian distributions.

The spore isolation processes described in Section 2.1 resulted in an average spore concentration and 1σ standard deviation of 88 ± 11 % based on manual cell and spore counts from 22 spore crops. Nearly 60 % of the 22 analyzed spore crops, however, were 91-100 % spores according to manual counts (Fig. 2.1). This distribution resulted in the observed non-parametric data set and negative MC values. Due to data skewness the median can provide a more accurate data summary and prediction of typical spore purity results. The median of the manually derived spore purity data is 93 %.

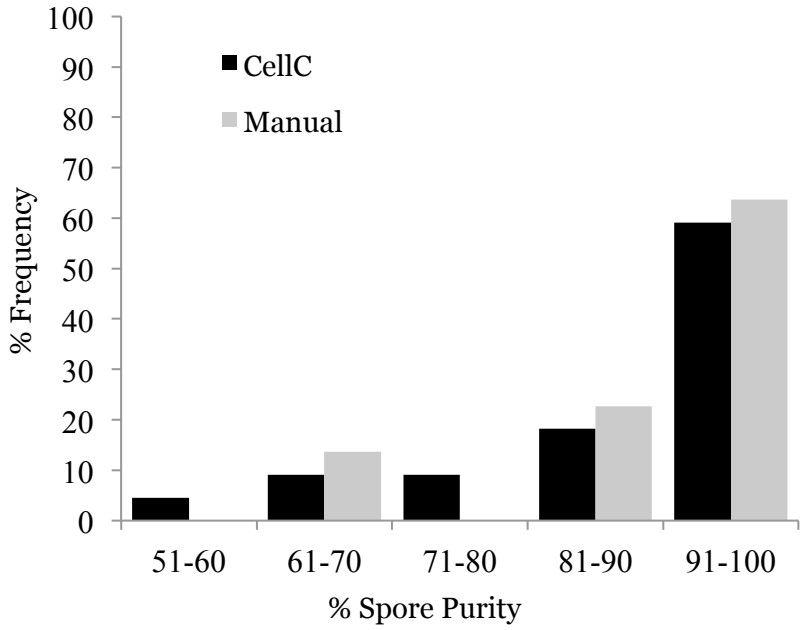

Figure 2.1 Percent frequency of spore purity determined by CellC and manual counts of purified B. subtilis spore harvests (n=22). Cell counts include spores with significant safranin stained material still attached and provide an upper estimate of cell contamination

We accelerated spore purity quantification by using CellC to generate a total count from the fluorescent images. The average percent spore purity and 1σ standard deviation based on total counts generated by CellC for the same 22 spore crops is 87 ± 11 % with a median of 92 %. Fig. 2.1 displays the frequency of spore crops within a given range of spore purity for both manual and CellC generated values. Variation in the percent spore purity can result from numerous sources including temperature variations (Sacks and Alderton, 1961), removal of interfacial solution, inadequate homogenization of the two-phase solution and variations in the spore content of the growth medium.

Errors in cell and spore counts were estimated to be 5 % for manual counts and 10 % for CellC generated counts. Errors in both manual and CellC counts may arise from bacterial aggregates and biotic debris in the smears. Total counts from CellC, however, tend to yield lower values relative to manual counts (Fig. 2.2). CellC error sources include limitations in resolving cell and spore boundaries in an aggregate and an inability to discern fluorescing debris from actual cells and spores. The latter of these complications seems to be less of an issue for CellC counts since the intensity threshold of the analyses appeared to filter out fluorescing debris and CellC counts rarely exceeded manual counts. Bacterial aggregates were reduced by diluting the spore suspension prior to making smears. Visual inspection and comparison of the binarized CellC image output with the original microscopy images indicated that individual bacteria within aggregates were not adequately isolated and often undercounted despite the use of cell division algorithms. An example of this can be seen by comparing bacterial aggregate separation in the binarized CellC image, Fig. 2.2C, with the original microscopy images, Fig. 2.2A and B, and the total CellC and manual counts of 152 and 161, respectively. These inaccuracies in bacterial aggregate separation make a large contribution to the final CellC count error. Additional errors in CellC counts can arise from batch image binarization based on a single intensity threshold where inconsistencies in the background and cell fluorescence intensities within individual images and a batch of images can result in counting errors.

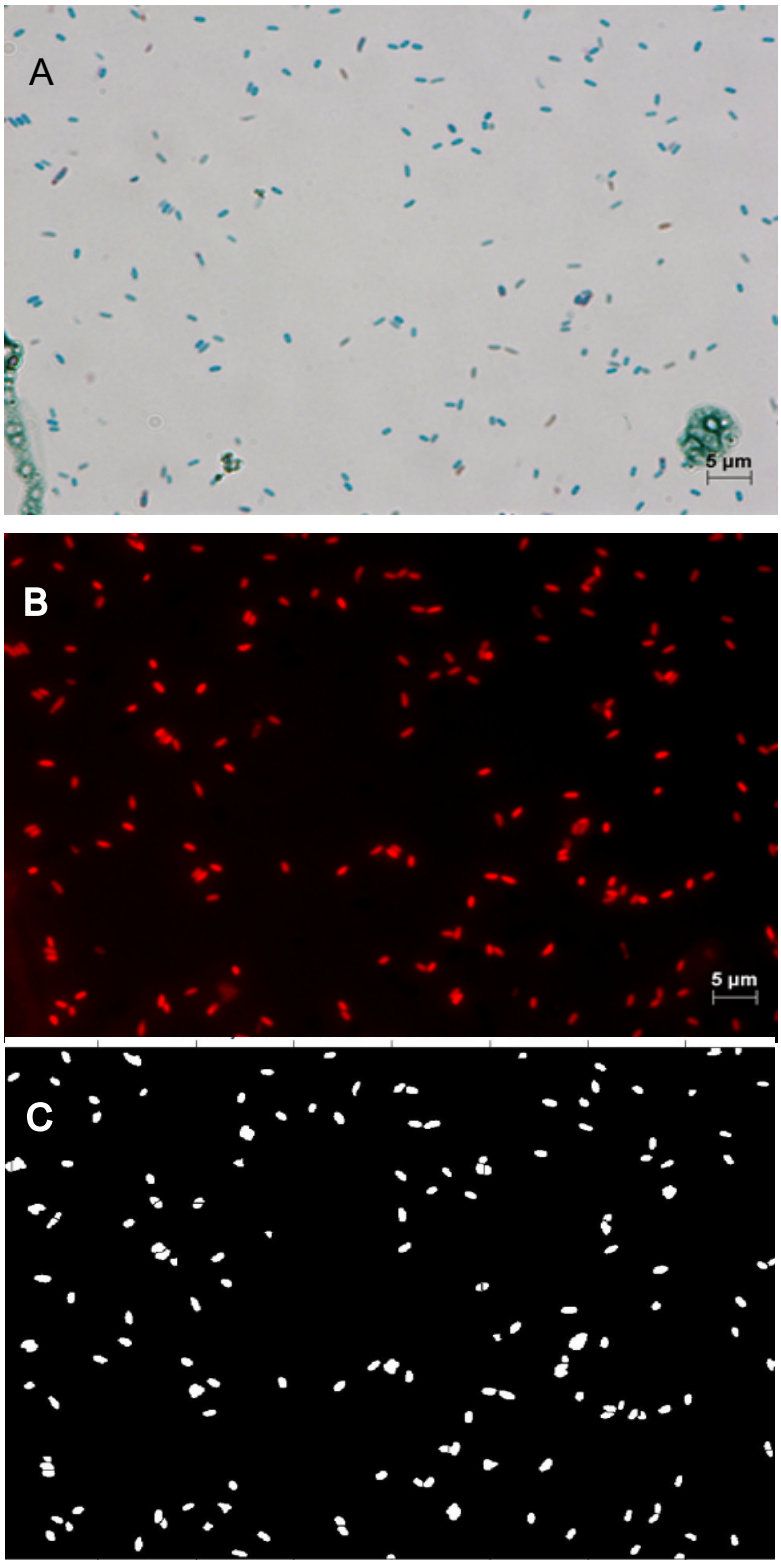

Figure 2.2 Corresponding brightfield (A), fluorescent microscopy images (B) and the binarized CellC output (C) for a purified spore harvest stained according to the Schaffer-Fulton method. The manual total count is 161 and the CellC total count is 152.

Lower total counts from CellC enumeration result in lower percent spore purity for the CellC derived data. This can be observed in a linear regression plot of manually versus CellC determined percent spore data (Fig. 2.3) where the y-intercept is negative due to lower percent spore values in the CellC data. The relationship between CellC bias and the calculated percent spore value is a function of Eq. 2.1. This calculation assumes that the percent spores cannot exceed 100 %. If we calculated percent spores using a manually derived spore count, the manual spore count from an image with 100 % spores could exceed the CellC total count due to the low count bias. This would result in a CellC derived percent spore value in excess of 100 % and a relationship between CellC and manually derived percent spore values inverse to that observed in our data. We choose to use Eq. 2.1 since manually counting the cells within a purified spore biomass image is much more rapid than manual spore enumeration. Based on these considerations we recommend and utilize a 10 % error for CellC counts when determining the error in individual percent spore values. Propagation of both CellC and manual count errors produced smaller individual errors than the standard deviation of the entire data set.

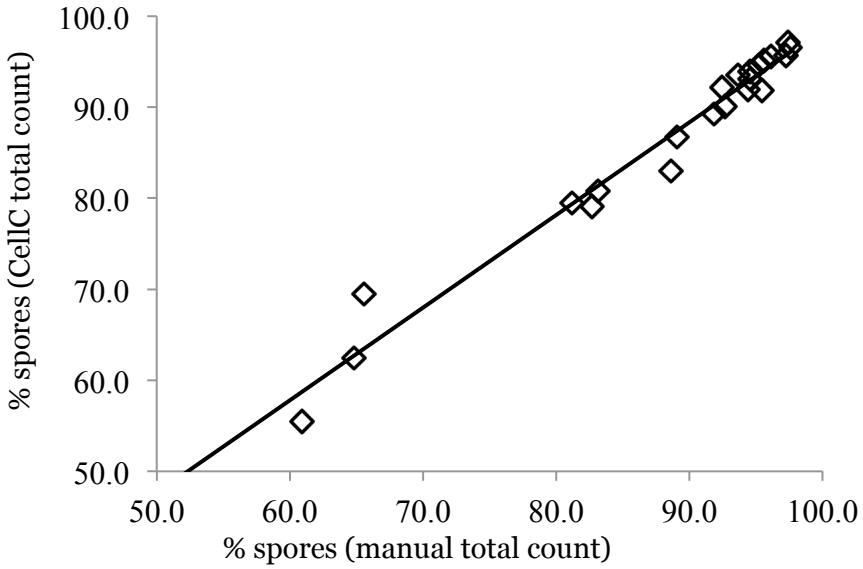

Figure 2.3 Linear regression correlating manual versus CellC based % spore data ($y = 1.0x - 3.2$, $R^2 = 0.97$).

The accuracy of CellC generated total counts from fluorescent images can be assessed by determining the spearman coefficient, ρ, which compares CellC and manual counts. The Spearman coefficient is used to relate skewed data sets based on the rank of each data point and average of each data set. The spearman coefficient correlating CellC and manual total count data from batch image analysis of 22 spore crops was 0.97. Based on this Spearman coefficient it is evident that CellC batch analyses generate reliable total cell and spore counts from our fluorescent images despite bacterial clumping and unavoidable variations in the background intensity of each image.

Table 2.2 Spore purity data for 8 smears made from the same purified spore suspension. Cell and spore counts for each smear include 10 fluorescent and corresponding brightfield images. Percent spore purity values provide a low end estimate by including spores with attached safranin stained material in the cell count value.

Replicate	Total Count (CellC)	Cell Count (manual)	% Spore Purity
B1	1865	100	95
B2	1394	112	92
C1	1633	76	95
C2	973	47	95
D1	687	45	93
D2	1034	49	95
E1	1631	40	98
E2	1159	62	95
		Average [a]	**95 ± 3**

[a] error is 2σ

Selinummi et al. (2005) utilized the Pearson coefficient (r), a correlation coefficient for data sets with a Gaussian distribution based on the averaged total count, standard deviations in the two data sets and the total number of data points in a data set, to correlate their CellC and manual count data. Their Pearson coefficient for DAPI stained bacteria was 0.98. Despite the non-Gaussian nature of our data we also calculated a Pearson coefficient to enable direct comparison of our CellC counting accuracy to Selinummi et al. (2005). Our Pearson coefficient

correlating CellC generated and manual total counts within 22 batches of images was 0.98 which is in good agreement with the *r* value determined by Selinummi et al. (2005).

Our CellC based percent spore quantification method proved to be repeatable over 8 smears made from the same spore suspension. Spore purity for each smear was determined using CellC total counts and yielded an average value of 95 ± 3 % (error is 2σ; Table 2.2). This level of repeatability indicates that the distribution of cells and spores within a smear is roughly homogeneous over ten randomly chosen fields of view at 1000 X magnification and representative of the parent solution.

2.5 Conclusions

In this study we refined and developed efficient methods for *B. subtilis* spore growth, separation and quantification that minimizes cell contamination errors in *Bacillus subtilis* spore research. A 0.3 % TSB growth medium produced significant *Bacillus subtilis* cell growth and subsequent sporulation over a six day incubation period. Based on the method of Sacks and Alderton (1961) we produced a highly purified spore biomass on the order of milligrams, by extracting approximately 80 % of the spore laden organic phase from a two-phase extraction system. To determine the purity of spore harvests we devised a semi-automated method to quantify spore harvest purity that combines the Shaffer-Fulton differential staining technique, brightfield and fluorescence microscopy imaging and CellC image processing.

Spore purity quantification results indicate that the combination of a defined biomass to two-phase extraction solution ratio, a reduction in the centrifugal force used for phase separation and a single top phase extraction step produces a high purity spore biomass. This eliminates the need for additional extraction steps, saving both time and resources. The spore purity quantification method described here enables rapid analysis of individual spore crop

purity and allows for better quality control in repeat experiments requiring a cell-free spore biomass.

2.6 References

Berlin, E., Curran, H.R., Pallansch, M.J., 1963. Physical surface features and chemical density of dry bacterial spores. J. of Bacteriol. 86, 1030-1036.

Boyles, W.A., Lincoln, R.E., 1958. Separation and concentration of bacterial spores and vegetative cells by foam flotation. Appl. Microbiol. 6, 327-334.

Brys, G., Hubert, M., Struyf, A., 2004. A robust measure of skewness. J. of Comp and Graph. Stat. 13, 996-1017.

De Vrind, J.P.M., De Vrind-De Jong, E.W., De Voogt, J.-W., H., Westbroek, P., Boogerd, F.C., Rosson, R.A., 1986. Manganese oxidation by spores and spore coats of a marine *Bacillus* species. Appl. Environ. Microbiol. 52, 1096-1100.

Goldman, R.C., Tipper, D.J., 1978. *Bacillus subtilis* spore coats: Complexity and purification of a unique polypeptide component. J. of Bacteriol. 135, 1091-1106.

Harwood, C.R., Cutting, S.M., 1990. Molecular biological methods for *Bacillus*, Wiley, Chichester; New York.

He, L.M., Tebo, B.M., 1998. Surface charge properties of and Cu(ii) adsorption by spores of the marine *Bacillus sp*. Strain sg-1. Appl. Environ. Microbiol. 64, 1123-1129.

Hubert, M., Van der Veeken, S., 2008. Outlier detection for skewed data, J. Chemomet., Vol. 22, pp. 235.

Nicholson, W.L., 2002. Roles of bacillus endospores in the environment. Cell. Mol. Life Sci. 59, 410-416.

Nicholson, W.L., Fajardo-Cavazos, P., Rebeil, R., Slieman, T.A., Riesenman, P.J., Law, J.F., Xue, Y.M., 2002. Bacterial endospores and their significance in stress resistance. Antonie Van Leeuwenhoek Int. J. Gen. Molec. Microbiol. 81, 27-32.

Revis, N.W., Hadden, C.T., Edenborn, H., 1997. Removal of dissolved heavy metals and radionuclides by microbial spores, Technical Report DOE/OR/21492--T9, US DOE.

Rosson, R.A., Nealson, K.H., 1982. Manganese binding and oxidation by spores of a marine bacillus. J. Bacteriol. 151, 1027-1034.

Roth, S., Feichtinger, J., Hertel, C., 2010. Characterization of bacillus subtilis spore inactivation in low-pressure, low-temperature gas plasma sterilization processes, Vol. 108, Blackwell Publishing Ltd, pp. 521-531.

Sacks, L.E., Alderton, G., 1961. Behavior of bacterial spores in aqueous polymer two-phase systems. J. Bacteriol. 82, 331-341.

Schaeffer, A.B., Fulton, M.D., 1933. A simplified method of staining endospores. Science (New York, N.Y.). 77.

Selinummi, J., Seppälä, J., Yli-Harja, O., Puhakka, J.A., 2005. Software for quantification of labeled bacteria from digital microscope images by automated image analysis. BioTechniq. 39, 859-863.

Siala, A., Hill, I.R., Gray, T.R.G., 1974. Populations of spore-forming bacteria in an acid forest soil, with special reference to bacillus subtilis. J. Gen. Microbiol. 81, 183-190.

Chapter 3: Thermodynamic analysis of *Bacillus subtilis* endospore protonation using isothermal titration calorimetry

3.1 Abstract

Bacterial proton and metal adsorption reactions have the capacity to affect metal speciation and transport in aqueous environments. We coupled potentiometric titration and isothermal titration calorimetry (ITC) analyses to study Bacillus subtilis spore-proton adsorption. We modeled the potentiometric data using a four and five-site non-electrostatic surface complexation model (NE-SCM). Heats of spore surface protonation from coupled ITC analyses were used to determine site specific enthalpies of protonation based on NE-SCMs. The five-site model resulted in a substantially better model fit for the heats of protonation but did not significantly improve the potentiometric titration model fit. The improvement observed in the five-site protonation heat model suggests the presence of a highly exothermic protonation reaction circa pH 7 that cannot be resolved in the less sensitive potentiometric data. From the log Ks and enthalpies we calculated corresponding site specific entropies. Log Ks and site concentrations describing spore surface protonation are statistically equivalent to B. subtilis cell surface protonation constants. Spore surface protonation enthalpies, however, are more exothermic relative to cell based adsorption suggesting a different bonding environment. The thermodynamic parameters defined in this study provide insight on molecular scale spore-surface protonation reactions. Coupled ITC and potentiometric titrations can reveal highly exothermic, and possibly endothermic, adsorption reactions that are overshadowed in potentiometric models alone. Spore-proton adsorption NE-SCMs derived in this study provide a framework for future metal adsorption studies.

3.2 Introduction

Microbially hosted adsorption reactions have the potential to influence the distribution and fate of dissolved chemicals in aqueous systems. Our knowledge of vegetative bacterial cell, referred to here as "cell," surface reactivity has grown rapidly to include thermodynamic data for proton and metal adsorption. Thermodynamic stability constants, enthalpies and entropies derived from calorimetric data and surface complexation modeling give insight into the mechanisms underlying cell surface complexation and provide parameters for modeling cell surface adsorption in natural aqueous systems. Comparatively little work, however, focuses on adsorption reactions hosted by bacterial endospores, termed "spores" in this paper.

Bacterial spores are a metabolically dormant cell type produced by numerous bacterial genera, including *Bacillus* and *Clostridium*, to protect their DNA under harsh environmental conditions. Spore surfaces are primarily comprised of a tough proteinaceous coat (Driks, 1999; Driks, 2002; Gould and Hurst, 1969) that may react differently with dissolved constituents relative to cell surfaces consisting of polysaccharides, lipopolysaccharides and peptidoglycan, among other organic molecules. Although both spore and cell surfaces are porous, He and Tebo (1998) found the *Bacillus* SG-1 spore surface area up to four times larger than its parent cell counterpart. In some environments spores comprise up to 45 % of the total bacteria population (Siala et al., 1974) and have the potential to outnumber parent cells. In fifty soil samples, Hong et al. (2009) determined an average aerobic spore count (~10^5 CFU g^{-1}) on par with vegetative cell densities. In a bacterial population comprised of 50 % spores, their surface area could contribute up to two times the surface area of the parent cell.

Spore coats, like bacterial cell surfaces, may host multiple, chemically distinct ligands. Our knowledge of spore surface complexation reactions is limited and insufficiently characterized by bulk distribution coefficients (K_d) describing proton and metal adsorption affinities (He and Tebo, 1998; Revis et al., 1997; Rode and Foster, 1966). K_d values, defined as

the ratio of adsorbed to dissolved constituents, oversimplify and fail to provide molecular scale insight on the adsorption reactions (Bethke and Brady, 2000). Unlike distribution coefficients, surface complexation models (SCM) are based on balanced chemical equations that are mechanistically related to the adsorption reactions occurring. Spectroscopic data of cell-metal adsorption supports the theory that sites derived from surface complexation models represent actual metal-active ligands on the cell surface (Kelly et al., 2002). More recent investigations employ calorimetric analyses that compliment SCMs and provide a more detailed understanding of the molecular scale thermodynamics associated with bacterial surface adsorption (Gorman-Lewis et al., 2006). Jesperson and Jordan (1970) also utilized ITC to generate robust determinations of proton active ligands and their concentrations in proteins.

Together, the large surface area of spores and poorly constrained spore adsorption models make it difficult to understand the influence of microbes on aqueous geochemical cycles. Our research will extend beyond the scope of system specific K_d values by fitting surface complexation models to potentiometric titration and isothermal titration calorimetry (ITC) data describing *Bacillus subtilis* spore surface protonation. From the SCM we will derive reactive site concentrations, thermodynamic stability constants, and enthalpies and entropies of protonation for a suite of potential proton adsorption sites on the spore surface.

The enthalpies, entropies and Gibbs energies generated in this approach provide quantitative information on the thermodynamic driving forces underlying spore surface-protonation. We will compare the thermodynamic spore-proton adsorption data to amino acid acidity constants, entropies and enthalpies to better constrain which ligands may be responsible for proton adsorption. Additional comparisons with *B. subtilis* cell surface protonation data offers insight on the chemical differences between cell and spore surface adsorption behavior. Acidity constants and site concentrations generated in this research will provide the necessary framework for investigating spore-metal adsorption through SCMs in the future.

3.3 Methods

3.3.1 Spore growth and isolation

We grew and isolated *Bacillus subtilis* spores as described in Harrold et al. (2011). *B. subtilis* was inoculated from agar plate cultures and incubated for 1 day in 3 % trypticase soy broth (TSB) and 0.5 % yeast extract. Culture tubes were transferred to 1 or 2 L volumes of 0.3 % TSB and incubated for 6 days. Spores were isolated with a two-phase, polyethylene glycol 4000 and potassium phosphate buffer separatory solution (Harrold et al., 2011). We determined the purity of each spore harvest following ITC analysis using the method described in Harrold et al. (2011). Total cell and spore counts were generated from CellC (Selinummi et al., 2005) batch analyses of ten fluorescence images at 1000 x magnification. Cell counts were determined manually from corresponding bright-field images.

3.3.2 Dipicolinic Acid (DPA) analysis

Bacterial spores contain a large reservoir of pyridine 2,6-dicarboxylic acid, also known as dipicolinic acid (DPA), within their cortex (Nicholson et al., 2000; Setlow, 2003; Warth, 1983). DPA released into solution during a titration has the potential to produce errors in the potentiometric data. We measured the amount of DPA released from spore suspensions of 35 g L^{-1} and 100 g L^{-1} as a function of pH and time. DPA was measured according to a method by Warth (1983) that utilizes the derivative of the Ca-DPA complex absorption. Aliquots of spore suspensions were sampled at different time intervals and filtered with pre-rinsed 0.1 uM millipore filters. The Ca-DPA complex was produced by adding 0.4 mL of 9 mM $CaCl_2$ and 180mM Tris base to 0.5 mL of filtered sample (Warth, 1983). The solution absorbance was measured from 300 nm to 250 nm with a scan rate of 20 nm min^{-1} and 0.1 nm data intervals on a Cary 300 Bio UV-Vis spectrophotometer. The difference between peak and valley values at

276 nm and 280 nm, respectively, from the derivative spectra were used to determine the concentration of DPA based on a standard calibration curve.

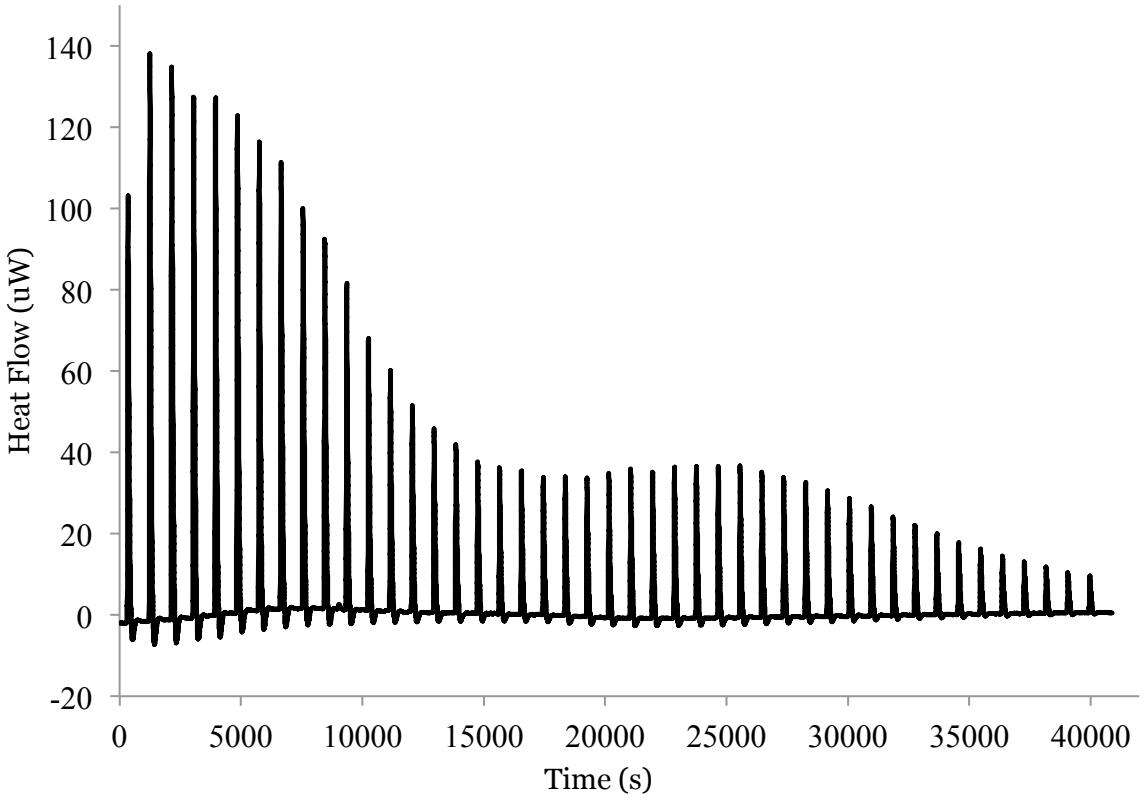

Figure 3.1 Heat flow from a B. subtilis spore surface protonation assay measured by isothermal titration calorimetry. Each peak in the heat flow corresponds to a 2 μL acid injection. Positive heats are exothermic. Suspension pH decreases from pH 10 to approximately pH 3 with increasing time.

3.3.3 Isothermal titration calorimetry

We performed isothermal titration calorimetry (ITC) on a TAM III nanocalorimeter that measures heat flux between a reaction and reference vessel as a function of time (Fig. 3.1). A computer controlled Lund syringe pump delivered aliquots of acid to the reaction vessel in the calorimeter and to an identical, external sample being monitored by an Orion 8103BN Ross semi-micro combination pH electrode calibrated with 4 NIST standards. Spores were suspended in degassed 0.1 M $NaClO_4$ to buffer ionic strength. The spore suspension was

adjusted to approximately pH 10 in an anaerobic chamber using a known amount of CO_2 free 1.025 M NaOH.

1 mL aliquots of the suspension were pipetted into Hastelloy reaction and reference vessels for ITC analysis and an external reaction vessel for pH monitoring. Upon removal from the anaerobic chamber the vessels for ITC analysis were immediately capped and placed into the reaction and reference chambers. We performed the titrations by injecting 2 μL of 0.143 M $HClO_4$ into both the ITC reaction vessel and the external suspension. Intervals between injections spanned 10 to 15 minutes to allow ample time for the heat signal to reach the baseline prior to the next injection (Fig. 3.1). The pH of the external suspension was monitored continuously and measurements were recorded every 3 seconds. Temperature within the isothermal titration calorimeter was maintained at 25 °C within μ°C variability by a temperature controlled, insulating oil reservoir. The parallel potentiometric titration experiments were subject to ambient laboratory temperature maintained at 23 °C with 0.3 °C variability. We report experimental temperatures of 25 °C to remain consistent with the more temperature sensitive analysis. We discarded the first data point in each spore ITC analysis due to anomalous heat associated with the first titrant addition and acid diffusion into the solutions as the system equilibrates prior to initiating the experiment.

We determined the heat evolved from spore surface protonation reactions ($Q_{corr,n}$, Eq. 3.1) by subtracting the stepwise background heats (i.e., heats intrinsic to the titration such as heats of dilution) ($Q_{bkg,n}$), from the ITC data ($Q_{meas,n}$). Background heats were determined as outlined above with spore-free solutions.

Eq. 3.1 $$Q_{corr,n} = Q_{meas,n} - Q_{bkg,n}$$

The average background heat was 0.1 ± 0.03 mJ (1σ). Heats of base neutralization ($H^+ + OH^- \rightarrow H_2O$) were calculated from the measured pH change for each step of a titration and an enthalpy of -56.48 kJ mol^{-1} (Gorman-Lewis et al., 2006) and included in $Q_{bkg,n}$.

When loading an ITC vial, the suspension was exposed to the atmosphere. Consequently, the spore suspensions could have absorbed some CO_2. To estimate the possible heat and proton uptake by dissolved CO_2 we calculated the stepwise, pH dependent, proton buffering capacity and heat flux for the maximum CO_2 contamination from 3 mL of atmospheric headspace. Both the CO_2 buffering capacity and protonation heats produced from our calculations are two orders of magnitude smaller than the stepwise spore protonation buffering capacity and corrected reaction heats. Maximum calculated CO_2 protonation heats were endothermic (+0.04 mJ). CO_2 contamination in the spore suspension aliquot utilized for pH measurements was eliminated by placing it under a positive pressure of N_2 gas for the duration of the titration.

3.3.4 Potentiometric titration reversibility

We tested the reversibility of spore protonation reactions by performing multiple potentiometric titrations on the same spore suspension. 35 g L^{-1} spore suspensions were made with N_2 degassed 0.1 M $NaClO_4$ to buffer ionic strength. 1 mL aliquots of the 35 g L^{-1} spore suspension were adjusted to pH 10 with a known amount of CO_2 free 0.143 M NaOH and subsequently titrated to pH 3. Following the first titration, we readjusted the spore suspension to pH 10 with a known amount of carbon dioxide free NaOH and titrated it again to pH 3.

Spores are highly resistant to acids and bases (Setlow, 2006; Nicholson, 2000). Setlow et al. (2002) studied the effectiveness of killing *B. subtilis* spores with HCl and NaOH solutions ranging from 0.3 M to 2 M, while Williams and Russell (1993) determined *B. subtilis* spore resistance to NaOH concentrations upwards of 0.2 M. Our experimental pH conditions are mild compared to these spore-killing treatments. These findings combined with the DPA release (see

Section 3.2) and reversibility titration (see Section 3.3.2) data in this paper suggest that spore integrity was maintained throughout the experiments.

3.4 Results and Discussion

3.4.1 Spore harvest purity

Spore suspensions following ITC analysis were on average 93 ± 3 % (1σ standard deviation) pure, meaning cell contamination was very low. We expect little deviation in the spore purity during the calorimetric titrations. The flat baseline observed over the course of the ITC analysis suggests little to no spore germination, outgrowth or residual cell metabolism.

3.4.2 DPA release

Bacillus subtilis spores contain a large reservoir of pyridine-2,6 dicarboxylic acid (dipicolinic acid, DPA) in their cortex (Setlow, 2003; Warth, 1983). DPA is a diprotic acid with pK_{a1} and pK_{a2} of 4.66 and 2.07, respectively (Martell et al., 1998). DPA released into solution can affect the proton mass balance by releasing or taking up protons over the course of an acidic ITC titration from high to low pH. All *B. subtilis* spore suspension assays slowly released DPA into solution over time, irrespective of pH. Low pH assays exhibited the most DPA release. 35 g L^{-1} *B. subtilis* spore suspensions equilibrated for 4 hrs at pH approximately 3 and 6.5 released 15.9 ± 0.4 μmol kg^{-1} and 4.9 ± 1.0 μmol kg^{-1} DPA (all errors are 1σ), respectively. DPA release from a 35 g L^{-1} spore assay adjusted to pH 9 and equilibrated for four hours increased with time but was below the detection limit (~5-9 μmol kg^{-1} DPA, dependent on sample volume). These results indicate the largest DPA release occurs at low pH. DPA release from three 35 g L^{-1} *B. subtilis* spore reversibility titrations ranged from 8.9 ± 0.5 to 17.7 ± 1.8 μmol kg^{-1} DPA. Two, 100 g L^{-1} spore suspensions adjusted to ca. pH 3 and equilibrated for approximately 2 hr and 45min released 38 ± 3 and 84 ± 2 μmol kg^{-1} DPA. The highest DPA release, 93 ± 2 μmol kg^{-1}, was

measured in a 100 g L^{-1} spore assay equilibrated for 3hr and 40 min circa pH 3. DPA measured in 100 g L^{-1} spore suspensions at pH circa 5, 7 and 10 was below the experimental detection limit. DPA concentrations did not plateau in any of the time dependent experiments (Fig. 3.2 and 3.3).

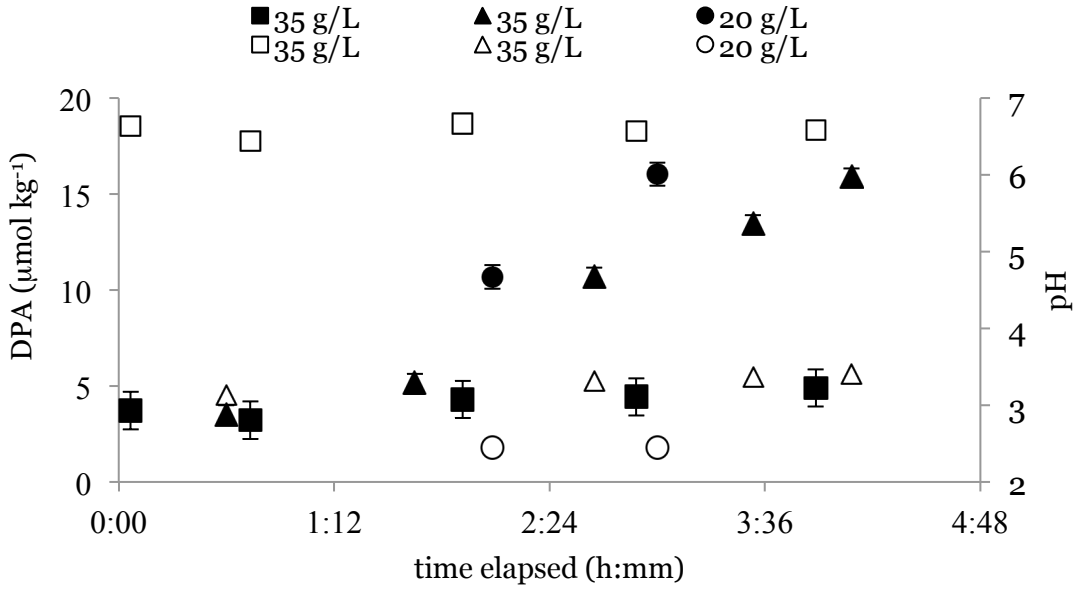

Figure 3.2 DPA (closed symbols) release and pH (open symbols) change as a function of time for 20 and 35 g L^{-1} B. subtilis spore suspensions.

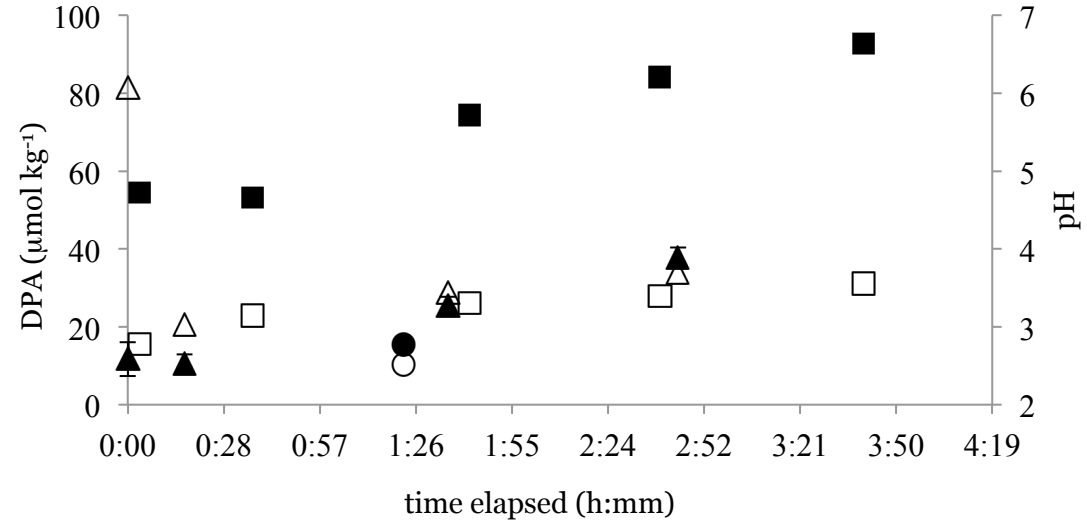

Figure 3.3 DPA released (closed symbols) and pH (open symbols) change over time for 100 g L^{-1} B. subtilis spore suspensions.

A study using *B. megaterium* showed a rapid release of spore DPA when germination was initiated with L-alanine (Scott and Ellar, 1978). DPA released from the germinating population reached a concentration of 450 μmol g^{-1} spores (dry weight) within 20 minutes (Scott and Ellar, 1978). In contrast, the DPA concentration of our spore assays increased much more slowly, over a period of hours, and only reached concentrations of approximately 0.93 μmol g^{-1} spores (wet weight) in the 100 g L^{-1} assays. Low, initial DPA concentrations in our spore suspensions are most likely from incomplete removal during the spore washing process. The slow rate of DPA release may suggest minimal to no germination in our spore assays. This belief is further supported by a lack of common germination triggers in our spore assays, aside from DPA (Setlow, 2003). The flat baseline observed over the course of ITC analyses suggests little to no metabolism. A third line of evidence includes the 93 % average spore purity determined for the spore assays following ITC analysis.

Setlow et al. (2002) observed DPA release from the *B. subtilis* cortex when exposed to strong acid treatment. This DPA release may be attributed to changes in the permeability of the spore inner membrane and is not associated with germination processes. Setlow et al. (2002) also observed significantly less DPA release from alkaline treated spores. Our pH and time dependent DPA data is in direct agreement with these findings despite much less extreme alkaline and acidic experimental conditions. Although limited spore germination is a potential source of DPA, it is more likely that our data indicates passive DPA release from the spore cortex through process related to solution pH.

3.4.3 Potentiometric Data

3.4.3.1 Proton adsorption edge

Data are plotted in Fig. 3.4 in terms of moles of protons adsorbed per gram of spores ($H_{consumed/released}$) described by Eq. 3.2:

Eq. 3.2 $$H_{consumed/released,n} = (C_a - C_b - [H^+] + [OH^-])/m_s$$

where C_a and C_b are the total concentration of acid and base, respectively, added to the spore suspension, $[H^+]$ and $[OH^-]$ are the suspension concentrations calculated from the pH, and m_s is the wet weight mass of spores in grams. The spore suspension exhibited substantial buffering capacity over the entire pH range studied. Average total proton uptake and 1σ standard deviation from triplicate titrations was 266 ± 10 μmol g^{-1}. The steep slope of the titration curves at low pH indicates that the spore surface is not fully protonated. A fully protonated surface would produce a very shallow slope indicative of little to no pH buffering capacity.

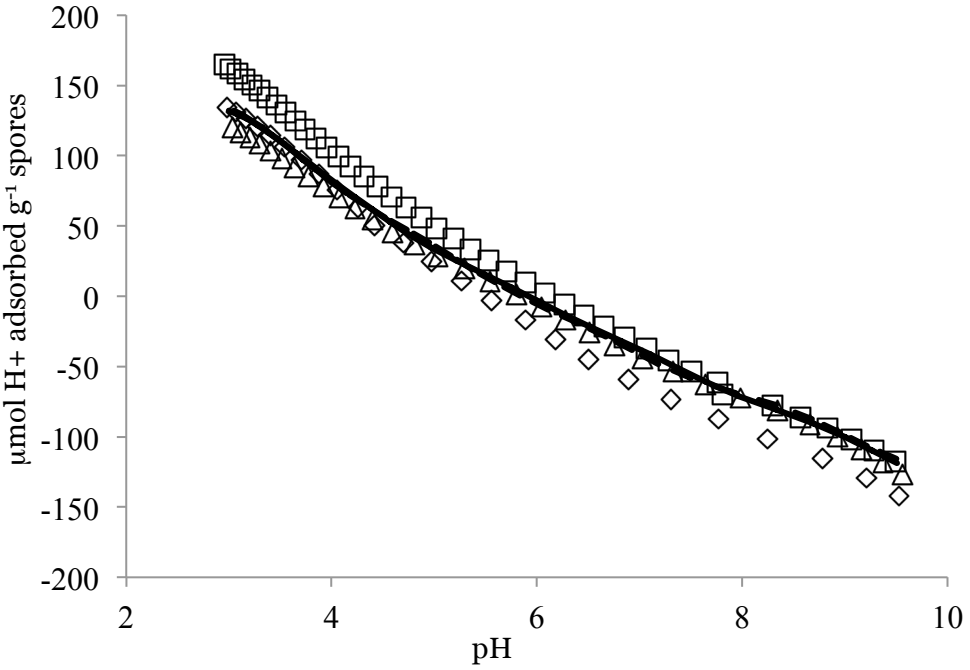

Figure 3.4 μmols of adsorbed protons per gram of B. subtilis spores in 0.1 M electrolyte at 25 °C as a function of solution pH. Data sets correspond to 20 (◇), 30 (△) and 35 (□) g L^{-1} spore suspensions. Solid and dashed curves are best fit, five and four site NE-SCMs, respectively, for an averaged 28.3 g L^{-1} spore suspension. Average T_H^o values for the five and four site models are 144 μmol g^{-1} and 132 μmol g^{-1}, respectively.

3.4.3.2 Reversibility

Triplicate reversibility titrations preformed on 35 g L^{-1} spore suspensions show little hysteresis between subsequent titrations on the same suspension (Fig. 3.5). This suggests that the protonation reactions occurring are limited to reversible adsorption reactions and not irreversible reactions that may include spore germination processes or damage to the spore surface. Some disagreement between ITC and reversibility titration data is evident at high pH values (Fig. 3.5). We believe this is a function of the shorter injection intervals used in the reversibility titrations (1-2 minutes versus 10-15 minutes) and pH drift at high pH.

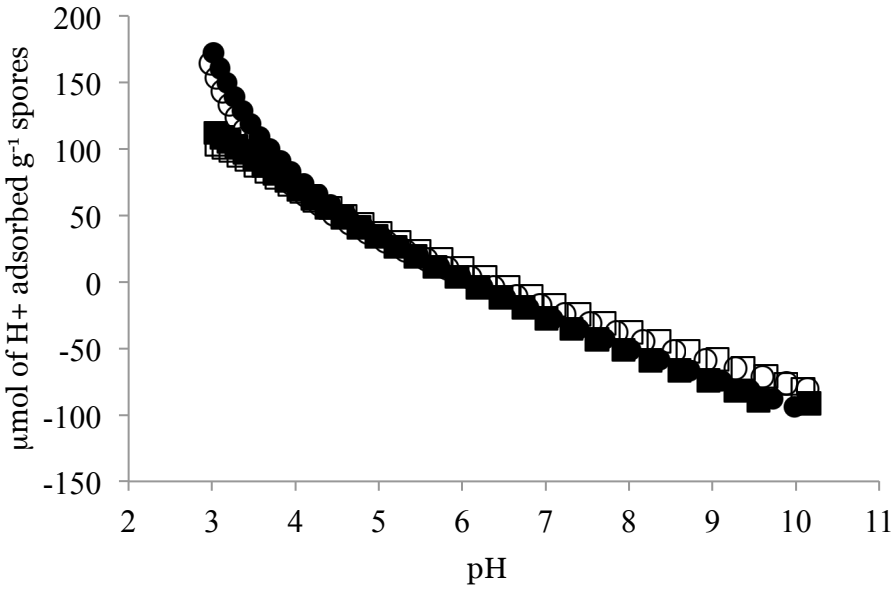

Figure 3.5 Duplicate, 35 g L^{-1} *B. subtilis* spore reversibility titrations showing the initial suspension titration (closed symbols) and secondary titrations (open symbols) following suspension readjustment to pH 10

Kapetas et al. (2011) identified time dependent discrepancies between potentiometric titration data and total bacterial surface proton uptake due to dissolved organic carbon (DOC) release. These variations in time dependent proton uptake, however, resulted in minimal significant differences between SCMs (Kapetas et al., 2011). pH dependent DPA release is the

most likely source of DOC contamination in our titration assays. We expect significantly less DOC release from *B. subtilis* spore assays relative to vegetative cell suspensions due to spore dormancy and their chemically resistant nature. Based on this and the findings of Kapetas et al. (2011) we expect longer time intervals to largely reflect the equilibrium protonation state of the *B. subtilis* spore surface. Consequently, reversibility titration data is not included in the models to avoid discrepancy due to the time interval variation in the data collection method.

3.4.3.3 Non-electrostatic Surface Complexation Modeling

We used non-electrostatic surface complexation modeling (NE-SCM) to define spore surface protonation. This approach has been applied extensively to vegetative bacterial cell adsorption (Borrok et al., 2005; Fein et al., 2005; Tourney et al., 2008). NE-SCM employs balanced chemical equations (Eq. 3.3) to describe substrate surface protonation reactions such that the total concentration of deprotonated sites on the spore surface is described in Eq. 3.4.

Eq. 3.3 $$R - L_i^- + H^+ \rightarrow R - L_iH$$

Eq. 3.4 $$\sum[R - L_i^-] = \sum_1^i \frac{[R-L_i]tot}{1+a_{H+}*K_i}$$

where $R\text{-}L_i^-$ is ligand i on the spore surface, $R\text{-}L_iH$ is a proton adsorbed to spore surface ligand i, α_{H+} is the activity of protons in solution as determined by the pH, and K_i is the stability constant defining ligand protonation.

The mass balance equations used to determine the moles of protons adsorbed to the spore surface in a titration defines the pH of immersion, or initial surface protonation state, as the zero state for each titration (Eq. 3.2, Figure 3.4 and 3.6). This methodology does not indicate that the spore surface is free of adsorbed protons at the pH of immersion. The

calculated adsorbed proton concentration as a function of pH is relative to the zero state (Fig. 3.4 and 3.6) and indicates the extent of proton adsorption or desorption in relation to the initial total proton concentration at the pH of immersion. A blank titration, in contrast, will pass through the zero line showing little to no proton uptake (Fig. 3.6). The initial total proton concentration in the system is discussed extensively by other researchers (Fein et al., 2005; Westall et al., 1995) and defined here and in other literature as $T_H{}^o$. The mass balance for total proton concentration in the system can be written as Eq. 3.5.

Eq. 3.5 $$T_H = T_H{}^o + (C_a - C_b)$$

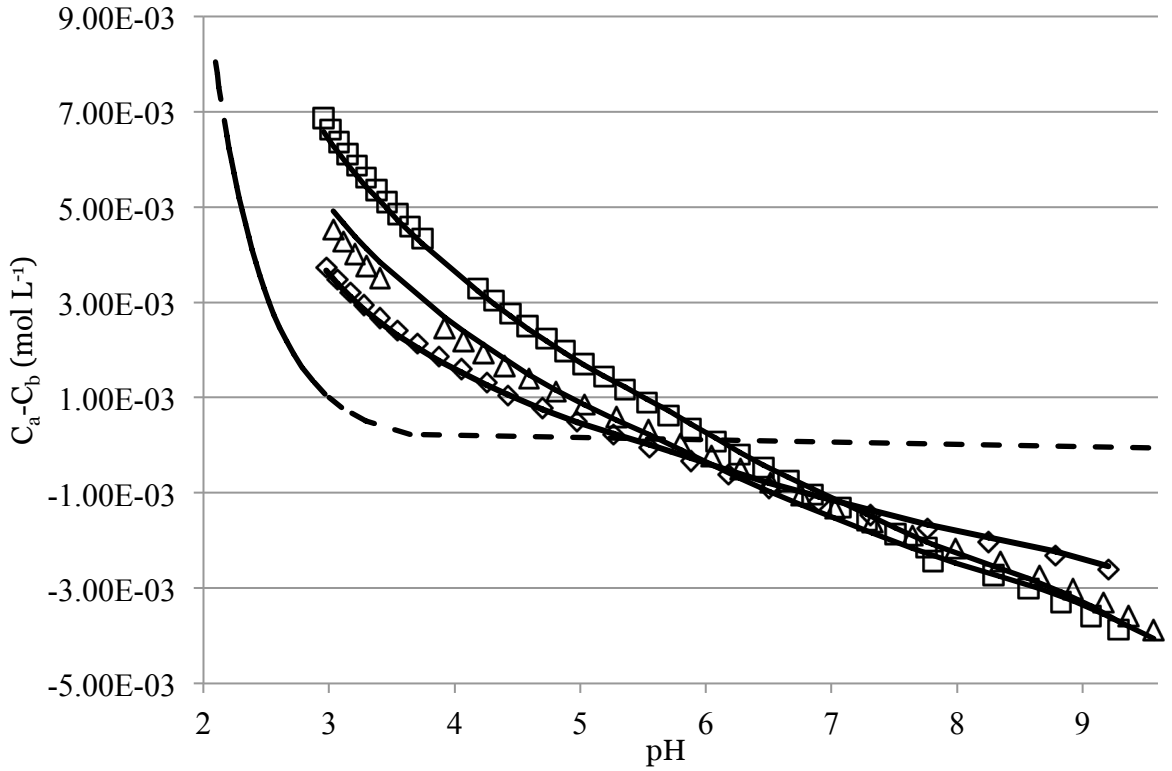

Figure 3.6 Triplicate Ca-Cb data in mol L^{-1} as a function of pH correspond to 20 (◇), 30 (△) and 35 (□) g L^{-1} B. subtilis spore suspensions in a 0.1 M electrolyte at 25 oC. Solid lines show the global five-site model fit to each spore assay. The dashed line shows a theoretical, degassed 0.1 M electrolyte blank titration assuming an initial pH of 6.88. The pH buffering capacity of *B. subtilis* spores is evident relative to the modeled blank titration.

Because the SCM is based on a proton mass balance, DPA contamination may affect the model results by contributing to proton uptake in the experimental assays. The effects of DPA contamination in the proton adsorption data were estimated by calculating the stepwise exchange of protons over the course of the potentiometric titration assuming 20 μM DPA at the start of the titration. Under these assumptions there is a net uptake of protons by DPA protonation reactions over the course of an ITC analysis. The proton uptake calculated for each step of a 1 mL, 20 μM DPA titration is circa two orders of magnitude smaller than the moles of protons adsorbed in the lowest concentration spore suspension titration data (20 g L^{-1}). Based on our titration specific DPA models and the findings of Kapetas et al. (2011) the DPA contamination levels expected in our spore suspensions should not have a significant effect on SCM model results. Consequently, we did not make any explicit corrections for DPA in the SCM derivation.

Table 3.1 F-test parameters and results comparing four and five site SCM fits. The five-site heat of protonation *p* value model shows a statically significant better fit that cannot be determined from the spore protonation SCM fits.

F-test model comparison	***Spore-Protonation NE-SCM***		***Heat of protonation model***	
Parameter	**4 site**	**5 site**	**4 site**	**5 site**
Sum-of-squares	3.07E-6	2.97E-6	76.72	37.66
Number of model parameters	9	11	12	15
Number of data points	97		91	
p-value	0.2408		<0.0001	

Site concentrations and stability constants were derived for a unique set of ligands by generating best fit models for triplicate spore-proton adsorption C_a-C_b data spanning from pH 3 to 9.5. Best fit models were generated in MATLAB using non-linear least squares fitting with the Newton-Raphson method. Parameters from each model fit were averaged to produce one global model describing all three data sets (Fig. 3.6). A surface complexation model with four unique proton bonding sites was sufficient to describe the net spore protonation data. Models

with fewer unique proton active ligands produced significantly poorer fits to the data. Applying a five-site model to the spore protonation data did not significantly improve the model fit (Fig. 3.4 and 3.6). We compared the four and five-site model fits using the extra sum-of-squares F-test. The F-test determines the statistical improvement from and validity of a more complex model relative to a simpler version based on the degrees of freedom and difference between the sum-of squares calculated for each model fit to the data. F-test results comparing the four and five-site SCMs produced a *p* value of 0.2408 (Table 3.1), suggesting no statistical difference between the model fits. Global four and five-site model parameters, with site concentrations normalized to moles of protons adsorbed per gram spores (mol g^{-1}), are reported in Tables 3.2 and 3.3, with subscripts $i/4$ and $i/5$ denoting model specific sites, respectively. 1σ errors in Tables 3.2 and 3.3 reflect the global model fits to all three data sets. Total protonation site concentration for the four and five-site models are 300 ± 35 and 316 ± 110 μmol g^{-1} spores respectively.

Table 3.2 Four-site adsorption model parameters for *B. subtilis* spore surface protonation in a 0.1 M electrolyte at 25 degrees C from a five-site SMC according to the reaction $R\text{-}L_i^- + H^+ \rightarrow R\text{-}L_iH$.

Spore Site	$\log K_i$[a]	[R-L_i] (umol g^{-1})[a]	ΔG_i (kJ mol^{-1})[a]	ΔH_i (kJ mol^{-1})[a]	ΔS_i (J mol^{-1})[a]
R-$L_{1/4}$	3.7 ± 0.1	108 ± 7	-21.1 ± 0.6	-9.8 ± 1.0	38 ± 6
R-$L_{2/4}$	5.4 ± 0.2	68 ± 8	-30.6 ± 1.2	-7.3 ± 1.2	78 ± 8
R-$L_{3/4}$	7.0 ± 0.2	62 ± 8	-40.0 ± 1.2	-27.0 ± 1.2	43 ± 8
R-$L_{4/4}$	9.1 ± 0.3	62 ± 12	-51.8 ± 1.7	-38.7 ± 1.3	44 ± 10

[a] errors are 1σ

Table 3.3 Five-site adsorption model parameters for *B. subtilis* spore surface protonation in a 0.1 M electrolyte at 25 degrees C from a five site SMC according to the reaction $R\text{-}L_i^- + H^+ \rightarrow R\text{-}L_iH$.

Spore Site	$\log K_i$[a]	[R-L_i] (umol g^{-1})[a]	ΔG_i (kJ mol^{-1})[a]	ΔH_i (kJ mol^{-1})[a]	ΔS_i (J mol^{-1})[a]
R-$L_{1/5}$	3.4 ± 0.5	83 ± 30	-19.5 ± 2.6	-9.3 ± 1.2	+34 ± 13
R-$L_{2/5}$	4.5 ± 0.6	64 ± 30	-25.9 ± 3.2	-9.3 ± 1.2	+56 ± 15
R-$L_{3/5}$	6.0 ± 0.4	60 ± 14	-34.4 ± 2.3	-10.3 ± 1.0	+81 ± 11
R-$L_{4/5}$	7.5 ± 0.4	46 ± 14	-42.6 ± 2.6	-35.6 ± 1.1	+23 ± 13
R-$L_{5/5}$	9.3 ± 0.5	63 ± 23	-53.2 ± 3.0	-39.8 ± 1.0	+45 ± 14

[a] errors are 1σ

3.4.3.4 Calorimetric Modeling

Enthalpies of protonation (ΔH_i) are related to Q_{corr} by the change in the number of moles of protonated spore sites ($\Delta n_{R-L_iH,n}$) with each step of the titration (n) as described by Eq. 3.6

Eq. 3.6 $$Q_{CORR,n} = \sum_1^i \Delta H_i \ \Delta n_{R-L_iH,n}$$

$\Delta n_{R-L_iH,n}$ values are calculated using the SCMs, simultaneous pH measurements, and volumes of acid added. These $\Delta n_{R-L_iH,n}$ values are used as independent variables in Eq. 3.6. We derive enthalpies of protonation by minimizing the difference between corrected heats and calculated heats with the Excel, non-linear optimization solver. 1σ errors were calculated from the covariance matrix.

Q_{corr} values from spore assays of three different concentrations, 20, 30 and 35 g L^{-1}, displayed little variation in the overall heat production as a function of spore concentration (Fig. 3.7). According to Eq. 3.6, adjusting Q_{corr} to account for spore concentration would require normalizing the data to concentration dependent, site specific $\Delta n_{R-L_iH,n}$ values. Consequently, we do not attempt to normalize or average the data in Fig. 3.7. $\Delta n_{R-L_iH,n}$ utilized in the enthalpy derivation take individual assay spore concentrations into account. The model fits plotted in

Fig. 3.7 are of an average spore concentration of 28.3 g L^{-1} for the three experimental assays. We chose to plot the averaged model results because variations in Q_{corr} for the different spore assays are small and pH dependent trends within each of the three model results are equivalent.

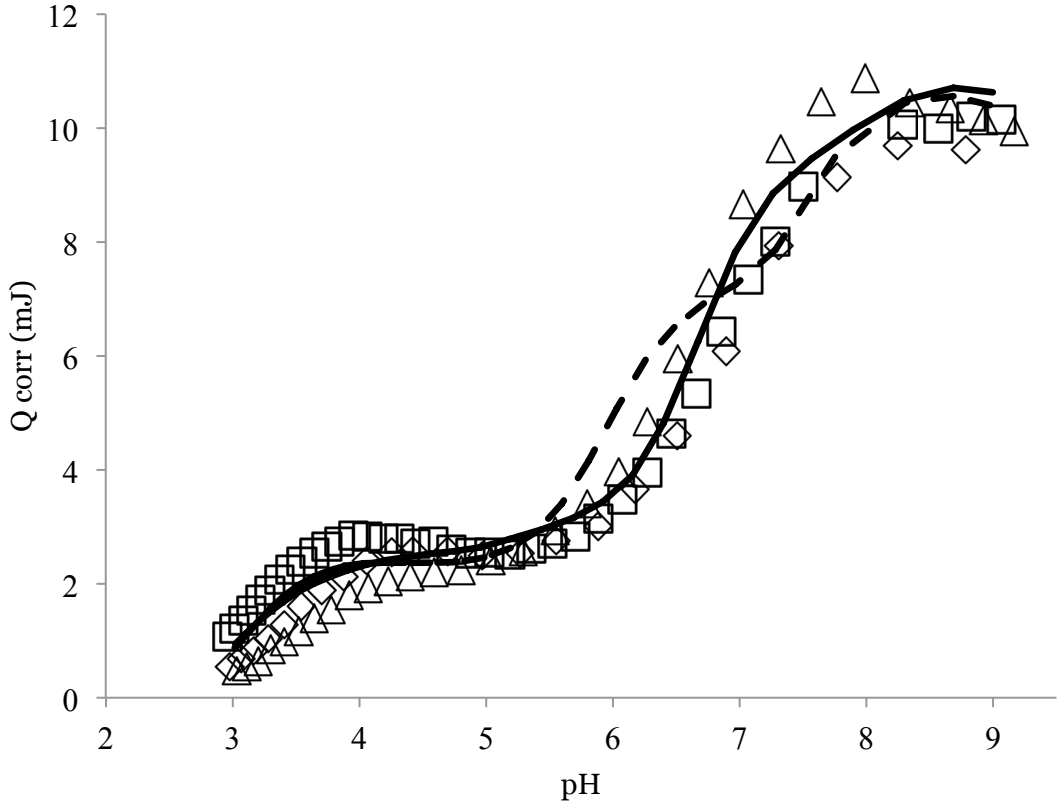

Figure 3.7 Corrected heats of B. subtilis spore surface protonation from triplicate ITC analyses of 20 (◇), 30 (△) and 35 (□) g L^{-1} spore suspensions in a 0.1 M electrolyte at 25 oC. Positive heats are exothermic. Solid and dashed curves show the averaged heat models from five and four site NE-SCM fits respectively.

Heats of protonation from DPA contamination have the capacity to affect Q_{corr} and the derivation of protonation enthalpies. Therefore, we calculated the stepwise heat production from DPA protonation assuming experimental titration parameters of a 20 μM DPA solution and enthalpies of DPA protonation, +3 kJ mol^{-1} and -2 kJ mol^{-1} for ΔH_1 and ΔH_2, respectively (Martell et al., 1998). All stepwise heats from DPA protonation are endothermic. The largest predicted heat absorption, approximately +9 μJ, is predicted at pH values circa pK_{a1} and is two

orders of magnitude smaller than the corrected heats of spore protonation. According to both heat and proton mass balance considerations, 20 μM DPA within the spore assays will have little to no effect on determining enthalpies of spore surface protonation and preclude the need for an additional correction factor in Q_{corr} (Eq. 3.1).

We attempted to model the corrected heat data (Q_{corr}) by generating best-fit enthalpies based on Δn_{R-LiH} values calculated from the four-site SCM model. Calculated protonation heats from the four-site model (Table 3.2) circa pH 7.5 were substantially lower than Q_{corr} data (Fig. 3.7). Carbonic acid and DPA contamination were ruled out as potentially significant heat producers. We resolved the discrepancy between calculated and observed heats by modeling the Q_{corr} data with best fit enthalpies corresponding to Δn_{R-L_iH} values calculated from the five-site NE-SCM (Table 3.3, Fig. 3.7). An F-test comparing the four and five-site heat of protonation model fits produced a p value of <0.0001, indicating a statistically significant improvement in the five-site model fit (Table 3.1).

3.4.3.5 Additional thermodynamic parameters

We calculated the site specific Gibbs energy of protonation (ΔG_i) for both the four and five-site model according to Eq. 3.7:

Eq. 3.7 $$\Delta G_i = -2.303RT\log K_i$$

where R is the gas constant and T is temperature in Kelvin. We calculated site specific change in entropies of protonation (ΔS_i) from the Gibbs energy (ΔG_i) and enthalpy of protonation (ΔH_i) based on Eq. 3.8:

Eq. 3.8 $$\Delta G_i = \Delta H_i - T\Delta S_i$$

We propagated errors through Eq. 3.7 and 3.8 to calculate 1σ errors for the Gibbs free energies and entropies of protonation.

3.4.4 Model Interpretations

3.4.4.1 Four versus five-site model comparison

The necessity of a five-site model to fit the observed heats of protonation may indicate the presence of an additional, highly exothermic, circumneutral site relative to the circumneutral log K (7.0) and corresponding enthalpy (27.0 kJ mol^{-1}) derived in the four-site model. The chemical signatures observed in the titration and protonation heat data and the discrepancy in the four-site heat of protonation model fit can be produced by multiple physical configurations. These include the presence of an additional, highly exothermic site with either (a) a proton adsorption log K value within close proximity (less than 2 log units) to other proton active site log Ks with less exothermic enthalpies, (b) a substantially lower site concentration that is below the titration sensitivity or shrouded by other protonation sites, or (c) a combination of the two conditions. The five-site NE-SCM fit to the protonation data produces an averaged model that most closely assumes condition (a) by effectively splitting the log K of site $L_{3/4}$ into two sites, $L_{3/5}$ and $L_{4/5}$ (Tables 3.2 and 3.3). The addition of a fifth site also results in the redistribution of acidic and circumneutral site concentrations over a wider log K range; 3.4-7.5 in the five-site model (Table 3.3), relative to the four-site model, 3.7 - 7.0 (Table 3.2). Corresponding best-fit enthalpies are able to more accurately reproduce the observed spore protonation heats due to the site concentration and log K redistribution in the five-site NE-SCM. The full range of predicted log Ks and total site concentration in both models are similar since they are constrained by the pH range encompassed by the titration data.

In this instance, the sensitivity of the ITC data to highly exothermic reactions reveals a level of complexity that is undetectable in the less sensitive titration data. The five-site SCM ascribes a significant concentration to the "additional" site, $L_{4/5}$. Based on the nearly equivalent

four-site protonation model fit, however, site $L_{4/5}$ in the five-site model may be an extraneous reaction in terms of its contributions to overall reactivity of the spore surface. Additional work including heats of metal adsorption may help elucidate the identity and relative contributions of $L_{3/5}$ and $L_{4/5}$ in overall spore reactivity.

The four and five-site spore protonation models have some distinct similarities. Total site concentration predicted in the four and five-site models are statistically equivalent at 300 ± 35 and 316 ± 110 μmol g^{-1} spores, respectively. Enthalpies of protonation in both models become increasingly exothermic with increasing log K_i. This is in accordance with the raw heats of protonation (Fig. 3.1). The highest log K_i site in each model, $L_{4/4}$ and $L_{5/5}$, and their corresponding site concentrations, enthalpies and entropies of protonation are statistically equivalent. Notably, these sites, also exhibit the most autonomous log K values at nearly two log units above the next lowest log K_i. The consistency between $L_{4/4}$ and $L_{5/5}$ provides evidence supporting the presence of ligands that are chemically distinct from those acting at a lower log K.

Cox et al. (1999) and Sokolov et al. (2001) proposed five-site models describing protonation data for *B. subtilis* and *Shewanella putrefaciens,* respectively, using the linear programming method (LPM). This method fixes pK_as at regular intervals and optimizes the site concentration at each pKa interval to fit each individual titration. The final, global model is an average of all pKa zones with site concentrations above zero for all replicate titrations. Unlike SCM, LPM does not provide the minimum number of unique sites required to describe the titration data and instead attempts to encompass site variability observed in all replicate titrations. We refrain from drawing direct comparisons between the five-site *B. Subtilis* vegetative cell protonation model proposed by Cox et al. (1999) due to differences in the modeling approach and pH range studied.

3.4.4.2 Model ligand interpretations

A large diversity of chemical environments can be found in a complex network of proteins and other organic molecules, such as the spore surface. These chemical micro-environments can produce variability in the thermodynamic behavior of proton active, amino acid side chains, referred to as R-groups. Proton active R-groups within secondary, tertiary and quaternary protein structures can be affected by surrounding amino acids and other organic molecules though hydrogen bonding, steric effects, Born effects, and electrostatic interactions (Dwyer et al., 2000; Thurlkill et al., 2006; Vasil'ev et al., 1998). Amino acid R-groups imbedded within a protein may experience large shifts in protonation log Ks relative to their intrinsic log K. This is in contrast to minimal alterations observed for protonation log K values measured for R-groups located at protein surfaces (Dwyer et al., 2000; Thurlkill et al., 2006). The sensitivity of protonation behavior to the ligand bonding environment may serve to spread out the protonation log K range over which a specific R-group acts. Consequently, amino acid acidity constant literature values only provide a starting point for determining the pH region over which an amino acid R-group will react in situ.

The *B. subtilis* spore coat is composed primarily of proteins with some lipids and carbohydrates (Driks, 1999; Driks, 2002; Pandey and Aronson, 1979). Proton active R-groups on the amino acids that make up *B. subtilis* spore coat proteins are likely candidates for spore proton adsorption. The dominant amino acids making up the *B. subtilis* spore coat include glutamic acid, aspartic acid, cysteine, lysine and tyrosine (Bhattacharyya and Bose, 1967; Pandey and Aronson, 1979). Glutamic and aspartic acid both have carboxyl R-groups with log K values of 4.1 - 4.5 and 3.2 - 4.7 respectively (Cohn and Edsall, 1943; O'neil, 2001; Thurlkill et al., 2006; Vasil'ev et al., 1998). Enthalpies of carboxyl R-group protonation on glutamic and aspartic acid are slightly exothermic at -3.0 and -6.6 kJ mol^{-1} with entropies of +68 and +56 J mol^{-1} K^{-1}, respectively (Martell et al., 1998). Cysteine is characterized by a thiol R-group with a log K ranging from 7.4 to 10.8 (Bulaj et al., 1998; Cohn and Edsall, 1943; O'neil, 2001; Thurlkill et al.,

2006) depending on its chemical environment. The Cysteine thiol alone exhibits an exothermic protonation enthalpy around -35 kJ mol^{-1} and entropy of 79 J mol^{-1} K^{-1} (Martell et al., 1998). Tyrosine hosts a phenol R-group that is proton active in more basic solutions with a log K ca. 10 (Cohn and Edsall, 1943; Martell et al., 1998; O'neil, 2001; Thurlkill et al., 2006), and a protonation enthalpy and entropy of -26 kJ mol^{-1} and +103 J mol^{-1} K^{-1}, respectively (Martell et al., 1998). Lysine has an amine on its R-group with a log K circa 10.6 (Martell et al., 1998; Thurlkill et al., 2006) and a protonation enthalpy and entropy of -54 kJ mol^{-1} and +23 J mol^{-1} K^{-1} (Martell et al., 1998). Terminal amines typically exhibit lower log Ks ranging from 8.1 to 9.6 with protonation enthalpies and entropies ranging from -38 to -47 kJ mol^{-1} and +17 to +51 J mol^{-1} K^{-1}. Terminal amines within peptides versus unbound amino acids such as Alanine show a significant drop in protonation log K and entropy from 10.1 to 8.5 and 40.4 to 9.8 J mol^{-1} K^{-1}, respectively (Martell et al., 1998; Vasil'ev et al., 1998). Phosphates are another common proton active ligand found on organic surfaces and may be present on the spore coat. Phytic acid, a multifunctional phosphate, hosts a range of protonation log Ks from 9.6 to 2.8 with enthalpies that become less exothermic and more endothermic, -12 to +5 kJ mol^{-1}, with subsequent protonation steps. Corresponding entropies of phytic acid protonation decrease from +144 to +72 J mol^{-1} K^{-1} (De Stefano et al., 2004).

Is it also likely that protons penetrate into and react with the spore cortex due to increased permeability of the spore inner membrane at acidic pH. Passive spore DPA release, observed at acidic and alkaline pH in this research and by Setlow et al. (2002), suggests chemical diffusion between the external solution and spore cortex. DPA within the spore cortex may contribute to proton adsorption observed at low pH values. DPA carboxyl groups have log K values of 4.66 and 2.07, protonation enthalpies of +3 and -2 kJ mol^{-1}, and protonation entropies of 102 J mol^{-1} K^{-1} and 29 J mol^{-1} K^{-1}, respectively (Martell et al., 1998).

The log Ks, exothermic enthalpies and entropies of sites $L_{1/4}$, $L_{1/5}$ and $L_{2/5}$ resemble carboxyl group protonation on amino acid R-groups or internal, cortex DPA. The more

exothermic nature of site $L_{3/5}$ reflects the thermodynamic properties of phosphate protonation in phytic acid. Protonation of $L_{4/5}$ more closely resembles the exothermic behavior and log K range of a thiol amino acid R-group. Site $L_{3/4}$ may display a mixture of two thermodynamically unique sites, $L_{3/5}$ and $L_{4/5}$. From our data we cannot, however, delineate the true mixing ratio of proton active sites with unique thermodynamic properties in this pH range. The log K, entropies and highly exothermic enthalpies of sites $L_{5/5}$ and $L_{4/4}$ are consistent with the chemical behavior of thiol and amine protonation reactions like those observed with cysteine and lysine. Phenolic protonation entropies are substantially higher than those reported for spore sites $L_{5/5}$ and $L_{4/4}$. This does not, however, discount the presence of phenol groups on the spore surface. Our positive entropies for spore surface protonation may reflect the dehydration of polarized ligands upon protonation.

3.4.5 Comparison to *B. subtilis* cell protonation

Fein et al. (2005) and Gorman-Lewis et al. (2006) utilized similar titration and ITC analyses to study *B. subtilis* vegetative cell surface reactivity. Both cell surface titration and ITC data, covering a pH range equivalent to the data reported in this paper, were described using a four-site NE-SCM (Table 3.4). The model derived total cell surface site concentration was 311 μmol g^{-1} (Fein et al., 2005). On a per gram (wet weight) basis our model indicates that *B. subtilis* cells and spores host similar total proton active site concentrations. The spore surface area, however, may be up to four times larger (He and Tebo, 1998) and the total spores per gram wet-weight may be higher relative to their cell counterpart. From this we can assume the density of spore surface proton active sites is lower than cell surface densities. This is in agreement with the more hydrophobic nature of spores (Sacks and Alderton, 1961).

Table 3.4: Site specific adsorption parameters for *B. subtilis* cell surface protonation in a 0.1M electrolyte at 25 degrees C derived from a four site SMC according to the reaction $R\text{-}L_i^- + H^+ \rightarrow R\text{-}L_iH$.

Cell Site	$\log K_i$[a,b]	$[R\text{-}L_i]$ (umol g^{-1})[a,b]	ΔG_i^o (kJ mol^{-1})[a,c]	ΔH_i^o (kJ mol^{-1})[a,c]	ΔS_i^o (J mol^{-1})[a,c]
$R\text{-}L_1$	3.3 ± 0.2	81 ± 16	-18.8 ± 1.1	-3.5 ± 0.2	+51 ± 4
$R\text{-}L_2$	4.8 ± 0.1	112 ± 36	-27.4 ± 0.6	-4.2 ± 0.2	+78 ± 4
$R\text{-}L_3$	6.8 ± 0.3	44 ± 13	-38.8 ± 1.7	-15.4 ± 0.9	+79 ± 5
$R\text{-}L_4$	9.1 ± 0.2	74 ± 21	-51.9 ± 1.1	-35 ± 2	+60 ± 20

[a] errors are 1 σ
[b] from Fein et al. (2005)
[c] from Gorman-Lewis et al. (2006)

We calculated *p* values using a two-tailed T-test to determine statistical differences between the thermodynamic SCM parameters in both the four and five-site spore models and the cell model (Table 3.5). We assumed equal variance and replicates (n=3) for each model parameter and 4 degrees of freedom. From the t-test values we determined the *p* values comparing site-specific thermodynamic model parameters for spore versus cell surface protonation. A *p* value in excess of 0.05 signifies statistically similar model values.

p values comparing cell four-site and spore five-site SCM log K values suggest overall similarities in the distribution of log Ks over both data sets. log K_2 and log K_3 in the cell versus log $K_{2/4}$ and log $K_{3/5}$ in the spore exhibit the most significant differences with *p* values of 0.01 and 0.05, respectively. All comparisons between spore and cell site concentrations resulted in *p* values above the critical *p* value of 0.05 (Table 3.5). These results suggest a statistical similarity between *B. subtilis* spore and cell buffering capacities per gram (wet weight) of biomass with minimal significant differences in SCM log K and site concentration distributions. Significant differences between the enthalpies and entropies of protonation, however, reveal variations in the chemical nature of spore surface sites relative to their cell counterparts. All *p* values comparing surface protonation enthalpies between four and five-site spore SCMs and its cell counterpart were below 0.05, except $\Delta H_{4/4}$ and ΔH_4 in the spore and cell (p = 0.055),

respectively. These *p* values indicate that *B. subtilis* spore protonation reactions are more exothermic than the cell surface at all pH studied. The most statistically significant differences between site specific entropies were between spore site entropies $\Delta S_{4/5}$ and $\Delta S_{3/4}$ versus cell site ΔS_3, (p = 0.002 and 0.003, respectively). This relationship suggests spore SCM site $L_{3/5}$ may share more chemical similarities with site L_3 in the cell. The "additional" highly exothermic site ($L_{4/5}$) circa pH 7 in the spore SCM may indicate the presence of a thiol on the spore surface that is absent in the cell SCM.

Table 3.5 *p* values based on a two-tailed T-test comparing *B. subtilis* cell and spore protonation thermodynamic SCM parameters.

Parameter Comparison				
Cell	**Spore (5 site)**	***p* value**	**Spore (4 site)**	***p* value**
$\log K_1$	$\log K_{1/5}$	0.764	$\log K_{1/4}$	0.036
$\log K_2$	$\log K_{2/5}$	0.441	$\log K_{2/4}$	0.010
$\log K_3$	$\log K_{3/5}$	0.050	$\log K_{3/4}$	0.391
$\log K_3$	$\log K_{4/5}$	0.072	-	-
$\log K_4$	$\log K_{5/5}$	0.555	$\log K_{4/4}$	1.000
$[L_1]$	$[L_{1/5}]$	0.924	$[L_{1/4}]$	0.055
$[L_2]$	$[L_{2/5}]$	0.151	$[L_{2/4}]$	0.108
$[L_3]$	$[L_{3/5}]$	0.221	$[L_{3/4}]$	0.111
$[L_3]$	$[L_{4/5}]$	0.865	-	-
$[L_4]$	$[L_{5/5}]$	0.574	$[L_{4/4}]$	0.439
ΔH_1	$\Delta H_{1/5}$	0.001	$\Delta H_{1/4}$	0.000
ΔH_2	$\Delta H_{2/5}$	0.002	$\Delta H_{2/4}$	0.012
ΔH_3	$\Delta H_{3/5}$	0.003	$\Delta H_{3/4}$	0.000
ΔH_3	$\Delta H_{4/5}$	0.000	-	-
ΔH_4	$\Delta H_{5/5}$	0.021	$\Delta H_{4/4}$	0.055
ΔS_1	$\Delta S_{1/5}$	0.096	$\Delta S_{1/4}$	0.035
ΔS_2	$\Delta S_{2/5}$	0.070	$\Delta S_{2/4}$	1.000
ΔS_3	$\Delta S_{3/5}$	0.789	$\Delta S_{3/4}$	0.003
ΔS_3	$\Delta S_{4/5}$	0.002	-	-
ΔS_4	$\Delta S_{5/5}$	0.218	$\Delta S_{4/4}$	0.136

B. subtilis spores may be a good candidate for a first-order, vegetative *B. subtilis* cell surface proxy based on the similarities between spore and cell log Ks and per gram site concentration values. Using vegetative bacterial cells to study the long-term effects of bacterial

surfaces on an aqueous system can be problematic due to cell metabolism and lysis (Lee and Fein, 2000; Wightman and Fein, 2004). Spore stability and dormancy, coupled with surface reactivity parameters similar to cells, provide a robust tool for isolating and quantifying the long-term effects of surface complexation on a system. Borrok et al. (2004; 2005) suggest a universal adsorption edge that adequately defines the cell surface protonation behavior of multiple bacterial species including *B. subtilis*. By extrapolation, *B. subtilis* spores may serve as a proxy for a consortium of bacterial species in long-term experiments studying the effects of surface complexation reactions on natural and engineered systems.

3.5 Conclusions

We studied *B. subtilis* spore-proton adsorption reactions though coupled potentiometric titration and isothermal titration calorimetry analyses. Spore-proton adsorption occurred over the entire pH range studied (pH 3-9) and full protonation of the surface was not achieved. Corrected heats of protonation (Q_{corr}) were exothermic over the experimental pH range and increased with increasing pH. Surface complexation modeling was used to describe the potentiometric data and generate best fit, site specific log Ks and site concentrations. A four-site SCM was required to describe the potentiometric data. The model fit was not significantly improved by adding a fifth site. From the four and five-site SCMs, we generated site specific best fit enthalpies to describe Q_{corr}. Four-site SCMs failed to predict sufficiently large heats circa pH 7 (Fig. 3.7). We rectified this misfit by describing Q_{corr} with a five-site SCM (Fig. 3.7). The need for a five-site model to fit the ITC data suggests the presence of a highly exothermic site that cannot be detected in potentiometric titrations due to (a) a log K that significantly overlaps other site log Ks, (b) a very low-concentration site, or (c) a combination of the two conditions. Coupling ITC data with potentiometric titrations provides a robust tool for discerning chemically unique sites with large exothermic, and potentially very endothermic, enthalpies that

are overlooked in the potentiometric data and best fit SCMs. ITC data also suggests *B. subtilis* spore surface protonation reactions are more exothermic than their cell counterparts. Although we cannot discern the physical identity of SCM generated sites described in this paper, the thermodynamic parameters provide a starting point for understanding spore surface protonation reactions on a molecular scale. The site-specific spore protonation parameters generated in this research also provide a framework for modeling spore-metal adsorption and predicting the influence of spore surface adsorption reactions on macro-scale systems.

3.6 References

Bethke, C. M. and Brady, P. V., (2000) How the Kd Approach Undermines Ground Water Cleanup. *Ground Water* **38**, 435-443.

Bhattacharyya, P. and Bose, S. K., (1967) Amino acid composition of cell wall and spore coat of *Bacillus subtilis* in relation to mycobacillin production. *J. Bact.* **94**, 2079-80.

Borrok, D., Fein, J. B., and Kulpa, C. F., (2004) Proton and Cd adsorption onto natural bacterial consortia: Testing universal adsorption behavior. *Geochim. Cosmochim. Acta* **68**, 3231-3238.

Borrok, D., Turner, B. F., and Fein, J. B., (2005) A universal surface complexation framework for modeling proton binding onto bacterial surfaces in geologic settings. *Am J Sci* **305**, 826-853.

Bulaj, G., Kortemme, T., and Goldenberg, D. P., (1998) Ionization -- Reactivity Relationships for Cysteine Thiols in Polypeptides. *Biochem.* **37**, 8965.

Calí, R., Rizzarelli, E., Sammartano, S., and Pettit, L. D., (1980) Thermodynamics of protonation of some dicarboxylic acids containing heteroatoms from group 6B. *Thermochim. Acta* **35**, 169-179.

Cohn, E. J. and Edsall, J. T., (1943) *Proteins, amino acids and peptides as ions and dipolar ions*. Reinhold Publishing Corporation, New York.

Cox, J. S., Smith, D. S., Warren, L. A., and Ferris, F. G., (1999) Characterizing Heterogeneous Bacterial Surface Functional Groups Using Discrete Affinity Spectra for Proton Binding. *Environ Sci & Tech* **33**, 4514-4521.

De Stefano, C., Milea, D., and Sammartano, S., (2004) Speciation of phytate ion in aqueous solution: Thermodynamic parameters for protonation in NaCl. *Thermochim. Acta* **423**.

Driks, A., (1999) *Bacillus subtilis* spore coat. *Microbiol Mol Biol Reviews* **63**, 1-+.

Driks, A., (2002) Maximum shields: the assembly and function of the bacterial spore coat. *Trends Microbiol.* **10**, 251-254.

Dwyer, J. J., Gittis, A. G., Karp, D. A., Lattman, E. E., Spencer, D. S., Stites, W. E., and GarcÃ-a-Moreno E, B., (2000) High Apparent Dielectric Constants in the Interior of a Protein Reflect Water Penetration. *Biophys. J.* **79**, 1610-1620.

Fein, J. B., Boily, J.-F., Yee, N., Gorman-Lewis, D., and Turner, B. F., (2005) Potentiometric titrations of *Bacillus subtilis* cells to low pH and a comparison of modeling approaches. *Geochim. Cosmochim. Acta* **69**, 1123-1132.

Gorman-Lewis, D., Fein, J. B., and Jensen, M. P., (2006) Enthalpies and entropies of proton and cadmium adsorption onto *Bacillus subtilis* bacterial cells from calorimetric measurements. *Geochim. Cosmochim. Acta* **70**, 4862-4873.

Gould, G. W. and Hurst, A., (1969) *The bacterial spore*. Academic Press, London, New York,.

Harrold, Z., Hertel, M. R., and Gorman-Lewis, D., (2011) Optimizing *Bacillus subtilis* spore isolation and quantifying spore harvest purity. *J. Microbiol.*

He, L. M. and Tebo, B. M., (1998) Surface charge properties of and Cu(II) adsorption by spores of the marine *Bacillus* sp. strain SG-1. *Appl. Environ. Microb.* **64**, 1123-1129.

Hong, H. A., To, E., Fakhry, S., Baccigalupi, L., Ricca, E., and Cutting, S. M., (2009) Defining the natural habitat of *Bacillus* spore-formers. *Research in Microbiol.* **160**, 375-379.

Jespersen, N. D. and Jordan, J., (1970) Thermometric Enthalpy Titration of Proteins *Anal. Lett.* Taylor & Francis.

Kapetas, L., Ngwenya, B. T., Macdonald, A. M., and Elphick, S. C., (2011) Kinetics of bacterial potentiometric titrations: The effect of equilibration time on buffering capacity of Pantoea agglomerans suspensions. *J. Colloid Interf. Sci.* **359**, 481-486.

Kelly, S. D., Kemner, K. M., Fein, J. B., Fowle, D. A., Boyanov, M. I., Bunker, B. A., and Yee, N., (2002) X-ray absorption fine structure determination of pH-dependent U-bacterial cell wall interactions. *Geochim. Cosmochim. Acta* **66**, PII S0016-7037(02)00947-X.

Lee, J.-U. and Fein, J. B., (2000) Experimental study of the effects of *Bacillus subtilis* on gibbsite dissolution rates under near-neutral pH and nutrient-poor conditions. *Chem. Geo.* **166**, 193-202.

Martell, A. E., National Institute of, S., and Technology . Standard Reference, D., (1998) NIST critically selected stability constants of metal complexes. U.S. Dept. of Commerce, National Institute of Standards and Technology, Standard Reference Data Program, Gaithersburg, MD.

Nicholson, W. L., Munakata, N., Horneck, G., Melosh, H. J., and Setlow, P., (2000) Resistance of *Bacillus* endospores to extreme terrestrial and extraterrestrial environments. *Microbiol Mol Biol R* **64**, 548-+.

O'Neil, M. J., (2001) *The Merck index : an encyclopedia of chemicals, drugs, and biologicals*. Merck, Whitehouse Station, N.J.

Pandey, N. K. and Aronson, A. I., (1979) Properties of the *Bacillus subtilis* spore coat *J. Bacteriol.* **137**, 1208-1218.

Revis, N. W., Hadden, C. T., and Edenborn, H., (1997) Removal of dissolved heavy metals and radionuclides by microbial spores *Other Information: PBD: [1997].*

Rode, L. J. and Foster, J. W., (1966) Quantitative Aspects of Exchangeable Calcium in Spores of *Bacillus* megaterium. *J. Bacteriol* **91**, 1589-1593.

Sacks, L. E. and Alderton, G., (1961) Behavior of bacterial spores in aqueous polymer two phase systems. *J. Bacteriol.* **82**, 331-341.

Scott, I. R. and Ellar, D. J., (1978) Study of calcium dipicolinate release during bacterial spore germination by using a new, sensitive assay for dipicolinate. *J. Bacteriol.* **135**, 133-137.

Selinummi, J., Seppälä, J., Yli-Harja, O., and Puhakka, J. A., (2005) Software for quantification of labeled bacteria from digital microscope images by automated image analysis. *BioTechniques* **39**, 859-63.

Setlow, B., Loshon, C., Genest, P., Cowan, A., Setlow, C., and Setlow, P., (2002) Mechanisms of killing spores of *Bacillus subtilis* by acid, alkali and ethanol. *J App Microbiol* **92**, 362-375.

Setlow, P., (2006) Spores of *Bacillus subtilis*: their resistance to and killing by radiation, heat and chemicals. *J. of Appl Microbiol* **101**, 514-525.

Setlow, P., (2003) Spore germination. *Current Opinion in Microbiology* **6**, 550-556.

Siala, A., Hill, I. R., and Gray, T. R. G., (1974) Populations of Spore-forming Bacteria in an Acid Forest Soil, with Special Reference to *Bacillus subtilis*. *J Gen Microbiol* **81**, 183-190.

Sokolov, I., Smith, D. S., Henderson, G. S., Gorby, Y. A., and Ferris, F. G., (2001) Cell surface electrochemical heterogeneity of the Fe(III)-reducing bacteria Shewanella putrefaciens. *Environ Sci & Tech* **35**, 341-7.

Thurlkill, R. L., Grimsley, G. R., Scholtz, J. M., and Pace, C. N., (2006) pK values of the ionizable groups of proteins. *Protein Sci* **15**, 1214-1218.

Tourney, J., Ngwenya, B. T., Mosselmans, J. W. F., Tetley, L., and Cowie, G. L., (2008) The effect of

extracellular polymers (EPS) on the proton adsorption characteristics of the thermophile *Bacillus* licheniformis S-86. *Chem Geol* **247**, 1-15.

Vasil'ev, V. P., Kochergina, L. A., and Gorboletova, G. G., (1998) Thermodynamics of Protolytic Equilibria in Aqueous Solutions of Biologically Active Ligands. *J Therm Anal Calorim* **54**, 311-315.

Warth, A. D., (1983) Determination of dipicolinic acid in bacterial spores by derivative spectroscopy. *Anal Biochem* **130**, 502-505.

Westall, J. C., Jones, J. D., Turner, G. D., and Zachara, J. M., (1995) Models for Association of Metal Ions with Heterogeneous Environmental Sorbents. 1. Complexation of Co(II) by Leonardite Humic Acid as a Function of pH and NaClO4 Concentration. *Environ Sci & Tech* **29**, 951-959.

Wightman, P. G. and Fein, J. B., (2004) The effect of bacterial cell wall adsorption on mineral solubilities. *Chem Geol* **212**, 247-254.

Williams, N. D. and Russell, A. D., (1993) Revival of biocide-treated spores of Bacillus subtilis. *The Journal of applied bacteriology* **75**, 69-75.

Chapter 4: Magnesium and silica- *Bacillus subtilis* endospore adsorption: investigating the influence of endospores on silicate weathering products

4.1 Abstract

Microbial surfaces are an intrinsic component in water-rock systems that have the capacity to influence major element speciation and geochemical processes such as mineral dissolution and precipitation. Most surface reactivity studies focus on metal adsorption to vegetative bacterial cells surfaces. Bacterial endospores, a prevalent component in some microbial populations, have surfaces that are chemically distinct from their vegetative cell counterpart. The major element adsorption capacity of the endospore surface is, however, poorly constrained. We investigate *Bacillus subtilis* endospore adsorption affinity of two major elements commonly found in primary silicates: magnesium and silica. Mg and Si – endospore adsorption is measured as a function of solution pH and element to endospore ratio and in aqueous systems containing both Mg and Si. pH dependent Mg – endospore adsorption is modeled according to a 4-site non-electrostatic surface complexation model (NE-SCM) described by Harrold et al. (2013, Chapter 3). Both 1_{site}:1_{Mg} and 2_{site}:1_{Mg} NE-SCMs provide good fits to the data. Modeling the Mg adsorption behavior for variable Mg: endospore ratios requires both 1_{site}:1_{Mg} and 2_{site}:1_{Mg} NE-SCMs. This suggests Mg-endospore adsorption includes both adsorption stoichiometries. Si-endospore adsorption is negligible under all conditions studied. Mg-endospore adsorption, however, increases in the presence of Si. This may be due to the formation of >Mg-Si-Mg ternary complexes. Assuming ternary complex formation occurs, a concomitant increase in Si adsorption is within analytical error and cannot be resolved. The results described herein suggest *B. subtilis* endospore Mg and Si adsorption behavior is similar to that of their vegetative cell counterparts despite variations in their surface properties. Direct

endospore-Mg adsorption is more likely to influence geochemical processes than endospore- Si adsorption.

4.2 Introduction

Microbes, an intrinsic component of water-rock systems, provide a reactive surface characterized by a variety of organic acid moieties capable of complexing a wide range of aqueous species. Extensive research addressing toxic and trace metal adsorption to microbial surfaces provides an array of models, including surface complexation parameters, which describe the chemical thermodynamics of microbe-metal adsorption (e.g. Daughney and Fein, 1998; Gorman-Lewis et al., 2005; Gorman-Lewis et al., 2013; Yee and Fein, 2001). These parameters serve to constrain the influence of microbe-ion adsorption on the fate of toxic and trace metals in bacteria-water-rock systems and provide insight on the chemical mechanisms underlying microbe-ion adsorption reactions. Few investigations, however, focus on measuring and modeling the capacity of major element adsorption onto microbial surfaces.

Microbially hosted major element adsorption is likely an intermediate step bridging primary mineral dissolution and the subsequent formation of secondary precipitates associated with microbial surfaces in bacteria-water-rock environments. These adsorption reactions have the capacity to enrich major ion concentrations at the microbial surface and may influence the speciation and chemical equilibrium within the bulk solution. It is therefore possible that the adsorption of major elements to microbial surfaces can influence both mineral dissolution rates and precipitation at the cell surface.

Primary silicate mineral weathering rates are a major factor controlling numerous geochemical phenomena including regional and global major element distributions. Increased dissolution rates associated with the presence of organic acids are observed for numerous silicate minerals with varying degrees of silica polymerization from quartz, a tectosilicate

(Bennett, 1991; Bennett et al., 1988; Vandevivere et al., 1994), to olivine, a common nesosilicate (Olsen and Rimstidt, 2008). Enhanced quartz and forsterite dissolution in the presence of organic acids with carboxylic acid moieties was attributed to the formation of a mineral surface complex, which lowered the activation energy of dissolution. An increase in quartz dissolution rate is accredited to a silica-carboxylic acid complex formed at circumneutral pH. A reasonable extrapolation of these findings would suggest that reactive, organic acid moieties present on the microbial surface have the capacity to influence silicate dissolution rates by complexing aqueous dissolution products or elements at the silicate mineral surface.

Microbial surface adsorption has the capacity to concentrate elements necessary for secondary mineral formation and may even act as a nucleation point for precipitation. Findings by Konhauser et al. (1993; 1994) show authigenic mineral and "gel-like" iron, aluminum and silica precipitates encrusting cells in riverine systems. Direct bacteria-silica adsorption is negligible, likely due to electrostatic repulsion between the negatively charged microbial surface and neutrally charged silicic acid that predominates in solutions at pH < 9 (Fein et al., 2002; Konhauser and Urrutia, 1999). Preliminary iron adsorption and iron-oxide precipitation onto the microbial envelope, however, provides a surface conducive to silica adsorption and is thus a precursor to subsequent silica gel and clay-like mineral precipitation at the microbial surface (Fein et al., 2002; Konhauser and Urrutia, 1999). Forming mineral precipitates by adsorbing and thus concentrating major elements at the microbial surface has implications in digenetic processes and the formation and preservation of microfossils.

The proteinaceous coat of *Bacillus subtilis* endospores exhibits an interesting chemical dichotomy characterized by both hydrophobic properties and reactive organic acid adsorption sites. Hydrophobicity of the endospore surface is high relative to their vegetative cell counterpart and enables endospore-cell separation based on a two-phase organic-electrolyte extraction process (Chapter 2, Harrold et al., 2011; Sacks and Alderton, 1961). Potentiometric titrations of *B. subtilis* endospores, however, reveal proton reactive organic acid moieties active

over an equivalent pH range and at similar concentrations as vegetative cells (Chapter 3, Harrold and Gorman-Lewis 2013). Despite endospore counts on par with their vegetative cell counter-part in some soils (Siala et al., 1974), bacterial endospore surface reactivity is a largely overlooked component in natural microbiomes.

The chemical dichotomy of endospore surfaces coupled with their ability to persist in a state of stasis for long periods of time make them an intriguing environmental component capable of influencing water-rock systems through direct and indirect microbe-mineral interactions. We investigate the potential for B. subtilis endospore surfaces to adsorb two major elements, Magnesium (Mg) and Silicon (Si), common in both primary silicates and secondary precipitates. Analyses aim to quantify adsorption as a function of pH and variable element:endospore ratios for each individual element. We also investigate the dynamics of multi-ion adsorption systems by measuring the influence Si concentration on Mg adsorption and vice versa. Mg pH adsorption edge data is modeled using the non-electrostatic surface complexation model (NE-SCM) described in Chapter 3 (Harrold and Gorman-Lewis, 2013).

4.3 Methods

4.3.1 *B. subtilis* endospore growth and isolation

We grew and isolated *B. subtilis* endospores based on the procedures described by Harrold et al. (2011). Briefly, we aseptically inoculated 3.5 mL of 3 % typticase soy broth (TSB) and 0.5 % yeast extract from *B. subtilis* cultures maintained on agar plates. Cultures were incubated for 24 h, subsequently transferred to 1 L of 0.3 % TSB and incubated for an additional 6 days at 32 ^{o}C prior to harvesting. We isolated the endospores with a two-phase, polyethylene glycol 4000 and potassium phosphate buffer separatory solution (Harrold et al., 2011). Endospores were washed in 0.1 M $NaClO_4$ and pelleted as previously described (Harrold et al.,

2011), prior to use in adsorption assays. The average spore harvest purity determined by Harrold et al. (2011) is 88 ± 11% (1σ standard deviation, n=22) with a median value of 93 %.

4.3.2 Adsorption Assays

We conducted three types of Si and Mg-endospore adsorption assays including (1) adsorption as a function of solution pH, (2) adsorption as a function of element:endospore ratio at circumneutral pH, and (3) adsorption in systems containing Mg and Si. We conduced duplicate assays for each adsorption permutation. All endospore suspensions for adsorption experiments were prepared in a 25 mM $NaClO_4$ electrolyte, made with 18 MΩ cm^{-1} H_2O, to buffer changes in ionic strength. Endospore suspension concentrations are provided in grams of wet weight endospores per liter of electrolyte (g L^{-1}). Suspension pH was determined using an Orion 8103BN Ross semi-micro combination pH electrode calibrated with 4 NIST standards.

Total Si for each adsorption assay was added from a 1000 mg L^{-1} Silicon SPEX CertiPrep standard (Article Number: PLSI9A-2X). Silicon in the SPEX standard is added in the form of sodium metasilicate nonahydrate ($Na_2SiO_3 \bullet 9H_2O$) which is characterized by structurally discrete silica tetrahedral anions ($Na_2SiO_2(OH)_2 \bullet 8H_2O$) (Wells, 1986). Based on the predicted speciation of Si within the experimental assays, references to Si hereafter imply the presence of silicic acid ($Si(OH)_4$), unless otherwise noted. Mg was added from a 1000 mg L^{-1} ICP standard (Ricca Chemical Co, Cat# AMGIKN-500) in 1 % HNO_3. NO_3^- is believed to be an inert component in the assays and is not considered further in the chemical speciation or models.

We measured Si adsorption as a function of pH using a 1.2 g L^{-1} endospore suspension and a total silica concentration ($[Si]_{total}$) of 35.9 μM. An initial endospore-silica suspension was created by gravimetric additions of electrolyte, endospores and Si standard. Aliquots (10 to 15 mL) of the homogenized suspension were pH adjusted with up to 30 μL of HClO4 or NaOH to achieve a range of solution pH from 3 to 10. Volume change due to acid and base additions is

less than 0.3 %. pH adjusted aliquots were equilibrated for 2 h prior to measuring the equilibrium pH and filtering with a 0.22 μm polycarbonate Millipore, Isopore™ membrane filter. Filtered samples (5 to 10 mL final volume) were basified with 20 μL of 8 M NaOH to prevent silica polymerization prior to analysis.

Assays testing Si adsorption as a function of Si:endospore ratio at circumneutral pH were conducted similarly with an initial spore suspension of 0.66 g L^{-1}. Suspension aliquots (13 mL) were amended with additions of 1000 mg L-1 Si standard to cover a range of total Si from 16 to 703 μM. All suspension aliquots and Si additions were made gravimetrically. Total Si and endospore concentrations, and thus the element:endospore ratio, was calculated from the gravimetric serial data for each aliquot. Aliquot pH was adjusted to 7.5 ± 0.4 (2σ) with acid and base additions of 40 μL or less. Dilution due to acid and base additions is less than 0.3 %. Following a 2 h equilibration period, each aliquot was filtered and basified as described above.

We determined pH-dependent Mg adsorption for a 0.30 g L^{-1} endospore suspension with a total Mg concentration of 41.5 μM. The effect of variable Mg:endospore ratios at pH 7.3 ± 0.3 (2σ) were measured for an initial endospore concentration of 0.66 g L^{-1} and total Mg ranging from 0.96 μM to 399.25 μM. Methods for measuring Mg adsorption as a function of pH and Mg:endospore ratio are equivalent to those described above for Si adsorption, except filtered Mg samples (5 to 10 mL) are acidified with 20 μL of triple distilled, trace metal free 10 M HNO_3. We also tested Mg adsorption reversibility following the initial 2 h aliquot equilibration step by acidifying a portion of select circumneutral to high pH samples to pH between 3.5 and 4.3. Each pH-adjusted sample was re-equilibrated for 2 h prior to filtration and acidification.

The effect of a multi-element system containing Si and Mg, on endospore adsorption was determined by fixing the concentration of one element and varying the element: endospore ratio of the other. An initial endospore suspension was made with gravimetric additions of electrolyte, endospores and the fixed element standard. Aliquots (14 mL) were amended with

gravimetric additions of the counter element and suspension pH was adjusted to 7.2 ± 0.7 (2σ) and 7.1 ± 0.4 (2σ) for variable Mg- and Si:endospore ratio assays, respectively, as previously described. Following a 2 h equilibration phase, samples were filtered with 0.22 μm polycarbonate Millipore, Isopore™ membrane filter and acidified with 20 μL of triple distilled, trace metal free 10 M HNO_3 prior to analysis.

4.3.3 Elemental Analyses

Samples with element concentrations above 5 ppm were diluted gravimetrically with 18 MΩ cm^{-1} H_2O and 50 μL of triple distilled, trace metal free 10 M HNO_3. All samples were measured on an inductively coupled plasma optical emission spectrometer (ICP-OES). The instrument was calibrated with four, multi-element, Si and Mg standards encompassing the sample concentration range and matrix matched to the highest electrolyte concentration of 25 mM $NaClO_4$. Non-linear calibration curves exhibited a correlation coefficient of 0.99 or better. We analyzed samples using a sample-standard bracketing approach with triplicate sample reads. Quality control was maintained by monitoring errors in the bracketed standard analyses. Errors on all bracketed standard analyses were 10 % or lower. Original sample concentrations are calculated from gravimetric dilution data. Errors for Mg and Si adsorption data are propagated assuming a ± 0.0005 g absolute error in gravimetric data and a 7-10 % relative error for ICP-OES data depending on the errors observed for bracketed standard analyses.

4.4 Results and Discussion

4.4.1 Dipicolinic acid

The bacterial endospore core contains a large reservoir of pyridine–2,6 dicarboxylic acid (dipicolinic acid, DPA) equivalent to approximately 10% of their total dry weight (Setlow, 2003;

Warth, 1983). DPA is a diprotic acid with $pK_{a,1}$ and $pK_{a,2}$ of 2.07 and 4.66, respectively. Within the endospore core, DPA is believed to exist as a 1:1 chelate with Ca^{2+} and, to a lesser extent, other divalent cations such as Mg^{2+} (Setlow, 2006). Upon endospore germination, DPA is rapidly released into solution along with its divalent cation counterpart at concentrations upwards of 450 μM g^{-1} dry weight endospores (Scott and Ellar, 1978). DPA released into the adsorption assays could effectively compete with endospore adsorption by complexing Mg and, to a much lesser degree, Si. *B. subtilis* endospores, however, are shown to be stable in a 0.1 M $NaClO_4$ electrolyte for 4+ h without undergoing germination (Harrold and Gorman-Lewis, 2013). It is therefore unlikely that germination occurred within our experimental assays.

A second, slower DPA leaching processes linked to solution pH has been observed (Chapter 3, Harrold and Gorman-Lewis, 2013) and may be related to the acidic break down of membranes within the endospore (Setlow et al., 2002). According to Harrold and Gorman-Lewis (2013), a 35 g L^{-1} B. subtilis endospore suspension incubated for 4 h at pH 3 and 6.5, leached 15.9 ± 0.4 μmol kg^{-1} and 4.9 ± 1.0 μmol kg^{-1} DPA (1σ error), respectively. Endospore concentrations in the analyses described herein range from 1.2 to 0.3 g L^{-1}, one to two orders of magnitude lower than the concentrations described by Harrold and Gorman-Lewis (2013). Assuming DPA leaches linearly over time, we predict a maximum DPA contamination on the order of 0.27 μM for a 1.2 g L^{-1} endospore suspension equilibrated at pH 3 for 2 h. A DPA concentration of 0.27 μM is approximately two orders of magnitude below the total Mg and Si of the pH dependent adsorption assays, 41.5 μM and 35.9 μM, respectively. The lowest Mg and Si concentrations, approximately 1 μM, are from assays with 0.66 g L^{-1} endospore suspensions equilibrated at pH approximately 7.5 for 2 h. DPA release at circumneutral pH is much slower relative to low pH systems (Chapter 3, Harrold and Gorman-Lewis, 2013). We estimate 0.05 μM DPA contamination in a 0.66 g L^{-1} endospore suspension equilibrated for 2 hours at pH 6.5. Based on these estimates we expect DPA contamination is small relative to total Mg and Si

concentrations and does not have a large effect on endospore adsorption behavior in our experimental assays.

4.4.2 Mg – endospore adsorption

4.4.2.1 pH dependent Mg-endospore adsorption

We measured Mg–endospore adsorption as a function of pH ranging from 3.4 to 9.7 for a 0.30 g L^{-1} endospore suspension with a total Mg concentration ($[Mg]_{total}$) of 41.5 μM (Fig. 4.1). A 25 mM $NaClO_4$ background electrolyte was used to buffer changes in ionic strength. Mg adsorbed is calculated from the difference of $[Mg]_{total}$ and Mg remaining in the supernatant. Mg-endospore adsorption below pH 4.7 is negligible. Above pH 4.7 Mg adsorption increases steadily, reaching a high at 15.5 μM, or 37.3 % adsorbed at the highest reported equilibrium pH, 9.73 (Fig. 4.1). Mg adsorption was completely reversible for select samples initially equilibrated at pH 9.7, 9.3, 7.5 and 7.1 and re-equilibrated to pH between 3.6 and 4.3 (~0 % adsorption, data not shown).

4.4.2.2 Mg:endospore ratio dependent adsorption

We measured Mg-endospore adsorption as a function of Mg:endospore ratio at pH 7.3 ± 0.3 (2σ) by increasing the $[Mg]_{total}$ for an initial 0.66 g L-1 endospore suspension (Fig. 4.2). The largest sample dilution corresponding to the highest $[Mg]_{total}$ (see section 2.2) results in a 1.5 % decrease in endospore concentration to 0.65 g L^{-1}. It is unlikely that a 1.5 % decrease in endospore concentration will exert a measurable effect on the adsorption behavior in the system. The 7-10 % relative error associated with ICP-OES data in conjunction with small errors incurred from sample dilution prior to chemical analysis, however, results in larger errors with increasing $[Mg]_{total}$. The relative decrease in percent Mg adsorbed at high $[Mg]_{total}$ further complicates the analysis and likely contributes to the scatter observed above 200 μM $[Mg]_{total}$. Despite these errors, Mg adsorption in this system is measurable and registers at approximately

one order of magnitude less than the $[Mg]_{total}$. Adsorption increases steadily between 20 to 60 μM $[Mg]_{total}$ prior to reaching a plateau above approximately 60 μM $[Mg]_{total}$ (Fig. 4.2).

4.4.2.3 Non-electrostatic surface complexation modeling

Electrostatic and covalent bonding forces between aqueous metal species and reactive sites associated with the cell envelope drive microbe-metal surface complexation. It is therefore necessary to consider the speciation of both the adsorbent and adsorbate when investigating and modeling adsorption phenomena. Non-electrostatic surface complexation models (NE-SCMs) describing the speciation of organic acids bound to the B. subtilis endospore surface (Table 4.1) include both a 4–and 5–site model (Chapter 3, Harrold and Gorman-Lewis, 2013). These models define discrete surface sites thermodynamically consistent with, but not limited to, carboxyl and phosphate functional groups that form anionic oxygen ligands upon deprotonation. Sequential site deprotonation occurs with increasing pH (Fig. 4.1A) resulting in a concomitant increase in and formation of a negatively charged surface electric field (Douglas, 1957). The organic acid moieties on endospore surfaces are capable of adsorbing a variety of metals over a wide pH range (Gorman-Lewis et al., 2013; He and Tebo, 1998; Revis et al., 1997).

The aqueous speciation of an adsorbate can significantly affect adsorption behavior due to species charge and steric effects arising from the size and configuration of aqueous elemental and molecular species. Mg^{2+} dominates aqueous Mg speciation in an open atmosphere system at pH < 9.5 (Fig. 4.1A). Around pH 9, neutrally charged $MgCO_3$ becomes a stable species that dominates aqueous Mg speciation above pH 9.5. $MgHCO_3^+$ remains a minor species at all pH with a small contribution to the total aqueous Mg between pH 9 and 10 (Melchior and Bassett, 1990). Mg-hydroxide formation (Table 4.1, reaction 14 and 15) is negligible at all pH studied (species are excluded from Fig. 4.1A for clarity) but are included in the models for completeness (Baes and Mesmer, 1976; Melchior and Bassett, 1990). No Mg precipitates are predicted.

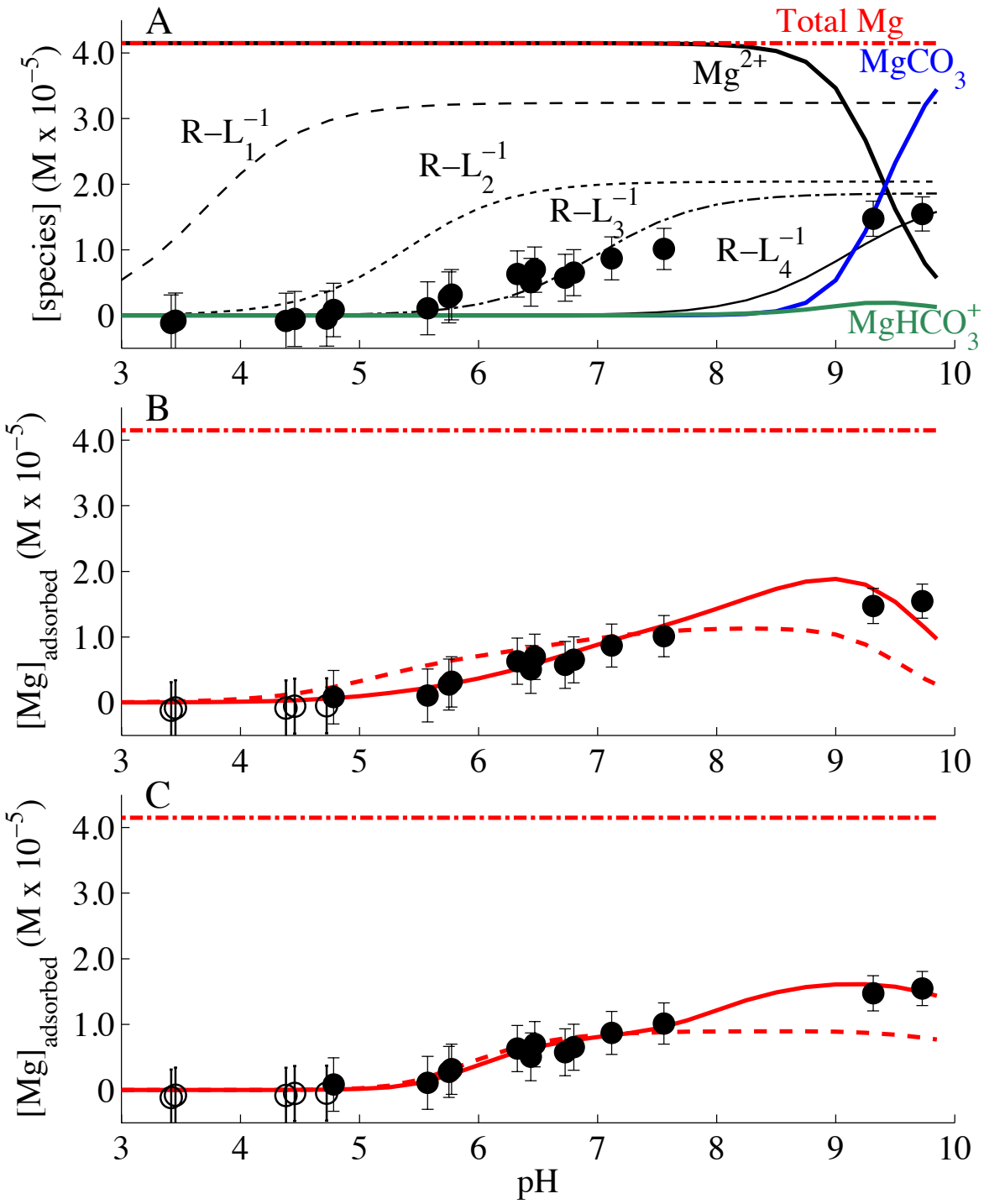

Figure 4.1. Mg-endospore adsorption as a function of solution pH (black data points in A-C, error bars are 2σ) for a 0.3 g L^{-1} endospore suspension in 25 mM NaClO4. (A) pH dependent Mg speciation and deprotonation of endospore surface-sites according to the 4-site NE-SCM by Harrold and Gorman-Lewis (2013). Protonated surface site speciation is excluded for clarity. (B) 2-site (dashed red line) and 3-site (solid red line) NE-SCM for 1_{site}:1_{Mg} Mg adsorption stoichiometry. (C) 2-site (dashed red line) and 3-site (solid red line) NE-SCM for 2_{site}:1_{Mg} Mg adsorption stoichiometry. $[Mg]_{total}$ is plotted for reference in all panels (dash-dot red line, A-C).

Table 4.1 NE-SCM model input and output parameters

Reaction		log K (2σ)
	***B. subtilis* endospore protonation**	
1[a]	$R-L_1^- + H^+ \rightarrow R-L_1H$	3.7 ± 0.2
2[a]	$R-L_2^- + H^+ \rightarrow R-L_2H$	5.4 ± 0.4
3[a]	$R-L_3^- + H^+ \rightarrow R-L_3H$	7.0 ± 0.4
4[a]	$R-L_4^- + H^+ \rightarrow R-L_4H$	9.1 ± 0.6
	1_{site} : 1_{Mg} Mg- endospore pH edge	
5	$R-L_2^- + Mg^{2+} \rightarrow R-L_2Mg^+$	3.52 ± 0.08
6	$R-L_3^- + Mg^{2+} \rightarrow R-L_3Mg^+$	4.47 ± 0.15
7	$R-L_4^- + Mg^{2+} \rightarrow R-L_4Mg^+$	5.24 ± 0.35
	2_{site} : 1_{Mg} Mg- endospore pH edge	
8	$R-2L_2^- + Mg^{2+} \rightarrow R-2L_2Mg$	7.31 ± 0.20
9	$R-2L_3^- + Mg^{2+} \rightarrow R-2L_3Mg$	10.95 ± 0.57
10	$R-2L_4^- + Mg^{2+} \rightarrow R-2L_4Mg$	11.24 ± 0.35
	Mg speciation parameters	
11	Mg^{2+}	n.a.
12[b]	$Mg^{2+} + CO_3^{2-} \rightarrow MgCO_3$	2.97
13[b]	$Mg^{2+} + HCO_3^- \rightarrow MgHCO_3^+$	1.07
14[c]	$4Mg^{2+} + 4OH^- \rightarrow Mg_4(OH)_4^{4+}$	-39.71
15[b]	$Mg^{2+} + 4OH^- \rightarrow Mg\ (OH)^+$	-11.44

[a]Harrold and Gorman-Lewis, 2013 [b] Melchior, 1990 [c] Baes and Mesmer, 1976

We model pH dependent, Mg-endospore adsorption using the 4-site NE-SCM (Table 4.1, reactions 1-4) determined for *B. subtilis* endospores suspended in 0.1 M NaClO4 (Chapter 3, Harrold and Gorman-Lewis, 2013). Work by Borrok and Fein (2005) and Fein et al. (2005) demonstrate that variations in ionic strength from 0.001 to 0.6 M and the accompanying changes to the surface electric field only exert moderate effects on the protonation behavior of gram-negative bacteria that can be described using a single NE-SCM. Based on these findings it is appropriate to apply the 4-site NE-SCM describing *B. subtilis* endospore protonation in a 0.1 M electrolyte to the 25 mM electrolyte suspensions described herein.

Organic acid moieties on the *B. subtilis* endospore surface, and described by the NE-SCM, sequentially deprotonate with increasing pH to form stable anionic oxygen ligands over the entire pH range studied (Fig. 4.1A). Mg-endospore adsorption between pH 4.7 and 9 is

likely driven by electrostatic attraction between the negatively charged endospore surface sites and Mg^{2+}. Using FITEQL, we model pH dependent Mg-endospore adsorption according to a 4-site NE-SCM which assumes discrete 1_{site}:1_{Mg} and 2_{site}:1_{Mg} complexation reactions with deprotonated surface sites. A generic reaction (Eq. 4.1) and the corresponding mass action equation (Eq. 4.2) can be described as:

Eq. 4.1 $$R - nL_i^- + M^m \rightarrow R - nL_iM^{(m-1)}$$

Eq. 4.2 $$K = \frac{[R-nL_iM^{(m-1)}]}{\alpha_{M^m}[R-nL_i^-]}$$

where R-L_i is a functional group, site L_i, on the endospore surface with stoichiometry of n set at 1 or 2 and M is a metal species with charge m, and α_{M^m} is the activity of species M^m. It is possible that Mg adsorption above pH 9 includes the adsorption of neutrally charged $MgCO_3$ onto the endospore surface. Data provided herein is insufficient to determine whether this reaction occurs and is therefore not included in the NE-SCM models describing Mg-endospore adsorption.

Negligible adsorption occurs between pH 3.4 to 4.7. We therefore exclude data below pH 4.7 from our NE-SCMs. Early work by De Jong (1949) shows phosphate moieties have a higher affinity for Mg^{2+} than carboxyl groups. These findings are in accordance with minimal adsorption onto site L_1 (logK= 3.7), which is most chemically consistent with carboxyl moieties. Sites L_2 and L_3 are more thermodynamically consistent with phosphate functional groups (Harrold and Gorman-Lewis, 2013). Attempts to model the entire pH range with a two-site model using sites L_2 and L_3 for both 1_{site}:1_{Mg} and 2_{site}:1_{Mg} stoichiometry fail to describe adsorption above pH 7.8 (dashed line in Fig. 4.1B and 4.1C). Three-site 1_{site}:1_{Mg} and 2_{site}:1_{Mg} stoichiometry according to reactions 5-7 and 8-10 (Table 4.1, Fig. 4.1B and 4.1C), respectively, provide the best

fit to the data with the fewest degrees of freedom. We generated each 3-site, best-fit model by first optimizing log K values describing Mg^{2+} adsorption onto sites L_2 and L_3 (Table 4.1, reactions 5-6 and 8-9) over the pH range 4.7 to 7.7. Log Ks describing adsorption onto sites L_2 and L_3 were set as constants and the remainder of the data (pH 4.7 to 9.7) was subsequently modeled by optimizing adsorption onto site L_4 (Table 4.1, reactions 7 and 10).

Data describing adsorption at variable Mg:endospore ratios was evaluated at pH 7.3 ± 0.3 (2σ). Adsorption data at one pH value is insufficient to constrain the log K values and adsorption behavior of discrete sites since reactions involving other sites at higher and lower pH cannot be constrained. We instead apply the pH-edge derived, 3-site NE-SCMs to the variable Mg:endospore ratio data to assess the validity and predictability of $1_{site}:1_{Mg}$ and $2_{site}:1_{Mg}$ adsorption stoichiometry (Fig. 4.2). This is achieved by predicting $[Mg]_{adsorbed}$ for each data point based on serial data inputs corresponding to the experimental sample pH and dilution corrected endospore-site concentrations and $[Mg]_{total}$.

The 3-site NE-SCM describing $1_{site}:1_{Mg}$ adsorption stoichiometry provides a good fit to the adsorption data below approximately 50 μM $[Mg]_{total}$. Above this threshold, the $1_{site}:1_{Mg}$ adsorption model over-estimates Mg adsorption and fails to predict the observed adsorption plateau at $[Mg]_{total}$ above approximately 60 μM. Inversely, the $2_{site}:1_{Mg}$ NE-SCM over-predicts Mg adsorption below 50 μM $[Mg]_{total}$ while successfully describing the adsorption plateau above ~ 60 μM $[Mg]_{total}$. These model results may suggest (*i*) a shift in adsorption stoichiometry with increasing Mg:endospore ratio, (*ii*) a mixture of both $1_{site}:1_{Mg}$ and $2_{site}:1_{Mg}$ adsorption stoichiometry over the entire range of Mg:endospore ratios studied or (*iii*) a combination of these two phenomena.

Evidence exists for both $1_{site}:1_{Mg}$ and $2_{site}:1_{Mg}$ adsorption stoichiometry with bacterial cell walls (Lambert et al., 1975a; Lambert et al., 1975b; Marquis et al., 1976; Ou et al., 1973). Baddley et al. (1973) describe two ionic bonding energies associated with the availability of phosphate groups in gram-positive cell walls containing teichoic acids. These bonding energies

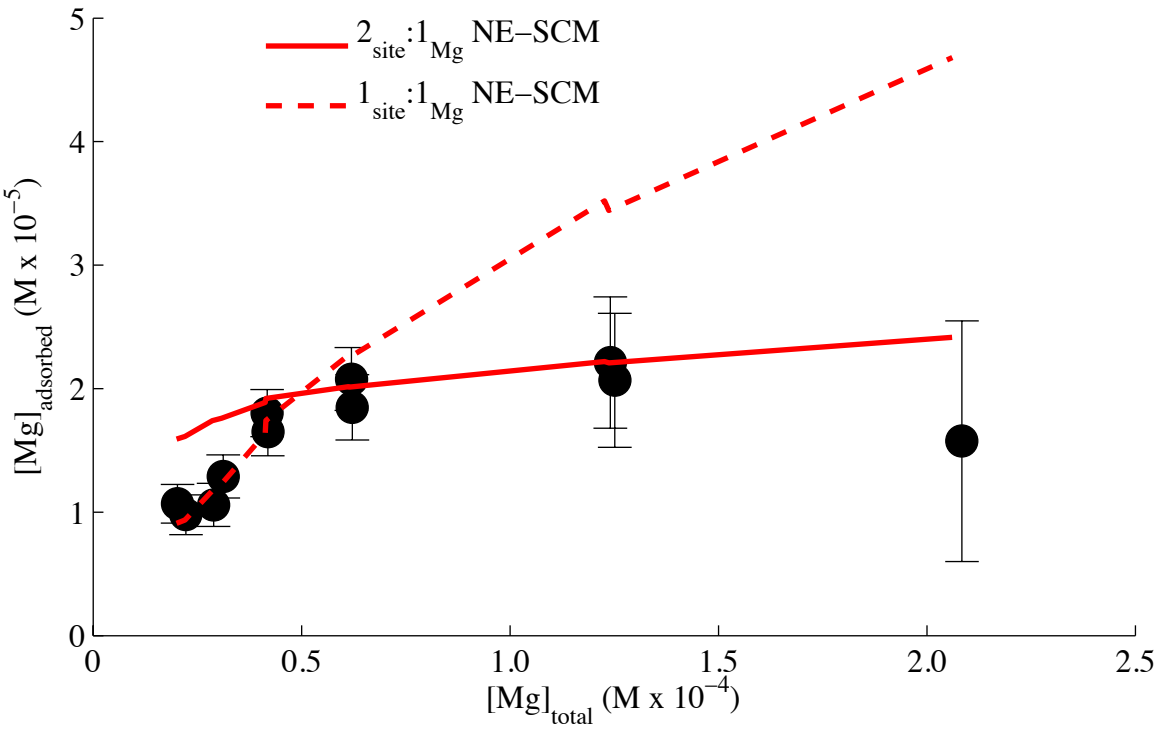

Figure 4.2 Mg-*B.subtilis* endospore adsorption as a function of Mg:endospore ratio at pH 7.3 ± 0.3 (2σ) (black data points, 1σ error bars). $[Mg]_{total}$ is increased for a constant endospore concentration of 0.66 g L^{-1} in 25 mM $NaClO_4$. Dashed and solid red lines plot predicted model values for each data point based on 3-site, 1_{site}:1_{Mg} and 2_{site}:1_{Mg} stoichiometric NE-SCMs describing pH dependent, Mg-endospore adsorption data.

are believed to reflect $2_{phosphate}$:1_{Mg} stoichiometry, where two neighboring phosphate moieties bond with a single Mg^{2+}, and $1_{phosphate}$:$1_{Mg\text{-}Cl}$ complexation when neighboring phosphate groups were neutralized by an amine moiety (Baddiley et al., 1973). Others effects on Mg adsorption include changes in cell wall conformation and ionic strength (Marquis et al., 1976). *B. subtilis* endospore coats are comprised of a complex network of over 30 proteins (Driks, 2002). It is possible that some regions on the endospore coat host neighboring organic acid moieties or diprotic functional groups, such as phosphate groups, that allow 2_{site}:1_{Mg} adsorption stoichiometry, while other locales only support 1:1 complex formation.

4.4.3 Si – endospore adsorption

We measured Si–endospore adsorption as a function of pH and Si:endospore ratio. Negligible adsorption occurred between pH 3 and 7.5 for a 1.2 g L^{-1} endospore suspension with a total silica concentration ($[Si]_{total}$) of 35.9 μM (Fig. 4.3). Similarly, increasing $[Si]_{total}$ from approximately 16 to 700 μM $[Si]_{total}$ for a 0.66 g L^{-1} endospore suspension at pH 7.5 ± 0.4 (2σ) yielded little to no measurable adsorption (Fig. 4.4). Positive adsorption values in both assay types are within the relative error observed for the ICP-OES analyses (7-10 %).

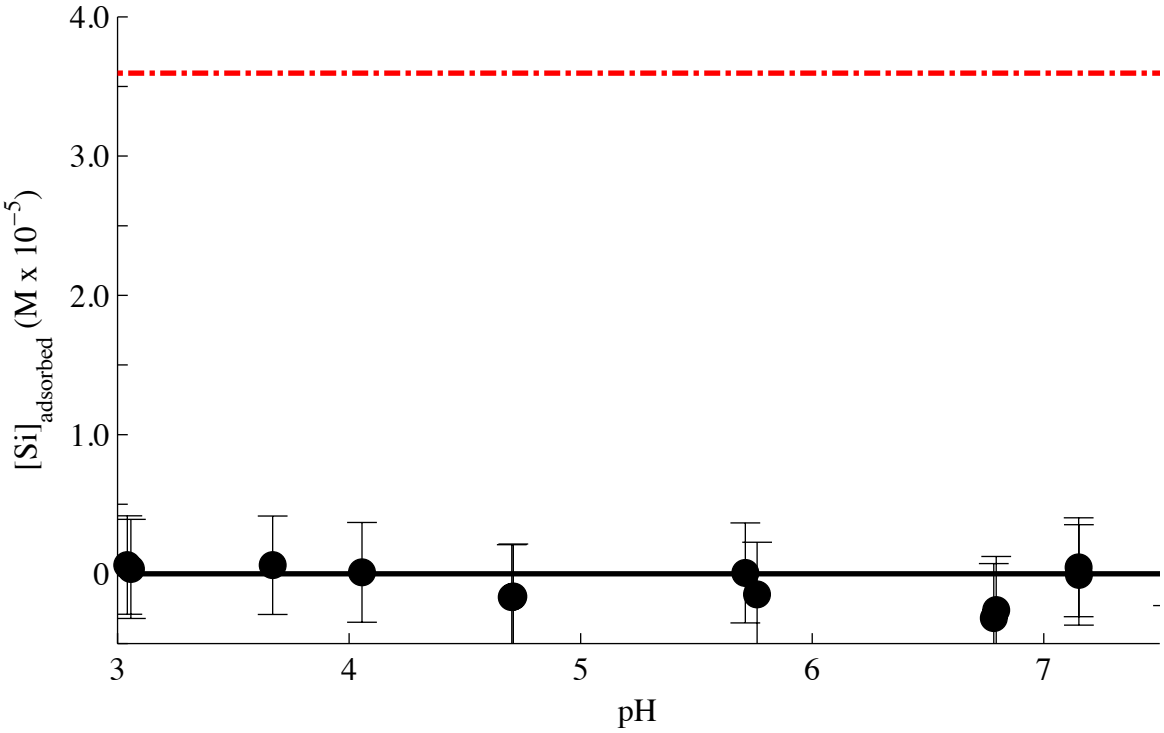

Figure 4.3 Si-endospore adsorption as a function of solution pH (black data points) for duplicate 1.2 g L^{-1} B subtilis endospore suspensions with 35.9 μM $[Si]_{total}$ (dashed red line). $[Si]_{total}$ is below SiO_2 saturation. Error bars are 1σ.

At pH between 3 to 7.5 Si exists as neutrally charged silicic acid ($Si(OH)_4$). Quartz (SiO_2,(cr)) saturation occurs around 1.1 x 10^{-4} M $[Si(OH)_4]_{total}$ at pH 7.5. A substantial kinetic barrier, however, likely prevents SiO_2,(cr) crystallization in our assays. It is possible that

aqueous silicic acid polymers or a silica gel formed within the variable Si:endospore assays containing $[Si]_{total}$ in excess of the SiO_2 (cr) saturation limit. Since loss of Si in all Si-adsorption assays is negligible, any Si polymers that formed did not adsorb to the endospore surface.

$Si(OH)_4$ adsorbs to neutrally charged iron-(hydr)oxide surfaces at circumneutral pH (Fein et al., 2002) by inner-sphere, bidentate bonding at low $[Si]_{total}$ (Hiemstra et al., 2007). Si–iron-oxide adsorption at high, or supersaturated, silica concentrations includes the formation of adsorbed silica polymers which deprotonate more easily than monomeric silicic acid to produce an anionic oxygen ligand at circumneutral pH (Hiemstra et al., 2007). Silica-organic acid complexes formed by multi-functional, carboxylic acids at circumneutral pH, are associated with enhanced quartz dissolution (Bennett, 1991; Bennett et al., 1988).

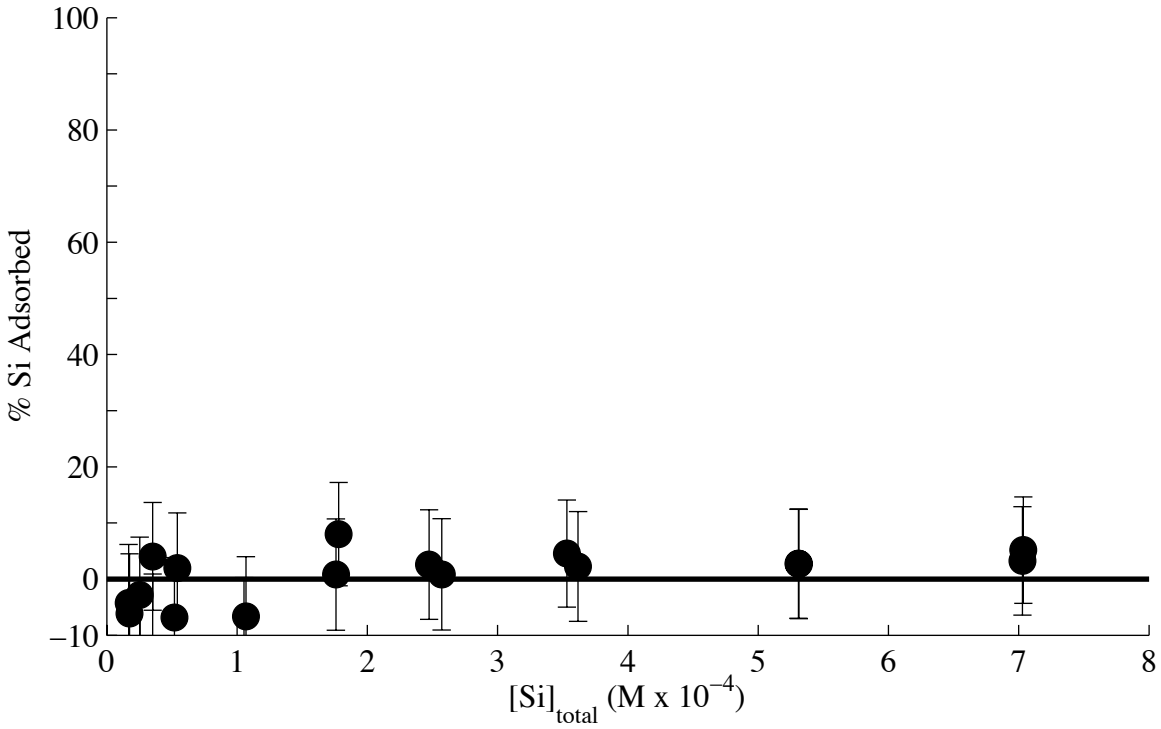

Figure 4.4. Percent silica adsorbed as a function of Si:endospore ratio at pH 7.5 ± 0.4 (2σ). The $[Si]_{total}$ is increased relative to the initial endospore suspensions of 0.66 g L^{-1}. Adsorption is negligible at all $[Si]_{total}$. $SiO_{2,}$(cr) saturation occurs at approximately 1.1 x 10^{-4} M $[Si(OH)4]_{total}$ for pH 7.5. Error bars are 1σ.

The data described herein, however, provide no evidence for silica-endospore adsorption driven by hydrophobic interactions or organic acid complexation. The incompatibility of Si-endospore adsorption is likely due to a variety of factors that may include the dichotic chemical nature of the endospore coat. Endospore coats are more hydrophobic than their vegetative cell counterpart as evidenced from the partitioning of endospores into the organic phase of an aqueous two-phase system consisting of polyethylene glycol and a strong phosphate buffer (Chapter 2, Harrold et al., 2011; Sacks and Alderton, 1961). Despite their relative hydrophobicity, *B. subtilis* endospore surfaces also host an array of proton-active organic acid moieties at concentrations on par with site densities measured for vegetative cells (Chapter 3, Harrold and Gorman-Lewis, 2013). Sufficient electrostatic repulsion generated by deprotonated, anionic organic acid functional groups may inhibit the formation of Si-endospore surface complexes. Bacterial envelopes are complex three-dimensional structures relative to more planar mineral surfaces. Organic acid moieties on the endospore "surface" may in-fact be imbedded within a complex protein structure that is inaccessible to monomeric and polymeric silicic acid due to steric limitations. Our results for *B. subtilis* Si-endospore adsorption agree with Fein et al. (2002) who observed negligible *B. subtilis* Si-cell adsorption under similar chemical conditions.

4.4.4 Multi-element endospore adsorption

Adsorption in aqueous multi-component systems does not necessarily reflect the element-adsorption behavior observed in single element assays. Factors effecting adsorption in multi-element systems include, but are not limited to: (*i*) alterations in element speciation due to the formation of multi-element species that have a different affinity for the adsorbent (e.g. Gorman-Lewis et al., 2005); (*ii*) the formation of ternary complexes on the adsorbent surface (e.g. Alessi and Fein, 2010); (*iii*) the precipitation of mineral phases onto the adsorbent surface which alter its surface properties (e.g. Fein et al., 2002); and (*iv*) the precipitation of mineral

phases in solution that alter solution equilibrium. We measured the effect of varying Si:Mg ratios on Si and Mg adsorption at circumneutral pH.

Si adsorption as a function of increasing Mg:Si ratio was measured by increasing $[Mg]_{total}$ relative to a constant 107 μM $[Si]_{total}$ in a 0.66 g L^{-1} endospore suspension. Average sample pH was 7.2 ± 0.7 (2σ). Mg adsorption increases with increasing $[Mg]_{total}$ up to approximately 50 μM corresponding to an adsorption maximum around 15 μM (Fig. 4.5A). This adsorption behavior is similar to adsorption observed in the variable Mg-endospore ratio assays without Si (Fig. 4.2). Si adsorption in this system is negligible at all Mg concentrations.

Similar assays were conducted to determine Mg adsorption behavior as a function of increasing Si:Mg ratio at pH 7.1 ± 0.4 (2σ). Data show a moderate increase in Mg adsorption from approximately 20 to 50 μM corresponding with an increase in $[Si]_{total}$ from 0 to 1.75 mM (Fig. 4.6 C). A multivariate analysis of variance (ANOVA) test confirms that Mg adsorption at the two highest $[Si]_{total}$ is statistically ($p < 0.05$) greater than at the lowest $[Si]_{total}$. To confirm the increase in Mg adsorption is independent of variations in sample pH we plot adsorption against equilibrium pH (Fig. 4.7). No clear correlation is observed with sample pH reinforcing that an increase in $[Si]_{total}$ enhances Mg adsorption in this system.

To better understand the effects of increasing Si:Mg ratio on the chemical system we modeled the predicted speciation for the adsorption assays based on $[Si]_{total}$ and $[Mg]_{total}$ (Fig. 4.6A). SiO_2 (cr) saturation occurs above 110 μM $[Si]_{total}$ but is unlikely to precipitate due to a kinetic barrier. We therefore exclude SiO_2 (cr) as a potential precipitate from the speciation model to better assess the chemical conditions affecting endospore adsorption. Based on the observed increase in Mg adsorption (~30 μM) we only consider species with a concentration above $10^{-6.5}$ M (~0.3 μM) as having the capacity to substantially influence Mg-endospore adsorption (Fig. 4.6A).

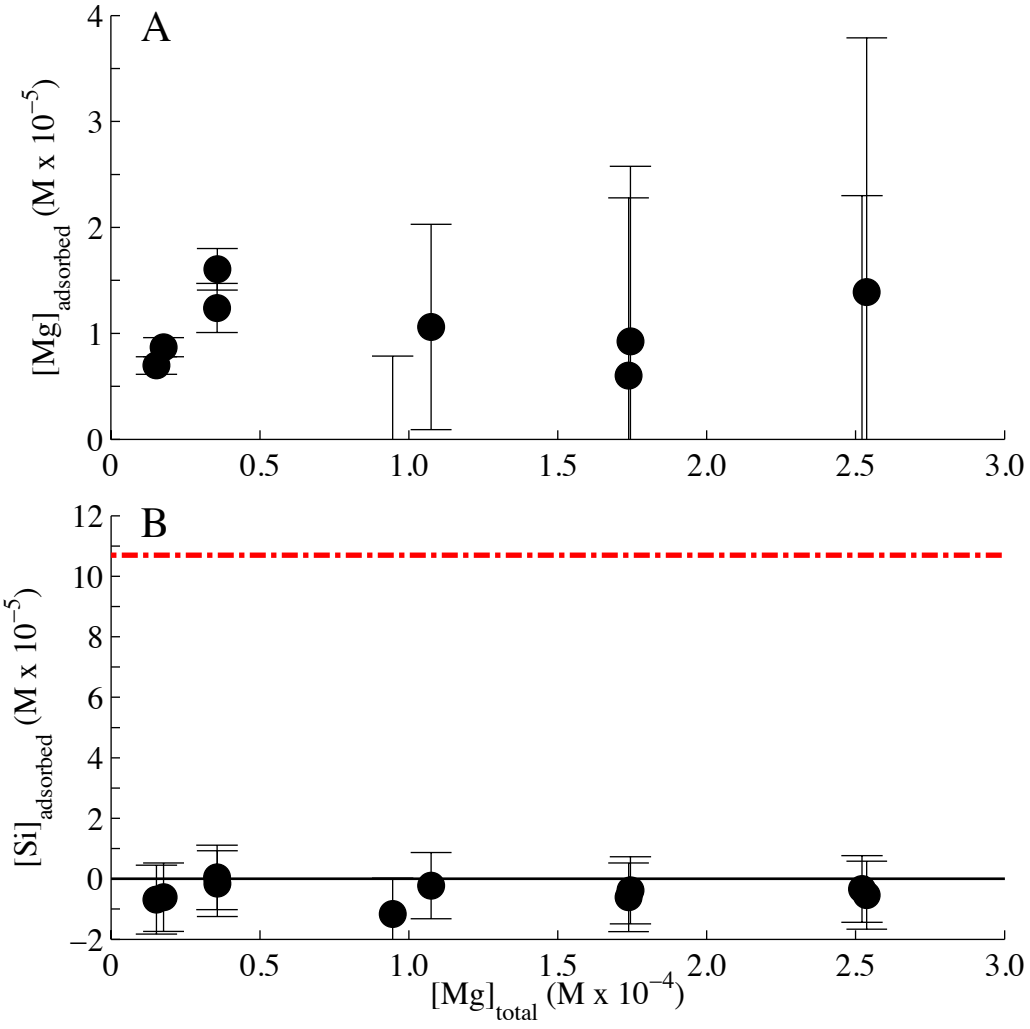

Figure 4.5. Mg (A, black data points) and Si (B, black data points) adsorption as a function of increasing $[Mg]_{total}$ for an initial 0.66 g L-1 endospore suspension with 107 μM $[Si]_{total}$ (B, dashed red line). Average pH is 7.2 ± 0.7 (2σ). Error bars are 1σ.

A hydrated sodium silicate mineral, magadiite ($NaSi_7O_{13}(OH)_3 \bullet 3\ H2O$), is purported to precipitate under the ionic strength and highest $[Si]_{total}$ tested in our assay. It is also possible that silica polymerization occurs to varying degrees under these conditions though precipitation of SiO_2 (am) is not predicted in the speciation. It is conceivable that Mg adsorption onto amorphous or crystalline silicate precipitates could account for the increase in Mg adsorption with increasing $[Si]_{total}$. However, $[Si]_{adsorbed}$ as a function of increasing $[Si]_{total}$ exhibits little to no Si removal from solution (Fig. 4.6B). A large component of the observed linear "increase" in Si loss as a function of increasing $[Si]_{total}$ (Fig. 4.6B) is likely due to the high (7-10 %) relative error observed for the ICP-OES Si analysis. Potentially significant Si loss observed at the highest $[Si]_{total}$ may be linked to endospore adsorption, ternary adsorption complex formation or precipitation. Removal of Si via precipitation would require the formation of particulates ≥ 0.22 μm (filtration size cutoff). This is unlikely, however, based on the complexity of the predicted silicate precipitate, magadiite, and the relatively short, 2 h equilibration times.

Anionic, mono-deprotonated silicic acid ($SiO(OH)_3^-$) gradually increases with increasing $[Si]_{total}$ until it reaches a maximum concentration around 3 μM. Neutral and anionic silica species could form ternary adsorption complexes with adsorbed Mg^{2+}, particularly if $1_{site}{:}1_{Mg}$ complexes with a net positive charge exist on the endospore surface. Subsequent Mg adsorption onto this Mg-Si complex could account for the increase in Mg adsorption with increasing $[Si]_{total}$. The gradual increase in Mg adsorption with increasing $[Si]_{total}$ supports this hypothesis. Assuming a *R-L$_i$Mg-Si-Mg* ternary complex is formed, the minimum concomitant, stoichiometric increase in Si- endospore adsorption would equal 30 μM $[Si]_{adsorbed}$ or 2 % adsorption at the highest $[Si]_{total}$. This increase in adsorption is well within the analytical error and would therefore be undetectable in our data. Based on these considerations we predict that ternary Mg-Si complex formation is the most likely cause for increased Mg adsorption with increasing $[Si]_{total}$. Additional experimental methods are required to confirm the formation of ternary Mg-Si-Mg adsorption complexes.

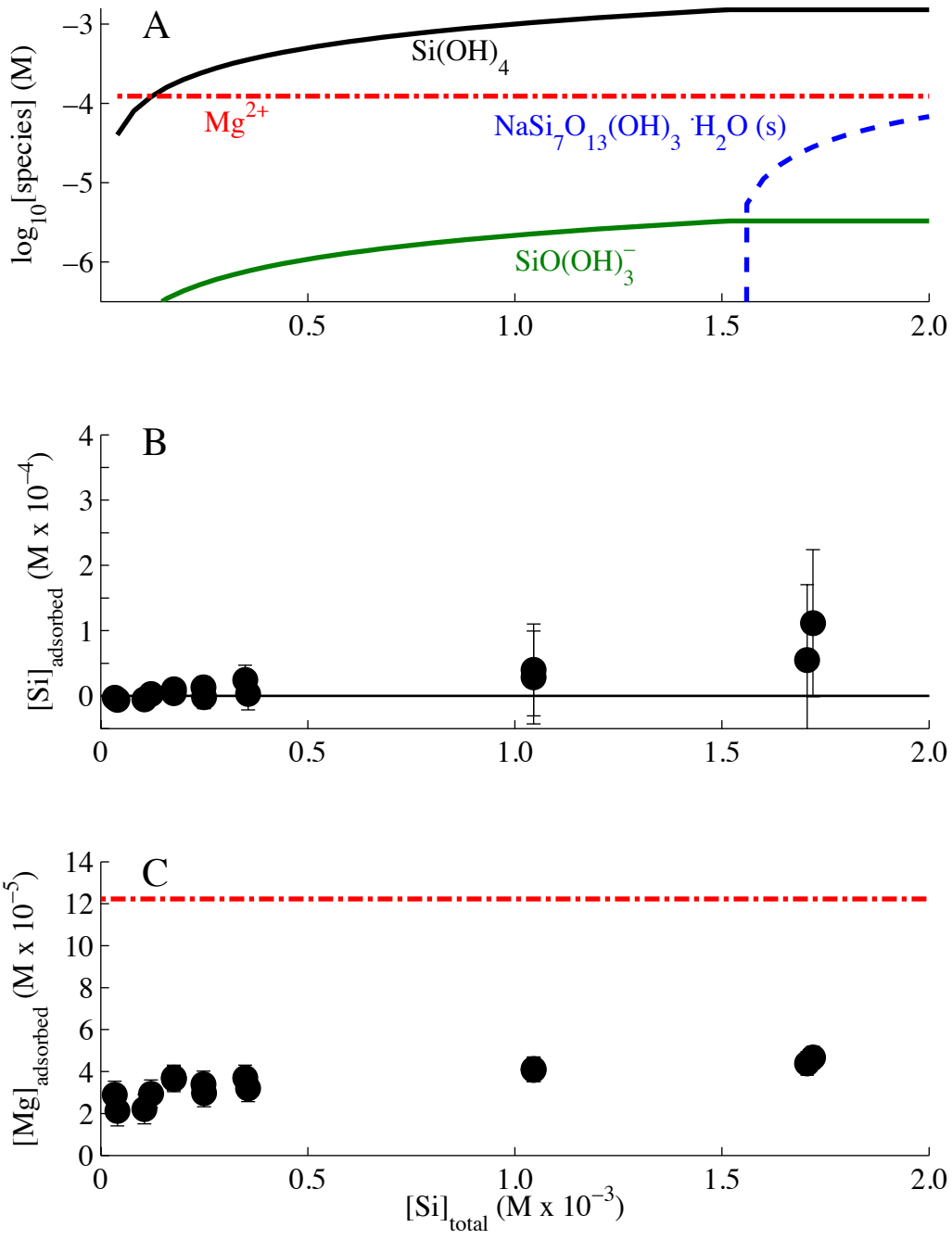

Figure 4.6 (A) Si and Mg speciation for an assay with variable $[Si]_{total}$ and constant, 123 μM [Mg] at pH 7.1 and assuming SiO_2 (cr) does not precipitate due to a kinetic barrier. Si (B, black data points) and Mg (C, black data points) adsorption as a function of increasing $[Si]_{total}$ for an initial 0.66 g L-1 endospore suspension with 123 μM $[Mg]_{total}$ (B, dashed red line). Average equilibrium pH for data plotted in (B) and (C) is 7.1 ± 0.4 (2σ). Error bars are 1σ.

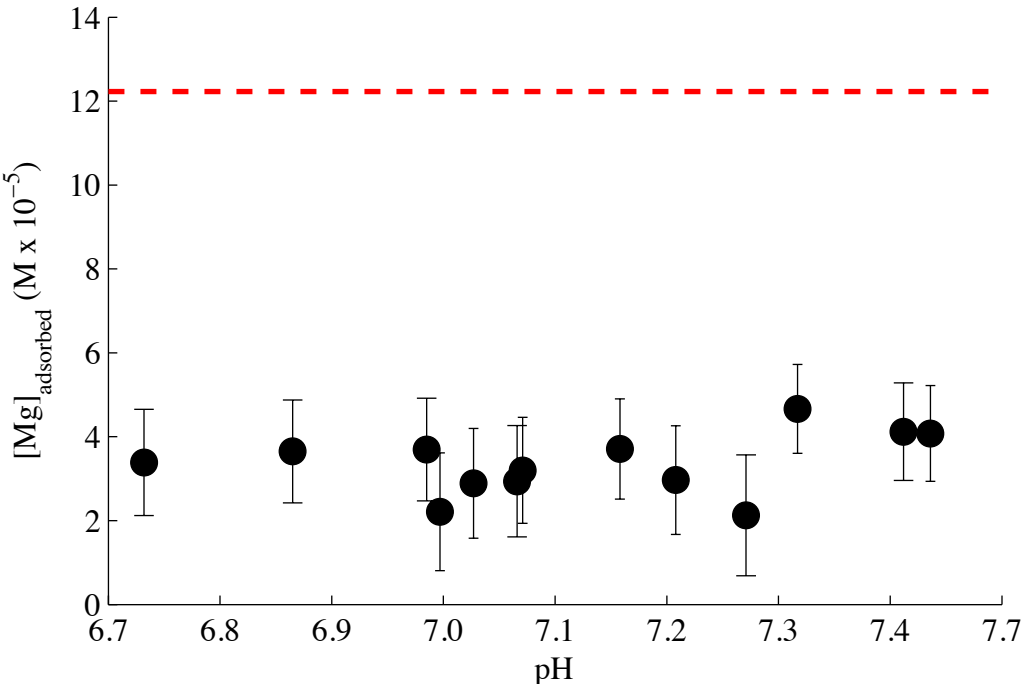

Figure 4.7 Mg adsorption (black data points) as a function of pH in assays with increasing $[Si]_{total}$ for an initial 0.66 g L-1 endospore suspension with 123 μM $[Mg]_{total}$ (dashed red line). Average pH is 7.1 ± 0.4 (2σ). Data is equivalent to Fig. 4.6B. Error bars are 1σ.

4.5 Conclusions

Mg-endospore adsorption increases with increasing pH and can be modeled using a 4-site NE-SCM with $1_{site}:1_{Mg}$ and $2_{site}:1_{Mg}$ adsorption stoichiometry onto sites L_2, L_3 and L_4. Data and NE-SEMs suggest Mg-phosphate complexation is more favorable relative to adsorption with carboxyl surface sites (L_1). $2_{site}:1_{Mg}$ adsorption stoichiometry may occur with a single, diprotic phosphate moiety or neighboring organic acid moieties. These findings are in agreement with numerous sources describing the formation of Mg-phosphate complexes with $1_{site}:1_{Mg}$ and $2_{site}:1_{Mg}$ stoichiometry (Baddiley et al., 1973; Lambert et al., 1975a; Lambert et al., 1975b; Marquis et al., 1976; Walters and Van Os, 1971). Increasing adsorption as a function of increasing $[Mg]_{total}$ for a constant endospore concentration at pH 7.3 can be described by $1_{site}:1_{Mg}$ adsorption stoichiometry. The adsorption plateau, however, is best described by a $2_{site}:1_{Mg}$

stoichiometry, further suggesting the formation of both adsorption complexes on the endospore surface. Based on these findings, the *B. subtilis* endospore surface, like their vegetative cell counterpart, can influence chemical equilibrium in microbe-water-rock systems by directly adsorbing aqueous Mg^{2+}.

Si adsorption is negligible in all endospore adsorption assays including those systems containing both Si and Mg. These findings are in agreement with Fein et al. (2002) and Konhauser et al. (Konhauser et al., 1993; Konhauser et al., 1994). Mg adsorption increases slightly with increasing $[Si]_{total}$. The increased adsorption may occur due to the formation of ternary *R-L$_i$Mg-Si-Mg* adsorption complexes. The estimated magnitude of concomitant Si adsorption in the case of ternary complex formation is within analytical error. More work is required to determine the cause of increased Mg adsorption in the presence of Si.

4.6 References

Alessi, D.S., Fein, J.B., 2010. Cadmium adsorption to mixtures of soil components: Testing the component additivity approach. Chemical Geology 270, 186-195.

Baddiley, J., Hancock, I.C., Sherwood, P., 1973. X-ray Photoelectron Studies of Magnesium Ions bound to the Cell Walls of Gram-positive Bacteria. Nature 243, 43-45.

Baes, C.F., Mesmer, R.E., 1976. The hydrolysis of cations. Wiley, New York.

Bennett, P.C., 1991. Quartz dissolution in organic-rich aqueous systems. Geochimica et Cosmochimica Acta 55, 1781-1797.

Bennett, P.C., Melcer, M.E., Siegel, D.I., Hassett, J.P., 1988. The dissolution of quartz in dilute aqueous solutions of organic acids at 25°C. Geochimica et Cosmochimica Acta 52, 1521-1530.

Borrok, D.M., Fein, J.B., 2005. The impact of ionic strength on the adsorption of protons, Pb, Cd, and Sr onto the surfaces of Gram negative bacteria: testing non-electrostatic, diffuse, and triple-layer models. Journal of Colloid and Interface Science 286, 110-126.

Daughney, C.J., Fein, J.B., 1998. The effect of ionic strength on the adsorption of H+, Cd2+, Pb2+, and Cu2+ by Bacillus subtilis and Bacillus licheniformis: A surface complexation model. Journal of Colloid and Interface Science 198, 53-77.

Douglas, H.W., 1957. Electrophoretic studies on spores and vegitative cells of certain strains of B. *megaterium*, B. *subtilis*, and B. *cereus*. Journal of applied Bacteriology 20, 390-403.

Driks, A., 2002. Maximum shields: the assembly and function of the bacterial spore coat. Trends in Microbiology 10, 251-254.

Fein, J.B., Boily, J.-F., Yee, N., Gorman-Lewis, D., Turner, B.F., 2005. Potentiometric titrations of Bacillus subtilis cells to low pH and a comparison of modeling approaches. Geochimica et Cosmochimica Acta 69, 1123-1132.

Fein, J.B., Scott, S., Rivera, N., 2002. The effect of Fe on Si adsorption by Bacillus subtilis cell walls: insights into non-metabolic bacterial precipitation of silicate minerals. Chemical Geology 182, 265-273.

Gorman-Lewis, D., Elias, P.E., Fein, J.B., 2005. Adsorption of Aqueous Uranyl Complexes onto Bacillus subtilis Cells. Environmental Science & Technology 39, 4906-4912.

Gorman-Lewis, D., Jensen, M.P., Harrold, Z.R., Hertel, M.R., 2013. Complexation of neptunium(V) with Bacillus subtilis endospore surfaces and their exudates. Chemical Geology 341, 75-83.

Harrold, Z.R., Gorman-Lewis, D., 2013. Thermodynamic analysis of Bacillus subtilis endospore protonation using isothermal titration calorimetry. Geochimica et Cosmochimica Acta 109, 296-305.

Harrold, Z.R., Hertel, M.R., Gorman-Lewis, D., 2011. Optimizing Bacillus subtilis spore isolation and quantifying spore harvest purity. Journal of Microbiological Methods 87, 325-329.

He, L.M., Tebo, B.M., 1998. Surface charge properties of and Cu(II) adsorption by spores of the marine Bacillus sp. strain SG-1. Applied and Environmental Microbiology 64, 1123-1129.

Hiemstra, T., Barnett, M.O., van Riemsdijk, W.H., 2007. Interaction of silicic acid with goethite. Journal of Colloid and Interface Science 310, 8-17.

Konhauser, K.O., Fyfe, W.S., Ferris, F.G., Beveridge, T.J., 1993. Metal sorption and mineral precipitation by bacteria in two Amazonian river systems: Rio Solimoes and Rio Negro, Brazil. Geology 21, 1103-1106.

Konhauser, K.O., Schultze-Lam, S., Ferris, F.G., Fyfe, W.S., Longstaffe, F.J., Beveridge, T.J., 1994. Mineral precipitation by epilithic biofilms in the speed river, ontario, Canada. Appl Environ Microbiol 60, 549-553.

Konhauser, K.O., Urrutia, M.M., 1999. Bacterial clay authigenesis: a common biogeochemical process. Chemical Geology 161, 399-413.

Kruyt, H.R., 1949. Colloid science. Elsevier Pub. Co., New York.

Lambert, P.A., Hancock, I.C., Baddiley, J., 1975a. Influence of alanyl ester residues on the binding of magnesium ions to teichoic acids. Biochem. J. 151, 671-676.

Lambert, P.A., Hancock, I.C., Baddiley, J., 1975b. The interaction of magnesium ions with teichoic acid. Biochem J 149, 519-524.

Marquis, R.E., Mayzel, K., Carstensen, E.L., 1976. Cation exchange in cell walls of gram-positive bacteria. Can. J. Microbiol. Canadian Journal of Microbiology 22, 975-982.

Melchior, D.C., Bassett, R.L., 1990. Chemical modeling of aqueous systems II : developed from a symposium sponsored by the Division of Geochemistry at the 196th National Meeting of the American Chemical Society, Los Angeles, California, September 25-30, 1988. American Chemical Society, Washington, DC.

Olsen, A.A., Rimstidt, D.J., 2008. Oxalate-promoted forsterite dissolution at low pH. Geochimica et Cosmochimica Acta 72, 1758-1766.

Ou, L.-T., Chatterjee, A.N., Young, F.E., Marquis, R.E., 1973. The physiology of teichoic acid deficient staphylococci. Canadian Journal of Microbiology 19, 1393-1399.

Revis, N.W., Hadden, C.T., Edenborn, H., 1997. Removal of dissolved heavy metals and radionuclides by microbial spores, Other Information: PBD: [1997], p. Medium: ED; Size: 14 p.

Sacks, L.E., Alderton, G., 1961. Behavior of bacterial spores in aqueous polymer two-phase systems. Journal of Bacteriology 82, 331-341.

Scott, I.R., Ellar, D.J., 1978. Study of calcium dipicolinate release during bacterial spore germination by using a new, sensitive assay for dipicolinate. Journal of Bacteriology 135, 133-137.

Setlow, B., Loshon, C., Genest, P., Cowan, A., Setlow, C., Setlow, P., 2002. Mechanisms of killing spores of Bacillus subtilis by acid, alkali and ethanol. Journal of Applied Microbiology 92, 362-375.

Setlow, P., 2003. Spore germination. Current Opinion in Microbiology 6, 550-556.

Setlow, P., 2006. Spores of *Bacillus subtilis*: their resistance to and killing by radiation, heat and chemicals. Journal of Applied Microbiology 101, 514-525.

Siala, A., Hill, I.R., Gray, T.R.G., 1974. Populations of Spore-forming Bacteria in an Acid Forest Soil, with Special Reference to Bacillus subtilis. J Gen Microbiol 81, 183-190.

Vandevivere, P., Welch, S.A., Ullman, W.J., Kirchman, D.L., 1994. Enhanced Dissolution of Silicate Minerals by Bacteria at Near-Neutral pH. Microbial Ecology 27, 241-251.

Walters, J., Van Os, G., 1971. Magnesium binding to yeast ribosomes. BIP Biopolymers 10, 11-20.

Warth, A.D., 1983. Determination of dipicolinic acid in bacterial spores by derivative spectroscopy. Analytical Biochemistry 130, 502-505.

Wells, A.F., 1986. Structural inorganic chemistry. Clarendon Press ; Oxford University Press, Oxford [Oxfordshire]; New York.

Yee, N., Fein, J., 2001. Cd adsorption onto bacterial surfaces: A universal adsorption edge? Geochimica et Cosmochimica Acta 65, 2037-2042.

Chapter 5: Microbially enhanced forsterite dissolution through non-metabolic surface reactivity

5.1 Abstract

Silicate weathering rates play a major role in dictating the flux of trace and major elements into the environment that in turn affect many geochemical and biologic cycles. Microbes, an intrinsic component in water-rock systems, are known to increase the rate of silicate dissolution. Mechanisms of biotically enhanced dissolution include the production and release of organic acids associated with metabolic activity. The influence of microbial surface reactivity on silicate mineral dissolution rates remains enigmatic. We utilize *Bacillus subtilis* endospores, a metabolically dormant cell type, as a tool for isolating and quantifying the affects of microbial surfaces on the rate of forsterite dissolution. Forsterite dissolution rates increase due to both indirect and direct pathways associated with endospore-Mg adsorption and mineral adhesion, respectively. Direct, endospore-forsterite adhesion likely increases the dissolution rate by forming bonds with the mineral surface and lowering the activation energy of dissolution. Indirect endospore interactions may enhance forsterite dissolution by altering the chemical gradient between the dissolving mineral front and bulk solution. Both direct and indirect surface reactivity enhanced rates increase as a function of endospore concentration and are modeled according to a simplified rate law:

$$r_{Si,o} = 10^{-11.33} + 10^{-10.19}[endospore]^{0.52} + 10^{-10.38}[endospore]^{0.78}$$

The work described herein provides a model for isolating the effects of microbial surface reactivity on mineral dissolution rates.

5.2 Introduction

Silicate mineral dissolution products, such as calcium (Ca), magnesium (Mg) and iron (Fe), play an important role in numerous biologic and geochemical cycles within the hydro-, bio- and litho-spheres. Ca and Mg released during the chemical weathering of primary silicates have the capacity to sequester atmospheric CO_2 in secondary carbonate precipitates (Berner et al., 1983; Kohler et al. 2010). Silicate dissolution products are also a necessary component in microbial metabolism and plant growth. The flux of silicate dissolution products into the environment is largely controlled by the rate of primary silicate mineral dissolution. Many abiotic factors are know to affect silicate dissolution rates including, but not limited to, surface area exposure, temperature, pressure, solution pH and the presence of organic acids (e.g. Bennett, 1991; Oelkers, 2001; Olsen and Rimstidt, 2008; Pokrovsky and Schott, 2000b; Rosso and Rimstidt, 2000; White and Brantley, 1995).

Microbes are a ubiquitous component in water-rock systems including ground and surface waters, soils (Siala et al., 1974), mid-ocean ridge hydrothermal systems, and deep sedimentary basins (Whitman et al., 1998). Microbe-mineral interactions are known to increase mineral dissolution rates (e.g. Lee and Fein, 2000; Song et al., 2007; Stumm, 1990; Vandevivere et al., 1994) and may play a significant role in determining the overall flux of dissolution products into the environment. Mechanisms of microbially enhanced dissolution include the production of ion-chelators (e.g. siderophores) and inorganic (e.g. H_2CO_3) and organic acids associated with microbial metabolism (Ehrlich, 1996; Pokrovsky et al., 2009; Vandevivere et al., 1994). The effect of microbial surface reactivity on silicate mineral dissolution rates, however, is unknown.

Bacterial cell walls provide a complex and highly reactive organic surface in water-rock systems. Evidence suggests cell surface reactivity arises from the presence of ion adsorption sites characterized by a range of organic acids including carboxyl and phosphate groups (Borrok

et al., 2004; Gorman-Lewis et al., 2006; Chapter 3, Harrold and Gorman-Lewis, 2013). These ion adsorption sites are capable of hosting a myriad of ion complexation reactions (Borrok et al., 2004; Borrok and Fein, 2005; Daughney et al., 2001; Gorman-Lewis et al., 2006; Ngwenya et al., 2009; Phoenix et al., 2003) that may have the capacity to affect mineral dissolution rates through direct mineral contact or indirectly, by complexing dissolution products in solution. The effects of microbial surface adsorption and mineral adhesion on chemical weathering rates may even outweigh the influence of active metabolic processes in environments where cell metabolism is slow or microbial surface area is large.

Isolating the influence of cell wall interactions on mineral dissolution rates is challenging for both *in situ* and laboratory experiments due to ongoing microbial metabolism. To date, two studies have been aimed at measuring the effects of *Bacillus subtilis* cell surface reactivity on gibbsite (Lee and Fein, 2000) and CuO (Wightman and Fein, 2004) dissolution. While increased CuO dissolution rates were attributed to cell wall adsorption, dissolution could only be measured over short (4 d) timeframes (Wightman and Fein, 2004). Complications including vegetative cell lysis affected both studies and limit the duration of experimental assays. The extent to which metabolically independent surface reactions influence ion concentrations, chemical speciation, mineral dissolution rates and precipitation features observed in microbe-mineral systems remains enigmatic (Bennett et al., 2001; Rogers and Bennett, 2004; Vandevivere et al., 1994).

Bacterial endospores provide the ideal biologic tool for isolating the effects of microbial surfaces on silicate mineral dissolution rates. Endospores, a metabolically dormant cell-type produced by some bacteria, function to preserve the bacterium genome when exposed to inhospitable conditions including harsh chemicals, UV radiation and oligotrophic environments. Individual endospores can persist for years in oligotrophic conditions due to their metabolic dormancy. We utilize *B. subtilis* endospores to quantify and model the effects of microbial surface reactivity on the rate of forsterite (Fo_{90}, $Mg_{1.8}Fe_{0.2}SiO_4$) dissolution as a function of both

direct, microbe-mineral adhesion and indirect, adsorption interactions. Results show the endospore surface is capable of enhancing mineral dissolution rates through both direct and indirect microbe-mineral interactions. Endospore enhanced dissolution accelerates the chemical system toward supersaturation with respect to secondary mineral precipitates.

5.3 Experimental Procedures

5.3.1 *B. subtilis* endospore growth and isolation

We grew and isolated *B. subtilis* endospores according to Harrold et al. (2011). Briefly, we aseptically inoculated *B. subtilis* into 3.5 mL of 3 % typticase soy broth (TSB) and 0.5 % yeast extract from cultures maintained on agar plates. Cultures were incubated for 24 h, transferred to 1 L of 0.3% TSB and incubated for an additional 6 days at 32 ^{o}C prior to harvesting. We isolated the endospores with a two-phase, polyethylene glycol 4000 and potassium phosphate buffer separatory solution (Chapter 2, Harrold et al., 2011; Sacks and Alderton, 1961). Endospores were washed in 0.1 M $NaClO_4$ and pelleted as previously described (Chapter 2, Harrold et al., 2011), prior to use in adsorption assays. The average spore harvest purity for this method as determined by Harrold et al. (2011) is 88 ± 11% (1σ) with a median value of 93 %.

5.3.2 Forsterite characterization and preparation

Naturally occurring forsterite grains (Alfa Aesar) were crushed using a corundum mortar and pestle and subsequently sieved. Care was taken to remove dark green to black mineral impurities from the final mineral powder during crushing. We retained the sieve fraction < 125 μM for use in forsterite dissolution assays. Some fines were removed by sedimenting the powder in 18 MΩ cm^{-1} H_2O and decanting the supernatant. Many fines remained as evidenced by SEM images of the unreacted forsterite powder (Fig. 5.1A). Sufficient forsterite powder was homogenized for use in all dissolution assays. A Bruker F8 Focus Powder X-ray diffractometer

(XRD) was used to confirm the structure of the mineral powder and identify any mineral phase impurities (Fig. 5.2). We determined the chemical identity of grains within the forsterite powder (Table 5.1) using a JEOL 733 Superprobe, electron microprobe calibrated with an internal olivine standard. Forsterite powder was mounted in an epoxy puck and polished to 0.5 μm prior to microprobe analysis. Powder surface area was determined by Brunauer-Emmett-Teller (BET) analysis (Table 5.2).

5.3.3 Dialysis assays: indirect microbe-mineral interaction

We eliminated endospore-mineral adhesion and isolated the effect of adsorption on forsterite dissolution by physically separating endospores and mineral grains with dialysis tubing. Abiotic controls and biotic dissolution assays were conducted in 25 mM $NaClO_4$, made with 18 MΩ cm^{-1} H_2O, to buffer changes in ionic strength from pH probe leaching, pH adjustments and mineral dissolution. Endospores were added gravimetrically to the bulk solution of each biotic dissolution assay to achieve concentrations of 0.05, 0.10, 0.20 and 0.66 g L^{-1} (wet weight). Unreacted forsterite powder was sequestered in suspended dialysis membrane capsules (Spectra/Por Float-a-lyzer G2) with a 1 mL volume capacity and molecular weight cut off (MWCO) of 1000 kD (~0.1 μm). The largest MWCO available was chosen to facilitate diffusion and mixing between the encapsulated forsterite and bulk solution. Forsterite was added gravimetrically to the dialysis capsules to minimize deviations in surface area. Total forsterite concentration in each assay was 1.25 g L^{-1}. Dialysis bound forsterite capsules were suspended in the endospore and abiotic control assays for between 46 and 95 d. Assays were mixed continuously using a Teflon coated magnetic stir-bar over the duration of incubation to promote solution heterogeneity and equilibration between the dialysis bound mineral and bulk solution. All biotic and abiotic control assays were run in duplicate.

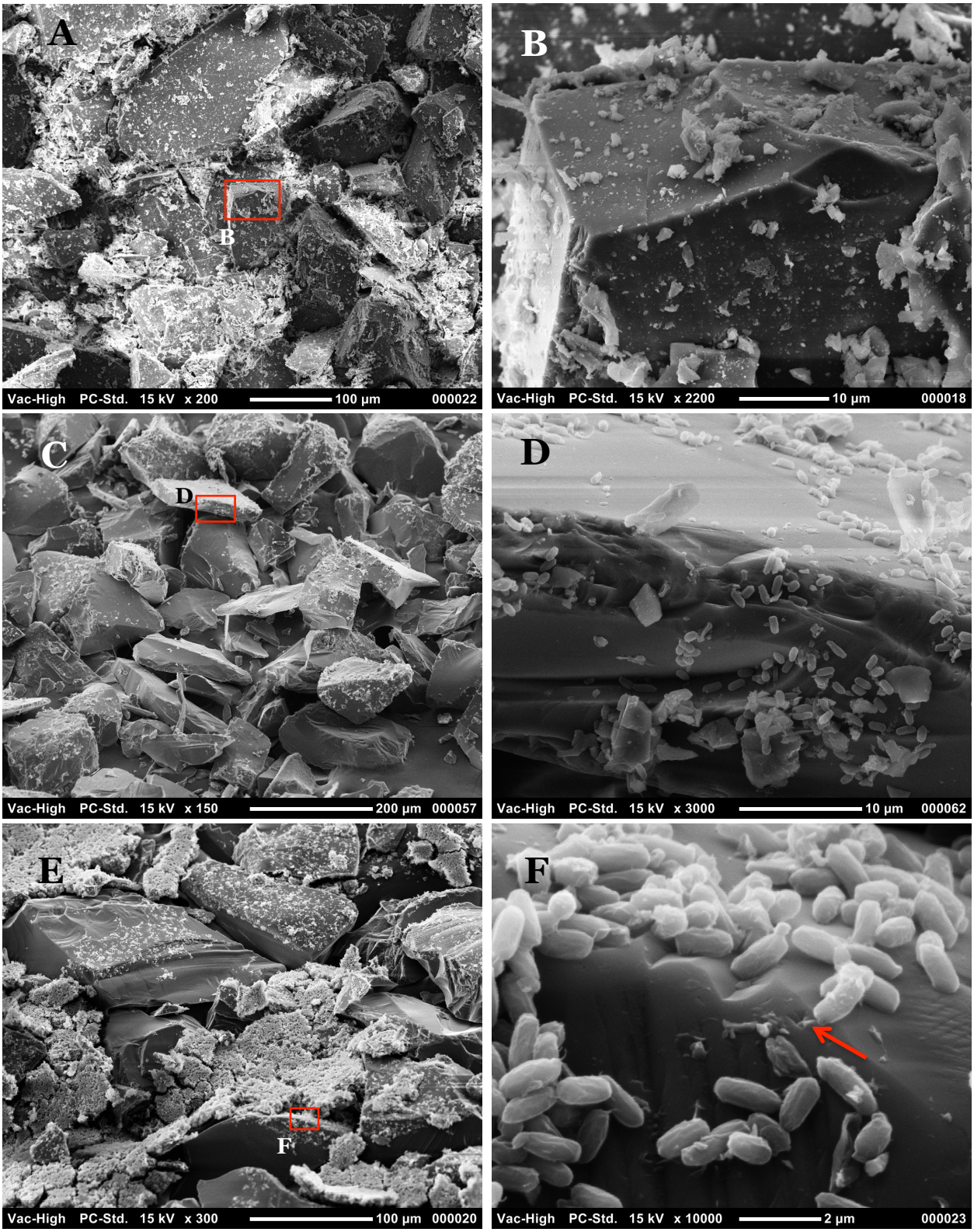

Figure 5.1. Panels A and B) SEM image of unreacted forsterite powder reveals a wide range of grain sizes. Fine particulates likely lead to large variation in BET surface area results. Panels C and D) Assay 9H exhibits a clear decrease in total fines relative to unreacted forsterite (A and B). Panels E and F) Assay 4H with masses of endospores clumping on forsterite grains after filtration. Potential etch pits features are visible in panel F (arrow).

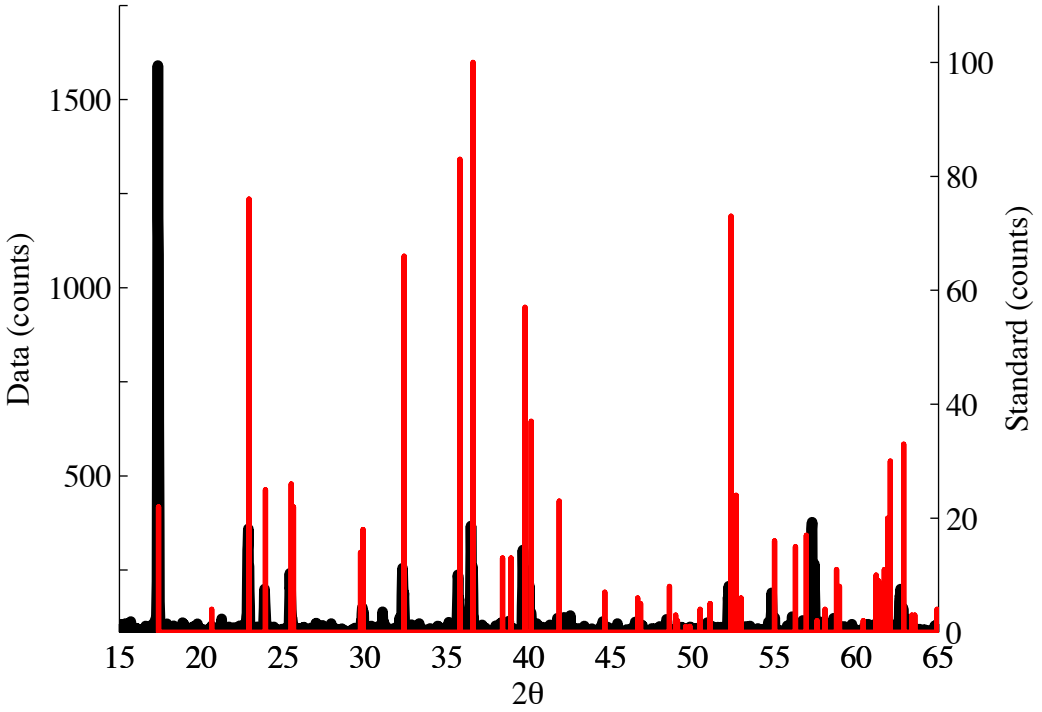

Figure 5.2. X-ray diffraction patterns for $Fo_{89.5}$ powder use in dissolution assays and forsterite standard XRD pattern (standard #34-189, Morris, 1984).

We sampled the bulk solution immediately after assembling each assay, twice a day for the first 10 days, once a day for days 10-15 and semiweekly thereafter. Sample volumes between 3 and 5 mL were removed via volumetric pipette and recorded. Samples were filtered with a 0.10 μm Millipore Isopore™ membrane filter to match the MWCO of the dialysis tubing and split into 1 mL aliquots for subsequent Si, Mg and Ca, and Dipicolinic acid (DPA) analyses. Aliquots for Si and Mg/Ca analysis were treated with 2 μL of 8 M NaOH or 10 M trace metal free HNO_3, respectively, and chilled at 4 °C prior to analysis. After sample removal, we measured and recorded the pH of each assay (pH_o) with an Orion 8103BN Ross semi-micro combination pH electrode calibrated with 4 NIST standards. Assay pH was adjusted to 7.5 ± 0.3 as necessary with 10 μL additions of 1 M NaOH or HNO_3. pH_o is regarded as the steady state pH of the assay at each sample point. We report the average, maximum and minimum pH_o for each assay (Table 5.3). Complete serial data for each sample includes time of sampling, volume removed,

Table 5.1. Forsterite chemical composition

		Major Elements (mol g^{-1})			Trace Elements (mol g^{-1})				Calculated (mol g^{-1})
Sample	**Total (%)**	**Si**	**Mg**	**Fe**	**Cr**	**Mn**	**Ni**	**Ca**	**O**
Fo-unreacted	98.16	6.858E-03	1.165E-02	1.320E-03	0	1.707E-05	4.743E-05	1.003E-05	2.676E-02
4H -1	99.84	6.740E-03	1.178E-02	1.563E-03	0	2.459E-05	4.616E-05	1.856E-05	2.691E-02
4H -3	98.98	6.733E-03	1.222E-02	1.207E-03	1.769E-06	2.011E-05	4.968E-05	1.624E-05	2.698E-02
4H -4	99.15	6.776E-03	1.217E-02	1.221E-03	6.924E-07	1.518E-05	6.088E-05	1.148E-05	2.703E-02
4H -5	99.02	6.605E-03	1.174E-02	1.585E-03	1.250E-06	2.162E-05	5.490E-05	1.075E-05	2.662E-02
4H -6	98.83	6.747E-03	1.214E-02	1.221E-03	0	1.609E-05	5.064E-05	1.510E-05	2.694E-02
4H -7	98.63	6.569E-03	1.222E-02	1.296E-03	0	2.144E-05	5.031E-05	1.270E-05	2.674E-02
4H -8	98.66	6.733E-03	1.194E-02	1.320E-03	3.269E-07	2.068E-05	5.294E-05	1.115E-05	2.681E-02
4H -9	98.71	6.687E-03	1.209E-02	1.271E-03	2.173E-06	1.899E-05	6.159E-05	1.255E-05	2.683E-02
4H -10	99.21	6.690E-03	1.222E-02	1.277E-03	2.173E-06	1.997E-05	5.062E-05	1.407E-05	2.696E-02

Sample	**M_{total}:Si**	**Si/O_4**	**Mg/O_4**	**Fe/O_4**	**Cr/O_4**	**Mn/O_4**	**Ni/O_4**	**Ca/O_4**
Fo-unreacted	1.902	1.0251	1.7412	0.1973	0	0.0026	0.0071	0.0015
4H -1	1.993	1.0017	1.7513	0.2323	0	0.0037	0.0069	0.0028
4H -3	2.007	0.9983	1.8119	0.1790	0.0003	0.0030	0.0074	0.0024
4H -4	1.989	1.0028	1.8006	0.1807	0.0001	0.0022	0.0090	0.0017
4H -5	2.031	0.9924	1.7644	0.2381	0.0002	0.0032	0.0082	0.0016
4H -6	1.993	1.0018	1.8028	0.1813	0	0.0024	0.0075	0.0022
4H -7	2.070	0.9827	1.8280	0.1939	0	0.0032	0.0075	0.0019
4H -8	1.983	1.0046	1.7822	0.1969	0.0000	0.0031	0.0079	0.0017
4H -9	2.012	0.9970	1.8024	0.1896	0.0003	0.0028	0.0092	0.0019
4H -10	2.030	0.9927	1.8132	0.1894	0.0003	0.0030	0.0075	0.0021
Average	*2.00*	*1.00*	*1.79*	*0.20*	*0.0001*	*0.0029*	*0.0078*	*0.0020*
1 σ	*0.04*	*0.01*	*0.03*	*0.02*	*0.0001*	*0.0004*	*0.0008*	*0.0004*
% ($Fo_{89.5}$)	100.0		89.5	9.9	0.0	0.1	0.4	0.1

pH_o and adjusted pH (pH_{adj}), if adjustments were made. All experiments were conducted at ambient laboratory temperature, controlled at 23 ± 0.3 °C.

Experiments were disassembled immediately after taking the final sample. The bulk solution was filtered with a 0.22 μM Millipore Isopore™ membrane filter to collect endospores and any particulates. Weathered forsterite grains were removed from the dialysis capsules and filtered as described for bulk solution filtrates. Portions of the filtrates were rinsed with 18 MΩ cm^{-1} H_2O to remove any residual electrolytes and prevent salt crystallization upon drying. All filtrates were dried on their filter membranes in individual petri dishes at ambient laboratory temperature, sealed with Parafilm and stored for subsequent SEM imaging.

Table 5.2. Forsterite powder surface area

Run #	BET surface area (m^2 g^{-1})
1	3.9940
2	0.8241
3	4.3210
4	2.5530
5	0.7203
6	1.5950
7	5.3880
8	0.6348
Average	2.5
1 σ	1.7

5.3.4 Homogeneous assays: indirect and direct microbe-mineral interaction

Homogeneous assays measure the effect of both endospore adsorption and endospore-mineral adhesion on the rate of Fo_{90} dissolution. Assays were assembled by gravimetrically adding endospores and forsterite powder to a 25 mM $NaClO_4$ electrolyte made with 18 MΩ cm^{-1} H_2O. Forsterite dissolution was tested at endospore concentrations of 0.05, 0.10, 0.20 and 0.66 g L^{-1} (Table 5.3). Abiotic control assays were assembled without endospores. The total forsterite

concentration in each assay was 1.25 g L^{-1}. All assays were mixed end-over-end to maintain solution heterogeneity.

Assays were vigorously mixed just prior to sampling to suspend all particulates and collect a homogeneous solution-endospore-mineral sample. This approach maintains the original microbe-mineral ratio for the duration of experimentation. Samples were filtered with 0.10 or 0.22 μm Millipore Isopore™ membrane filters, separated into aliquots and stored as previously described for dialysis assays. We measured and recorded solution pH after sample removal (pH_o) and adjusted the pH as necessary (see section 5.2.2). We report the average, maximum and minimum pH_o for each homogeneous assay (Table 5.3).

Homogeneous assay filtrates collected at the end of the experiment contain both endospore and forsterite components. Filtrates were prepared, dried and stored as previously described for dialysis assays.

5.3.5 Chemical analyses

Silica (Si) concentrations were determined based on a molybdenum (Mo) blue colorimetric method (Marczenko, 1976). This method determines the concentration of monomeric and dimeric silicic acid in solution. Samples were pre-treated with base as previously described (see section 5.2.2) to maintain Si in the aqueous monomeric silicic acid state prior to analysis. Briefly, up to 580 μL of sample was combined with 120 μL of a Mo solution containing 16.2 mM ammonium-Mo tetrahydrate in 0.7 M HCl, and let stand for 15 m. We doubled the total Mo added relative to the method described by Iler (*in* Marczenko, 1976) to ensure sufficient reagent was available to complex all silica in solution. Following Si complexation with Mo, 300 μL of a reducing solution was added containing 19.4 mM Metol, 31.7 mM sodium sulfite and 0.22 M oxalic acid in 3.6 N H_2SO_4. Colorimetric assays were allowed to develop for 1.5 h prior to analysis.

Table 5.3 Experimental parameters for dialysis and homogeneous assays

Dialysis Assays

Assay ID	[endospore]$_o$ (g L^{-1})	[Fo_{90}] (g L^{-1})	Average pH_o	Maximum pH_o	Minimum pH_o	Duration (d)
1H[1] control	n.a.	1.251	7.57 ± 0.26	8.701	7.318	81.07
2H[1] control	n.a.	1.253	7.58 ± 0.27	8.753	7.323	81.07
3H[1]	0.656	1.260	7.62 ± 0.18	8.490	7.340	83.80
4H[1]	0.660	1.255	7.60 ± 0.19	8.506	7.152	83.80
5H	0.200	1.250	7.55 ± 0.28	8.628	7.300	41.87
6H	0.200	1.245	7.52 ± 0.34	9.003	7.280	41.87
7H	0.100	1.251	7.46 ± 0.32	8.862	7.224	41.87
8H	0.114	1.250	7.50 ± 0.33	8.947	7.293	41.87
9H	0.050	1.250	7.49 ± 0.33	8.947	7.251	41.87
10H	0.050	1.251	7.49 ± 0.30	8.934	7.293	41.87

Homogeneous Assays

Assay ID	[endospore]$_o$ (g L^{-1})	[Fo_{90}] (g L^{-1})	Average pH_o	Maximum pH	Minimum pH	Duration (d)
1D control	n.a.	1.251	7.40 ± 0.16	7.594	6.973	56.82
2D control	n.a.	1.250	7.38 ± 0.12	7.543	6.954	46.64
3D	0.650	1.250	7.41 ± 0.27	7.666	6.568	56.82
4D	0.660	1.249	7.36 ± 0.09	7.632	7.181	46.64
5D	0.200	1.247	7.40 ± 0.15	7.840	7.144	95.96
6D	0.200	1.250	7.36 ± 0.13	7.657	7.080	95.96
7D	0.100	1.250	7.37 ± 0.12	7.55	7.024	96.98
8D[2]	0.100	1.250	7.37 ± 0.17	7.838	7.087	95.97
9D	0.051	1.250	7.35 ± 0.14	7.635	6.983	95.98
10D	0.050	1.247	7.35 ± 0.15	7.711	7.028	95.99

[1] filtered with 0.22 μm filter. [2] dialysis tubing rupture recorded at $t \cong 41.8$ d (3.4×10^6 s)

We measured sample and standard absorbance relative to a Si-free blank on a double beam Cary 300 Bio UV-Vis spectrophotometer at 810 nm with a 1 s average read interval. Samples and standards were analyzed in triplicate using sample-standard bracketing technique to monitor for changes in standard absorbance. Sample and standard absorbance was stable over the duration of the analysis. Sample concentration was determined based on a minimum 5-standard linear calibration curve. Calibration lines exhibited R^2 of 0.98 or better. Errors are propagated based on error in the linear calibration line and the sample dilution factor. All reported errors are 2σ unless otherwise noted.

Mg, Ca, Al, Mn, Fe, and Si were measured for a subset of samples on an inductively coupled plasma optical emission spectrometer (ICP-OES). Samples from acidified sample aliquots were diluted gravimetrically and acidified to 0.6 % HNO_3. Four matrix-matched, multi-element standards were used to calibrate the instrument and produced a calibration correlation coefficient of 0.99 or better. Sample-standard bracketing was used to monitor instrument performance for quality control purposes. Errors are propagated based on a 10 % analytical error in the ICP-OES data. All reported errors are 2σ unless otherwise noted.

5.3.6 Scanning Electron Microscopy (SEM)

Unreacted, abiotic and biotically weathered forsterite grains and endospores were imaged on a Joel JCM 4500 SEM. Samples were dried under ambient laboratory conditions, mounted on pucks with carbon tape and gold sputter coated three times to ensure complete coverage. Images were taken under high vacuum at 15 kV. Maximum magnification was 15-20,000 x.

5.4 Results

5.4.1 Forsterite characterization

XRD analysis of the forsterite powder exhibits evidence of preferential orientation (Fig. 5.2) likely due to the presence of larger (50 to 125 um) grains. Despite this, data indicate the powder is composed of crystalline forsterite with no clear evidence of contamination by other primary or secondary minerals. During electron-microprobe analyses, only one grain of orthopyroxene was identified within the analyzed epoxy grain mounts. This further suggests minimal contamination by mafic minerals or secondary precipitates. Microprobe data for 10 forsterite grains (Table 5.1) indicate an average powder composition of $Fo_{89.5}$ with a chemical formula of $(Mg_{1.79}Fe_{0.198}Ni_{0.016}\ (Ca,Mn)_{0.002})SiO_4$. BET surface area measurements (Table 5.2) are highly variable, ranging from 0.6 $m^2\ g^{-1}$ to 5.4 $m^2\ g^{-1}$ with an average surface area of 2.5 ± 1.7 $m^2\ g^{-1}$ (1σ, n=8). Variability in BET surface area is likely related to the abundance of fines within the forsterite powder (Fig. 5.1).

Forsterite impurities - Trace amounts of aqueous Ca^{2+} and Mn (II) within the forsterite are unlikely to have a large effect on the endospore-forsterite system. $[Ca]_{aq}$ range from 0.4 to 18.7 μM with an average of 2.7 ± 2.3 μM (1σ). $[Mn]_{aq}$ is negligible in all assays. It is prudent to note, however, that endospore surfaces, including those of *Bacillus* sp., are known to oxidize Mn (II) to Mn(IV) resulting in Mn(IV)-oxide (MnO_2) precipitation onto the endospore surface (e.g. Bargar et al., 2000; De Vrind et al., 1986; Mandernack et al., 1995). Based on the small [Mn] impurity in the forsterite (0.1 % of total metal content) and the highest aqueous Mg concentration measured (207 μM) we estimate 0.23 μM of MnO_2 precipitate. Fe-oxide precipitates are much more likely to effect the dissolution system due to a 2 order of magnitude higher concentration relative to Mn (see Section 5.4.3).

5.4.2 Dipicolinic Acid

Endospores contain a large reservoir of pyridine–2,6 dicarboxylic acid (dipicolinic acid, DPA) equivalent to 10 -15 % of their total dry weight, primarily located in their core. DPA within the endospore is chelated in a 1:1 stoichiometric ratio with Ca^{2+} and, to a much lesser degree, other divalent cations including Mg^{2+} (Setlow, 2006). As a dicarboxylic acid with a $pK_{a,1}$ and $pK_{a,2}$ of 2.07 and 4.66, respectively, DPA would be fully deprotonated under the circumneutral pH of the assays described herein. It follows that DPA is capable of complexing aqueous species and interacting with the forsterite surface in both dialysis and homogeneous dissolution assays. Other researchers show multi-functional carboxylic acids are indeed capable of increasing the dissolution rates of a wide range of silicates, including quartz and forsterite, through both direct and indirect pathways (Bennett, 1991; Bennett et al., 1988; Olsen and Rimstidt, 2008). Consequently, is it important to consider the concentration of DPA in all biotic dissolution assays.

Upon germination and outgrowth, endospores rapidly release DPA and the corresponding Ca^{2+} chelate into solution at concentrations upwards of 450 μM g-1 dry weight endospores. While there is some evidence of endospore rupture in SEM images (not shown), it is limited to a small fraction estimated at less than 1 %, of the total cells. Due to the absence of an obvious germination trigger, endospore rupture may have occurred via grinding under the stir bar or through the lysis of a small percentage of cells enveloping immature endospores. We estimate 3 μM of DPA release assuming 1 % of a 0.66 g L^{-1} endospore suspension ruptured.

DPA is also known to leach from the endospore under acidic to alkaline pH (Chapter 3, Harrold and Gorman-Lewis, 2013; Setlow et al., 2002). The DPA leach rate for an endospore suspension at circumneutral pH, akin to the conditions used herein, is slow relative to more acidic solutions. Based on data in Harrold et al. (2013, Chapter 3), and assuming a constant linear leach rate, we estimate a 0.66 g L^{-1} endospore assay incubated for 60 d would accrue 36 μM DPA.

Alternately, we can estimate the total DPA in solution based on [Ca^{2+}] assuming DPA release is accompanied by a concomitant release of Ca^{2+} in a 1:1 ratio regardless of pathway. This approach is further substantiated since Ca^{2+} within the $Fo_{89.5}$ is minimal (see section 5.3.1). Between 0.6 and 5 μM Ca^{2+} is observed in the abiotic control assays suggesting Ca^{2+} sources other than DPA, likely $Fo_{89.5}$ and contamination. The maximum [Ca^{2+}] in all biotic assays is 18.7 μM in assay 4D, containing 0.66 g L^{-1} endospores. The average [Ca^{2+}] for all biotic assays is 2.7 μM, similar to concentrations within abiotic control assays. These data suggest a maximum DPA contamination of 18.7 μM.

Olsen and Rimstidt (2008) observed a 6-fold increase in forsterite dissolution rate at pH > 4.2 for solutions containing 1 mM oxalate, a di-carboxylic acid. DPA concentrations estimated for the highest endospore concentration assays (0.66 g L^{-1}) range from 3 to 36 uM and are two- to three-orders of magnitude below previously described oxalate concentrations. Rapid initial dissolution rates determined for dialysis and homogeneous assays with 0.66 g L^{-1} endospores are approximately 1-order of magnitude (see section 5.4) faster than the abiotic dissolution rates. Based on our estimates and compared to findings by Olsen and Rimstidt (2008) is it unlikely that DPA is a major contributor to the overall rapid initial forsterite dissolution rate observed in the biotic dissolution assays described herein.

5.4.3 Dialysis assays

5.4.3.1 Aqueous Si

We isolated and measured the influence of *B. subtilis* endospore-ion adsorption on the rate of forsterite dissolution by sequestering the forsterite within dialysis tubing. Duplicates of four endospore concentrations and endospore free abiotic controls, for a total of 10 assays were monitored for durations ranging from 46 to 95 d (Table 5.3). Average solution pH ranging from 7.41 to 7.35 show little variation between assays over the duration of experimentation. The highest pH_o typically occurred near the end of each experiment while the most acidic pH_o was

observed within the first 1-2 d of dissolution. pH adjustments were required at nearly every sample point for the first 3-5 days of dissolution with solution pH_o often below the target pH range of 7.5 ± 0.3. Solution pH_o began to stabilize after approximately 5 days with subsequent pH adjustments made every few days, on an as needed basis.

Dialysis tubing creates a physical barrier between the mineral grains and suspended endospores while allowing forsterite dissolution products ≤ 1000 kD MW to pass through the membrane, equilibrate with the bulk solution and interact with the endospore surface. Samples were taken from the bulk solution for subsequent elemental analyses to determine the rate of forsterite dissolution. The forsterite powder, however, remains undisturbed over the course of the experiment. This method of sampling results in incongruent removal of the bulk solution relative to the mineral powder, effectively increasing the forsterite concentration and decreasing the endospore:forsterite ratio over time.

We correct for the change in effective forsterite concentration and solution volume by calculating the total moles of Si released at each time-step according to a step-wise linear integration from time *t-1* to *t* (Eq. 5.1).

Eq. 5.1 $$n_{x,t} = n_{x(t-1)} + \left(V_{(t-1)}\Delta_{t-1}^{t} M_x\right)$$

Where $n_{x,t}$ is the number of moles of analyte *x* at time *t*, $V_{(t-1)}$ is the total solution volume at time *t-1* and $\Delta_{t-1}^{t} M_x$ is the change in analyte concentration from time *t-1* to *t*. Applying Eq. 5.1 to low resolution sample sets such as the ICP-OES data (n=6 data points per assay) would smooth out any variation in dissolution behavior as a function of time due to the discrete stepwise integration. We therefore only apply Eq. 5.1 to the high-resolution (n=30-40 data points per assay) Si data determined from the Mo-blue method.

Dissolution rate is linearly related to mineral surface area (White and Brantley, 1995). Surface area determined by monolayer surface-gas adsorption and BET theory is commonly

used for normalizing mineral dissolution data (White and Brantley, 1995). While this approach may underestimate the reactivity of a mineral, based in part on the density of highly reactive sites on the mineral surface, it provides a basis for comparing dissolution rates. The BET surface area of forsterite powder measured in this research, however, is highly variable and imparts a large error on the dissolution data and rate if used to normalize Si data. We instead choose to normalize $n_{Si,t}$ to total grams of forsterite in each assay (Fig. 5.3-5). Dissolution data provided in $mol_{Si}\ g_{Fo}^{-1}$ for both dialysis and homogenous assays are directly comparable and minimize error. Dissolution rates are only normalized to BET surface area following complete data processing and modeling to enable comparisons with other published dissolution rates.

$[Si]_{aq}$ are one order of magnitude lower in all dialysis assays (Fig. 5.3 and 5.4) relative to their homogeneous assay counterparts (Fig. 5.3 and 5.5). The dialysis membrane may slow the diffusion of dissolution products into the bulk solution and lower $[Si]_{aq}$. The average steady state abiotic dissolution rates in both homogeneous and dialysis abiotic control assays are, however, statistically equivalent (Table 5.4, section 5.5.1). This suggests that diffusion though the dialysis membrane does not ultimately affect the dissolution rate. The rate of abiotic forsterite dissolution is relatively constant over the duration of the experiment (Fig. 5.3 and 5.4). Dialysis assays containing endospores, however, show a rapid increase in aqueous Si relative to abiotic controls during the first 5 to 10 days of incubation (Fig. 5.4). Total aqueous Si released over time increases with increasing endospore concentration. The rate of Si release and therefore the forsterite dissolution rate in each biotic assay slows drastically following the initial rapid dissolution phase. We term this data region the "transition point" (see section 5.5.1). Qualitatively, the rate of forsterite dissolution following the transition point in each biotic assay parallels the dissolution behavior observed in all abiotic control assays.

5.4.3.2 Aqueous Mg

Unlike Si data, $[Mg]_{aq}$ in the biotic assays parallel the behavior of $[Mg]_{aq}$ observed in abiotic assays (Fig. 5.6). These observations suggest endospores are adsorbing and lowering the activity of aqueous Mg in biotic, dialysis assays as forsterite dissolves (see Chapter 4). This behavior is in accordance with findings showing appreciable Mg-endospore adsorption at circumneutral pH and 25 mM ionic strength (see Chapter 4). We refrain from using $[Mg]_{aq}$ data to determine dissolution rates since $[Mg]_{aq}$ is affected by endospore adsorption, available data is at much lower resolution (n ≅ 6 data points per assay), and forsterite dissolution rates are typically calculated with Si dissolution (Oelkers, 2001; Olsen and Rimstidt, 2008; Pokrovsky and Schott, 2000b).

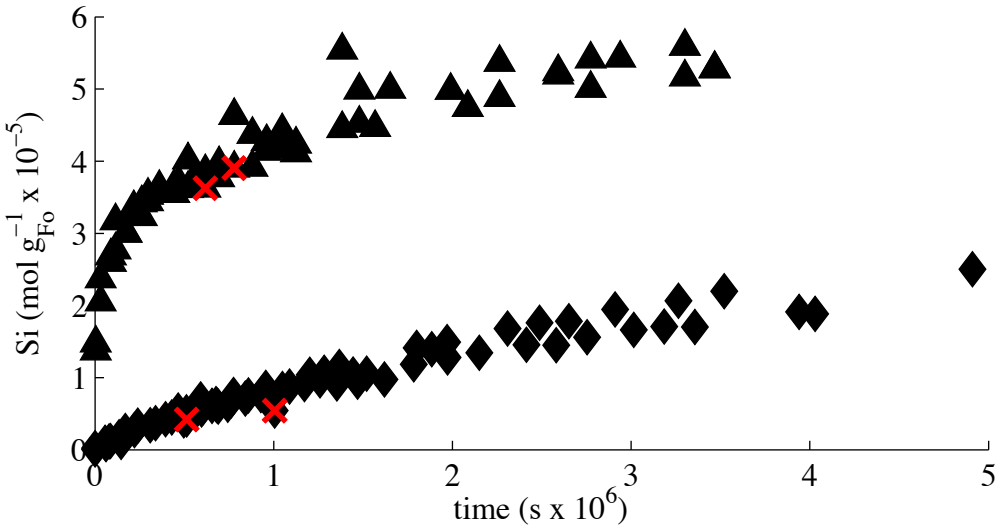

Figure 5.3 Si data for dialysis (black diamonds) and homogeneous (black triangles) abiotic control assays as a function of time. Data points encompass 2σ error. The calculated transition point (red "x") is provided for each assay. Rapid initial dissolution in the homogeneous control assays is likely due to the release of highly reactive sites on the forsterite surface. Rapid initial dissolution is tempered by diffusion thorough the dialysis membrane.

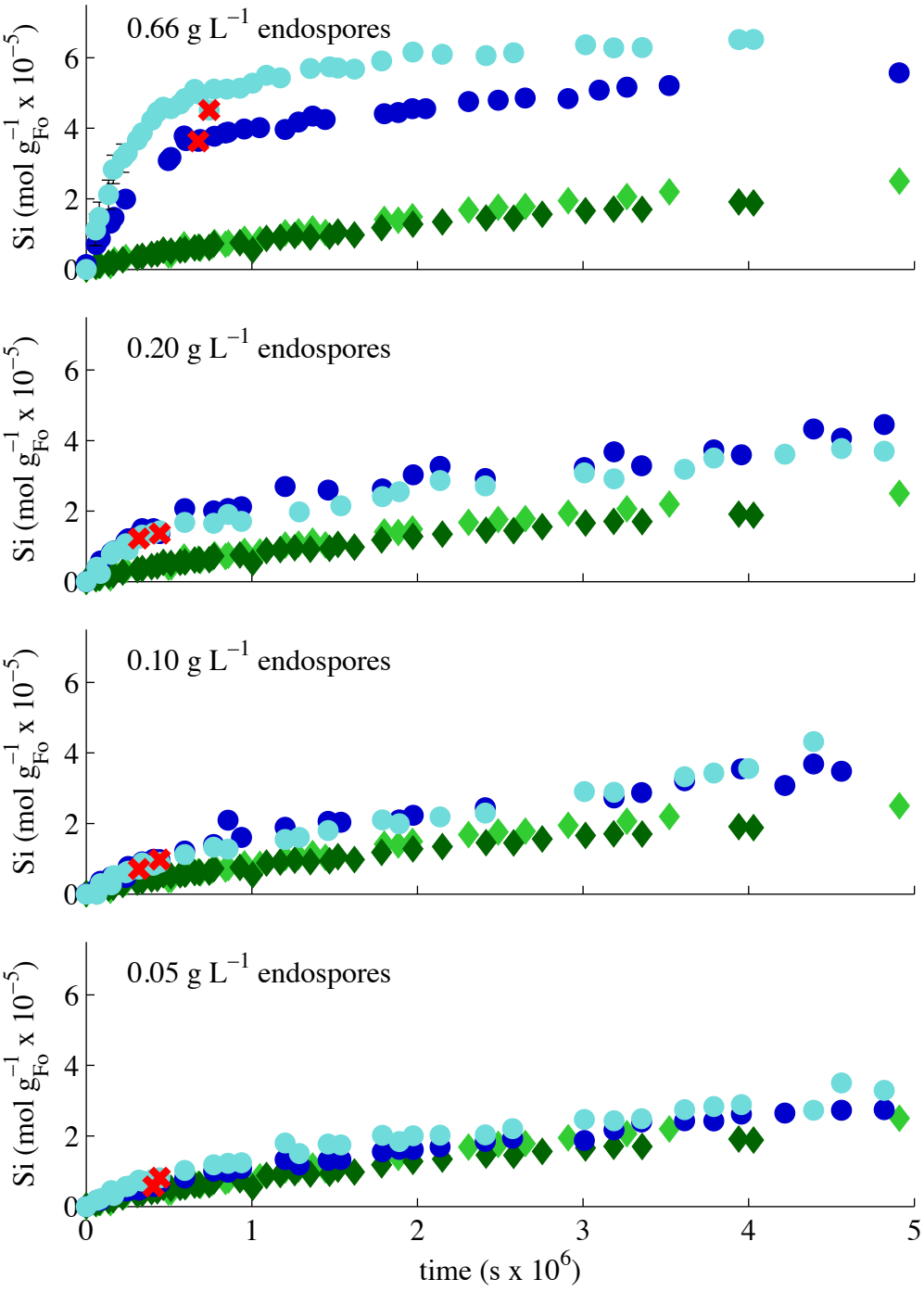

Figure 5.4 Dissolution data as a function of time for dialysis assays corresponding to 4 endospore concentrations (light and dark blue circles are duplicates). Calculated transition points (red "x") denote the end point for initial linear rate integrations. We provide abiotic control data (green diamonds) for comparison. Data points encompass 2σ error unless otherwise marked with error bars.

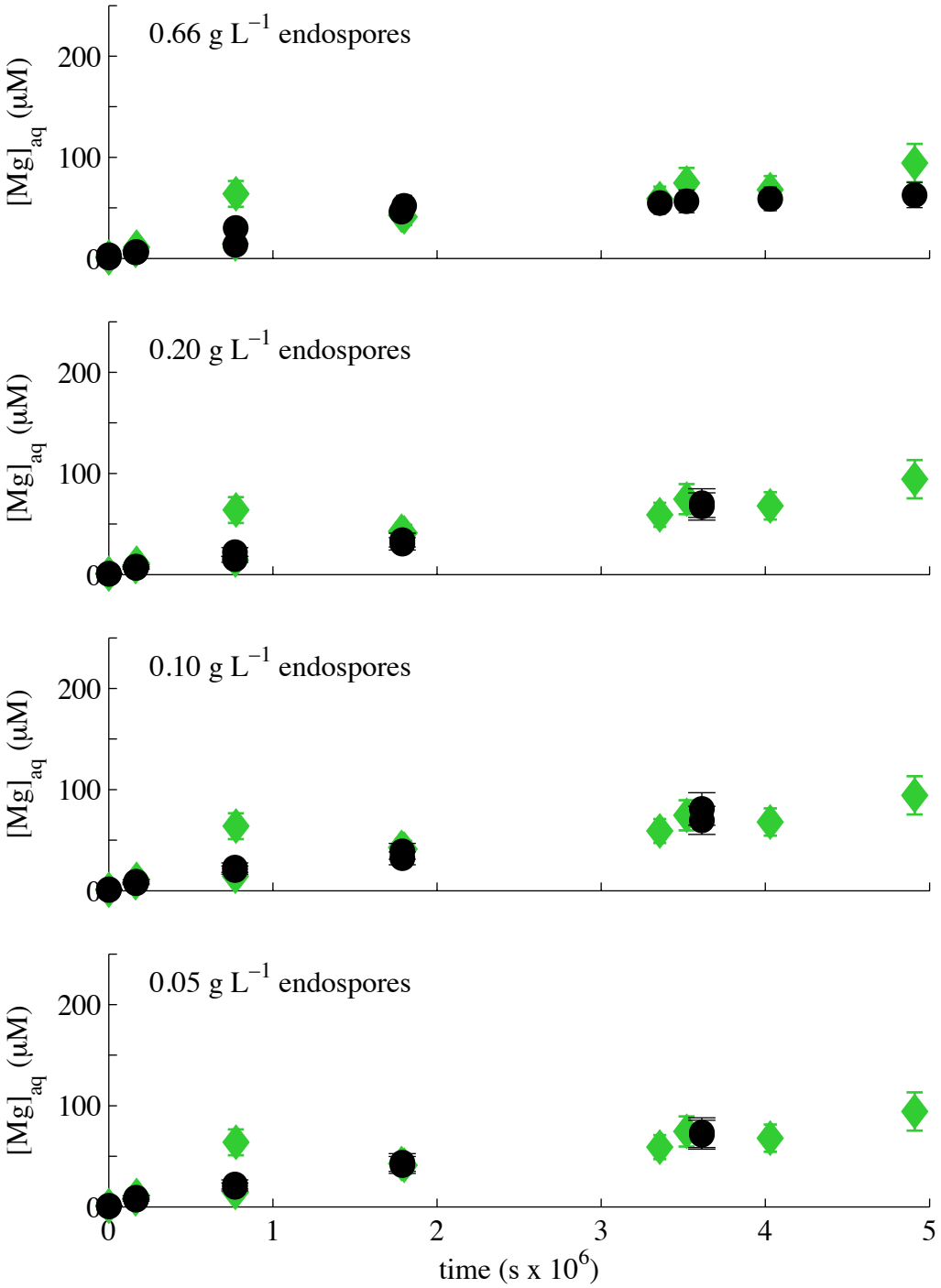

Figure 5.5 $[Mg]_{aq}$ for all biotic dialysis assays (black circles, 2σ error) compared to abiotic assay concentrations (green diamonds, 2σ error), Mg concentrations are equivalent in both biotic and abioitic dialysis assays despite rapid dissolution in the presence of endospores. This is achieved though Mg^{2+}-endospore adsorption.

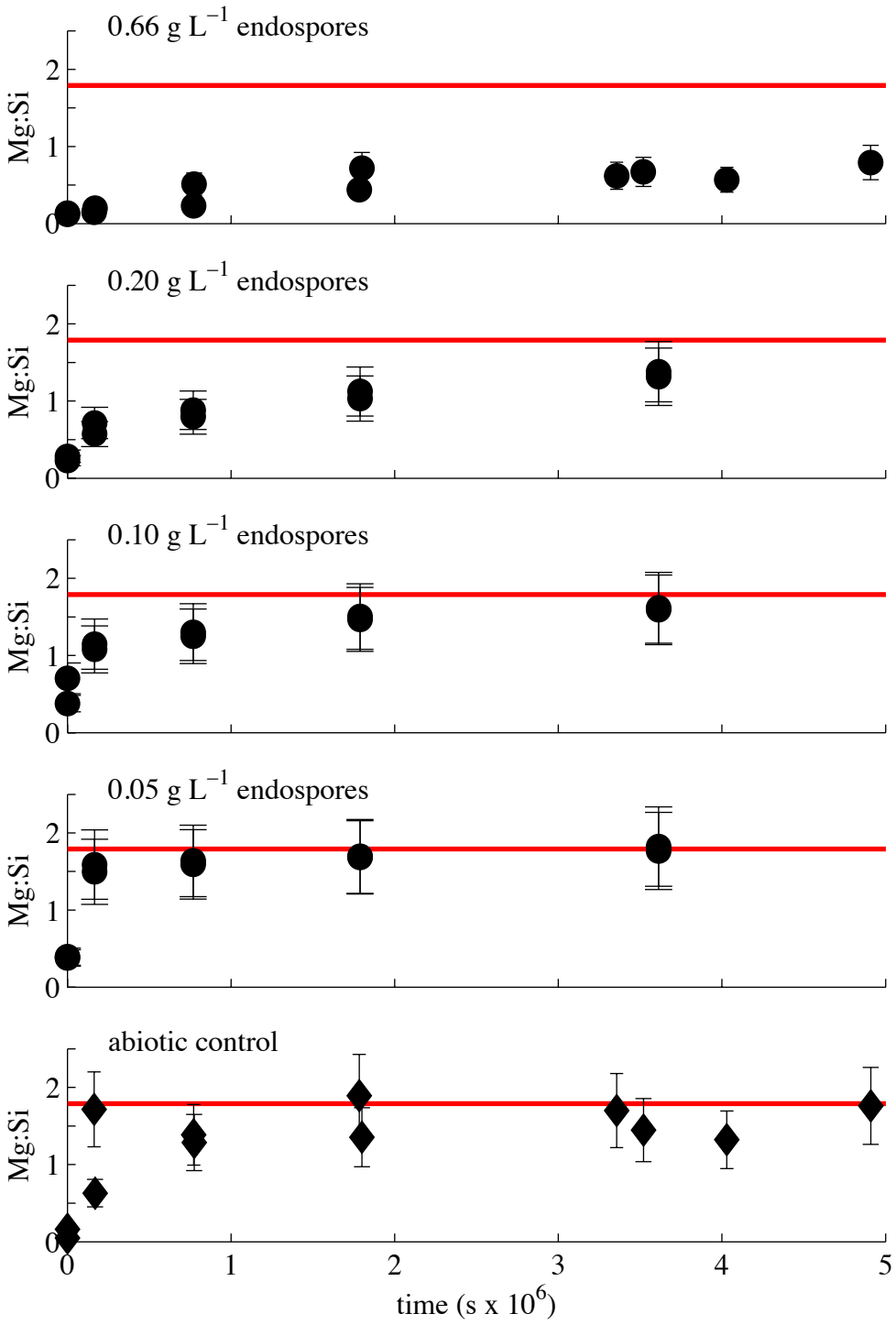

Figure 5.6 Mg:Si ratios as a function of time for biotic (black circles) and abiotic (black diamonds) dialysis assays. The Mg:Si ratio of $Fo_{89.5}$ is 1.79 (red line). Errors are 2σ.

5.4.3.3 Mg:Si ratio

ICP-OES data was used to determine the Mg:Si ratio over time in each assay. It was unnecessary to processes the ICP-OES data using a stepwise integration, as described in section 5.4.3.1, since the ratio of aqueous Mg and Si is unaffected by sample removal. The abiotic, dialysis control (Fig. 5.7) shows an initial Mg:Si ratio below the equilibrium value corresponding to congruent forsterite dissolution (1.79:1). This is in contrast to abiotic homogeneous controls, which exhibit congruent dissolution over the entire duration of incubation. It is possible that the dialysis membrane selectively inhibited forsterite dissolution products from equilibrating with the bulk solution. Within approximately 3 days the ratio achieves and maintains congruent dissolution for the remainder of the incubation. Biotic assays show a similar trend with a low Mg:Si ratio the beginning of dissolution which trends towards the congruent forsterite dissolution ratio. As endospore concentration increases the Mg:Si ratio takes longer to achieve the congruent dissolution ratio. In the 0.20 and 0.66 g L^{-1} endospore assays the Mg:Si ratio is always lower than the congruent dissolution ratio. This suggests the endospore surfaces create either a deficit of Mg, an excess of Si or both, relative to the 1.79 Mg:Si ratio observed within the forsterite structure.

5.4.4 Homogeneous assays

5.4.4.1 Aqueous Si

Homogeneous endospore dissolution assays allow both indirect endospore-ion interactions and direct endospore-forsterite adhesion to influence the rate of forsterite dissolution. Samples taken from each assay removed equal parts of solution, endospores and mineral powder, thereby maintaining the endospore:mineral ratio as well as the original endospore and forsterite concentrations. We calculate mol_{si} g_{Fo}^{-1} by normalizing the Mo-blue derived Si concentrations to the concentration of forsterite (Fig. 5.3 and 5.5).

Abiotic control assays exhibit an initial rapid increase in aqueous Si. At the atomic scale, mineral surface sites exhibit a range of reactivity related to the number of bonds remaining with the bulk mineral structure. Silica tetrahedral exposed at the forsterite surface, for example, can maintain between 1 and 4 bonds with the forsterite structure. Tetrahedra tethered by fewer bonds are more easily released from the mineral surface. The observed rapid initial increase in abiotic dissolution is likely due to the release of highly reactive sites on the mineral surface. Dissolution reaches a steady state once these highly reactive sites are released into solution (Fig. 5.3). Homogeneous biotic assays, however, show rapid initial dissolution beyond that observed in the abiotic controls. The extent of initial dissolution increases with increasing endospore concentration. After the initial dissolution phase, the rate of Si accumulation in all biotic assays taper off and parallel the abiotic dissolution rate (Fig. 5.5).

5.4.4.2 Aqueous Mg

$[Mg]_{aq}$ are similar in both biotic and abiotic homogeneous assays over the duration of incubation (Fig. 5.7). Akin to the trends observed in the dialysis assays (Fig. 5.6), Mg-endospore adsorption is likely responsible for lowering the $[Mg]_{aq}$ in homogeneous assays as forsterite dissolves. This interpretation is corroborated by previously discussed adsorption assays exhibiting significant Mg-endospore adsorption under equivalent aqueous conditions (see Chapter 4).

5.4.4.3 Mg:Si ratio

Mg:Si ratios in the abiotic homogeneous assays are at or near congruent forsterite dissolution for the duration of incubation (Fig. 5.9). Biotic assays show Mg:Si ratios decrease with increasing endospore concentration. This is the same trend observed in the biotic dialysis assays (Fig. 5.8), suggesting a similar dissolution mechanism involving a decrease in $[Mg]_{aq}$, increase in $[Si]_{aq}$ or both, relative to congruent dissolution observed in abiotic control assays.

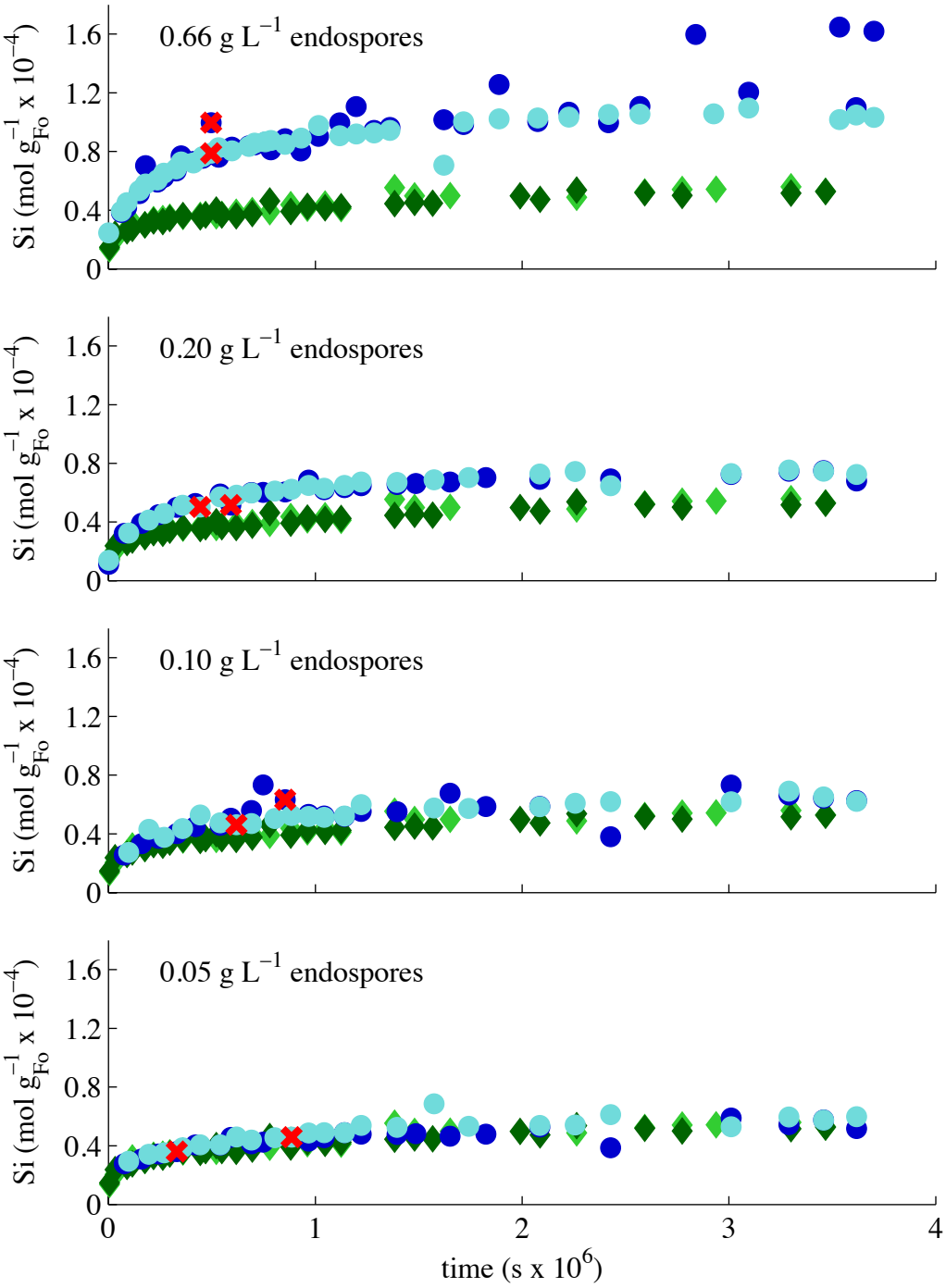

Figure 5.7 Forsterite dissolution in terms of $[Si]_{aq}$ as a function of time in homogeneous forsterite-endospore assays (duplicate assays in dark and light blue circles). Abiotic homogeneous control data is provided for comparison (dark and light green diamonds). Initial rapid dissolution rate decreases with decreasing endospore concentration. Calculated transition points (red "x") for biotic assays denote the end-point for linear rate regressions. Data points encompass 2σ error.

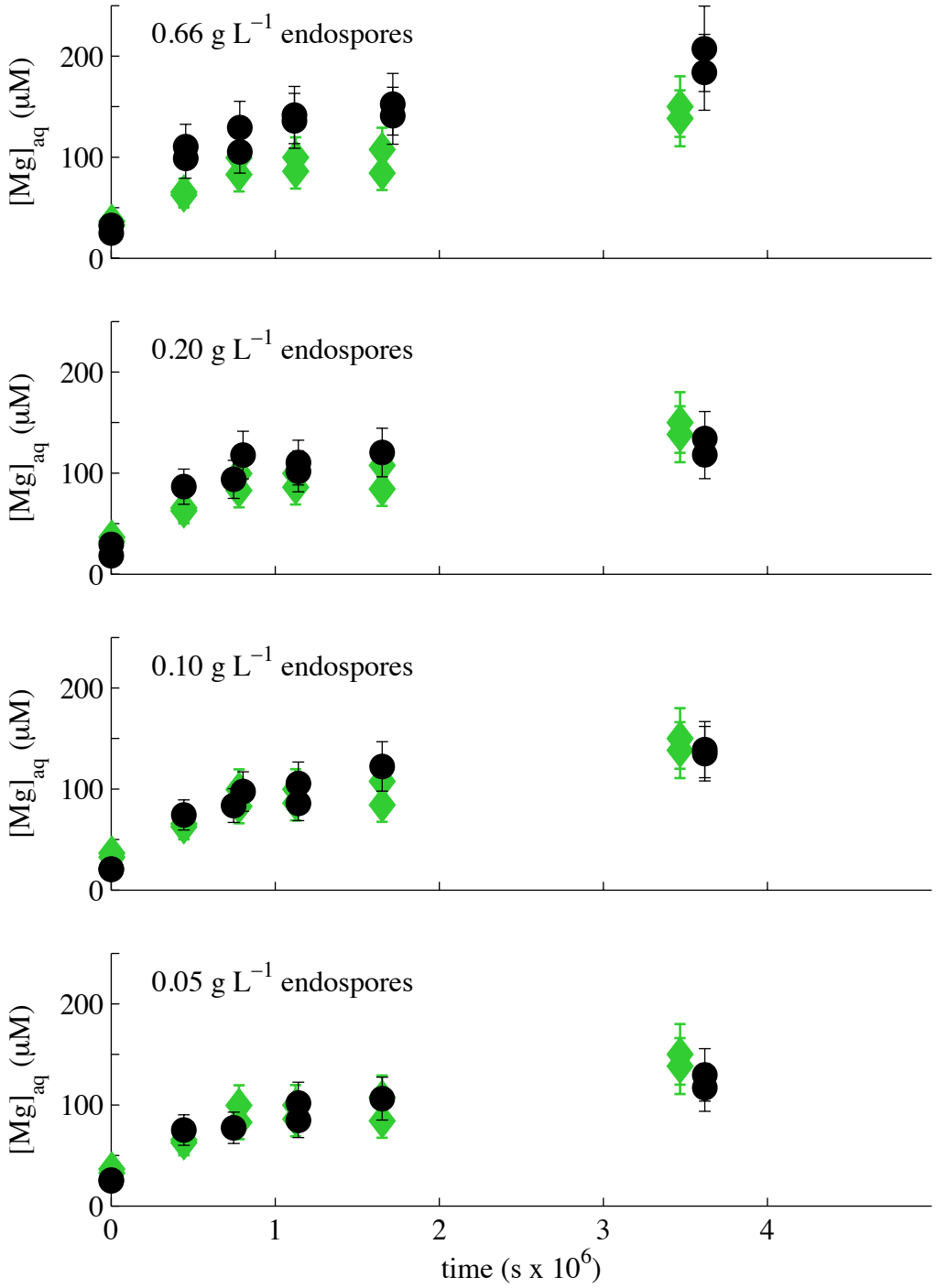

Figure 5.8 $[Mg]_{aq}$ for all biotic homogeneous assays (black circles, 2σ error) compared to abiotic assay concentrations (red diamonds, 2σ error), Mg concentrations are equivalent in both biotic and abioitic homogeneous assays despite rapid dissolution in the presence of endospores. This is achieved though Mg^{2+}-endospore adsorption.

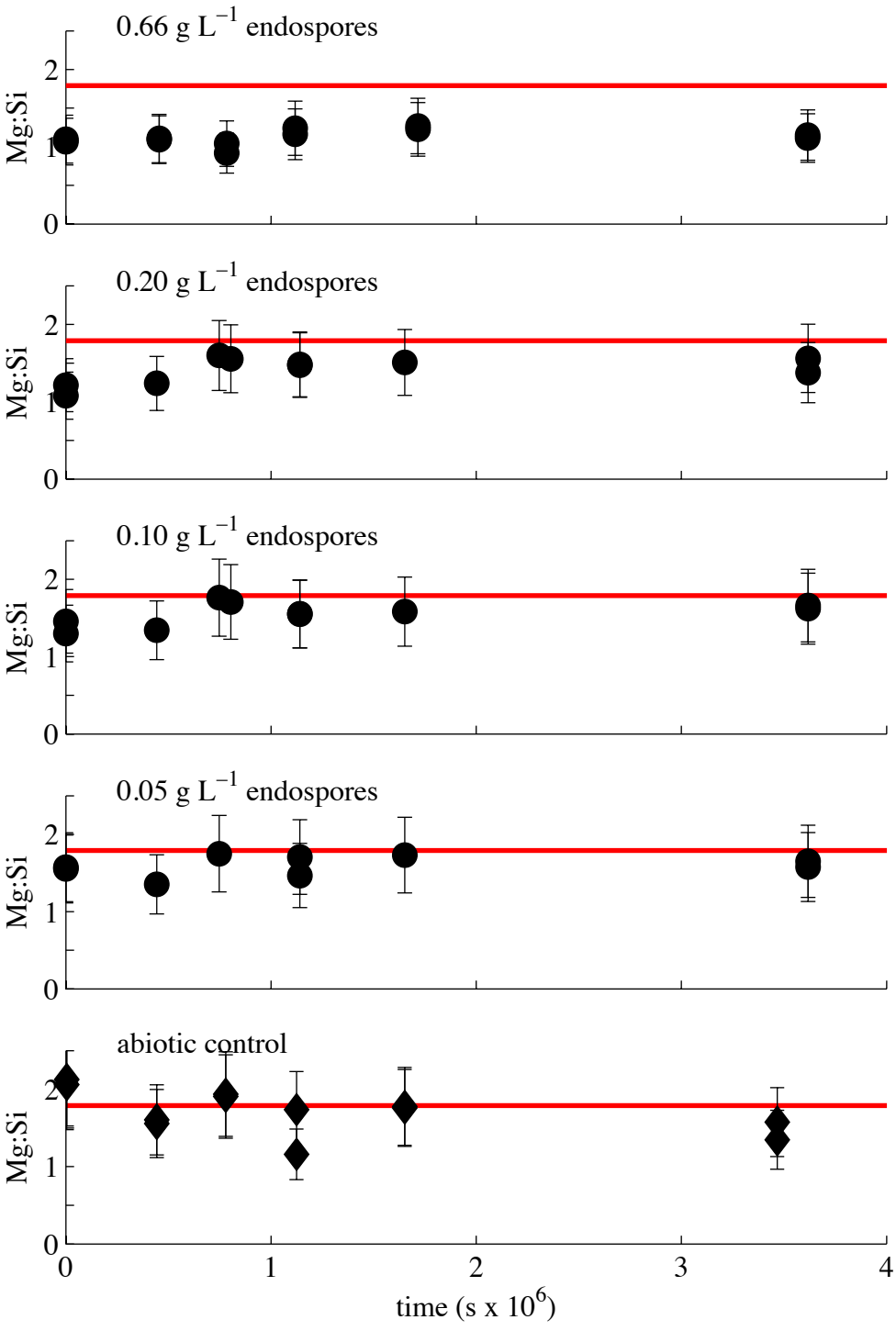

Figure 5.9 Mg:Si ratios as a function of time for biotic (black circles) and abiotic (black diamonds) homogeneous dissolution assays. The Mg:Si ratio of $Fo_{89.5}$ is 1.79 (red line). Errors are 2σ.

5.5 Modeling

5.5.1 Abiotic rate and transition point determination

We calculated the final, steady state forsterite dissolution rate in $mol_{Si}\ g_{Fo}^{-1}\ s^{-1}$ for all dialysis and homogeneous assays from the slope of a best-fit linear regression line describing data from 1–5 x 10^6 s (Table 5.4) and 1–4 x 10^6 s (Table 5.5), respectively. The average final steady state log dissolution rate for all dialysis assays is -11.33 ± 0.15 (2σ). Homogeneous assays show a statistically equivalent, average final steady state log dissolution rate of -11.34 ± 0.49 (2σ). Due to the distinct similarity between all biotic and abiotic final steady state dissolution rates in both the homogeneous and dialysis assays, we term this rate the abiotic dissolution rate ($r_{Si,abiotic}$). All rates are provided in log form (Tables 5.4 and 5.5)

The transition point (TP) is defined as the location where the rate of forsterite dissolution, or rate of Si release, transitions from the initial rapid dissolution rate to $r_{Si,abiotic}$. We define the TP quantitatively based on a threshold deviation from the $r_{Si,abiotic}$ regression line for data t < 1 x 10^6 s. In dialysis assays this threshold is defined as the first data point with a value that deviates from the abiotic linear regression line by 3σ (Fig. 5.3 and 5.4). Homogeneous assays, however, exhibit more data scatter resulting in larger 3σ, $r_{Si,abiotic}$ linear regression errors. The large data scatter included in the homogeneous $r_{Si,abiotic}$ linear regressions, coupled with a 3σ deviation threshold to determine the TP, results in a point position far from the visually estimated TP. We instead define homogeneous assay TPs as the first data point (t < 1 x 10^6 s) that deviates from the respective $r_{Si,abiotic}$ linear regression line by one tenth of the mean y value ($mol_{Si}\ g_{Fo}^{-1}$) divided by the standard deviation of the residuals (Fig. 5.3 and 5.5).

5.5.2 Isolating the indirect and direct biotic rate components

5.5.2.1 Indirect, endospore-ion adsorption

The initial rapid dissolution rate ($r_{Si,o}$) observed in dialysis assays is a function of both abiotic and indirect endospore-ion adsorption processes. We calculate $r_{Si,o}$ from the best-fit linear regression line for data from time t = 0 s up to the calculated TP (t_{TP}) for all dialysis assays (Table 5.4). Multivariate ANOVA tests indicate $r_{Si,o}$ determined for the three highest endospore concentrations are statistically different ($p \leq 0.05$) from the average initial ($r_{o,Si,abiotic}$) and steady state ($r_{Si,abiotic}$) abiotic dissolution rates. The rate component associated with indirect endospore-ion adsorption ($r_{Si,IS}$) is determined by subtracting the average $r_{Si,abiotic}$ from $r_{Si,o}$ for each experimental assay (Table 5.4).

To determine the dependence of $r_{Si,IS}$ on endospore concentration we utilize the chemical rate law as described by Eq. 5.2 (Nagy and Lasaga, 1992; Olsen and Rimstidt, 2008):

Eq. 5.2 $$R_{si} = r_{+} = k_{+} \prod_j a_j^{m_j} \left(1 - e^{\frac{\Delta G_r}{RT}}\right)$$

Where the total rate of Si release into solution (R_{si}) is approximately equal to the forward rate of dissolution (r_{+}) for assays undersaturated with respect to forsterite and secondary Si precipitates (see section 5.4.5). k_{+} is the rate constant of the forward reaction, a_j is the activity of the rate determining component j, m_j is the order of the reaction with respect to j, ΔG_r is the change in Gibbs free energy of the reaction, R is the gas constant and T is temperature in kelvin. When ΔG_r < -5RT, $\left(1 - e^{\frac{\Delta G_r}{RT}}\right)$ approaches 1 and the rate law can be simplified according to Eq 5.3. Assuming the highest observed $[Mg]_{aq}$ and $[Si]_{aq}$ of 207 and 186 μM (assay 3H), respectively, ΔG_r is −497 kJ mol^{-1} or -200RT, much less than the -5RT threshold. This is expected since forsterite, a primary silicate, dissolving at standard temperature and pressure at acidic to circumneutral pH is always far from equilibrium.

Table 5.4 Dialysis assays: linear regression model results

Assay ID	$[endospore]_o$	$\log(r_{Si,o})$ (mol g_{Fo}^{-1} s^{-1})[a]	n[b]	R^2	$\log(r_{Si,abiotic})$ (mol g_{Fo}^{-1} s^{-1})[a]	n[b]	R^2	$\log(r_{Si,IS})$ (mol g_{Fo}^{-1} s^{-1})[d]
3D	0.65	-10.28 ± 0.04	11	0.98	-11.37 ± 0.05	17	0.95	-10.32 ± 0.05
4D	0.66	-10.23 ± 0.10	18	0.84	-11.44 ± 0.08	19	0.89	-10.27 ± 0.11
5D	0.20	-10.49 ± 0.10	11	0.89	-11.32 ± 0.09	21	0.89	-10.56 ± 0.12
6D	0.20	-10.42 ± 0.11	8	0.91	-11.32 ± 0.06	21	0.94	-10.48 ± 0.13
7D	0.10	-10.65 ± 0.08	11	0.93	-11.29 ± 0.07	21	0.94	-10.75 ± 0.11
8D[c]	0.10	-10.61 ± 0.13	8	0.89	-11.17 ± 0.05	13	0.98	-10.70 ± 0.16
9D	0.05	-10.87 ± 0.08	10	0.94	-11.34 ± 0.04	21	0.97	-11.06 ± 0.15
10D	0.05	-10.73 ± 0.07	11	0.95	-11.34 ± 0.06	21	0.93	-10.86 ± 0.11
1D control	0.00	-11.11 ± 0.14	8	0.87	-11.35 ± 0.06	17	0.95	n.a.
2D control	0.00	-11.16 ± 0.08	22	0.87	-11.40 ± 0.05	19	0.95	n.a.
				Mean	**-11.33 ± 0.15**			

[a] 2 σ error based on the linear regression
[b] Number of data points included in linear regression
[c] Dialysis tubing ruptured at $t \cong 3.4 \times 10^6$ s, $r_{si,abiotic}$ excludes samples taken after dialysis burst.
[d] 2 σ error

Table 5.5 Homogeneous assays: linear regression model results

Assay ID	$[endospore]_o$	$\log(r_{Si,o})$ (mol g_{Fo}^{-1} s^{-1})[a]	n[c]	R^2	$\log(r_{Si,abiotic})$ (mol g_{Fo}^{-1} s^{-1})[a]	n[c]	R^2	$\log(r_{Si,DS(ss)})$ (mol g_{Fo}^{-1} s^{-1})[b]	$\log(r_{Si,DS(int)})$ (mol g_{Fo}^{-1} s^{-1})[b]
3H	0.66	-9.91 ± 0.11	12	0.85	-10.71 ± 0.21	17	0.53	-10.20 ± 0.25	-10.36 ± 0.35
4H	0.66	-10.01 ± 0.08	12	0.92	-11.23 ± 0.31	17	0.35	-10.42 ± 0.28	-10.72 ± 0.50
5H	0.20	-10.20 ± 0.19	13	0.78	-11.44 ± 0.18	16	0.69	-10.51 ± 0.42	-11.12 ± 1.67
6H	0.20	-10.10 ± 0.17	11	0.86	-11.46 ± 0.22	16	0.58	-10.32 ± 0.31	-10.60 ± 0.59
7H	0.10	-10.24 ± 0.09	18	0.90	-11.35 ± 0.53	16	0.21	-10.47 ± 0.20	-10.97 ± 0.64
8H	0.11	-10.29 ± 0.23	14	0.70	-11.35 ± 0.18	16	0.71	-10.56 ± 0.47	-11.43 ± 3.38
9H	0.05	-10.32 ± 0.17	8	0.90	-11.47 ± 0.37	16	0.34	-10.51 ± 0.29	-11.14 ± 1.22
10H	0.05	-10.52 ± 0.17	18	0.75	-11.63 ± 0.60	16	0.16	-10.89 ± 0.50	n.a.
1H control	0.00	-10.61 ± 0.16	17	0.69	-11.44 ± 0.30	15	0.48	n.a.	n.a.
2H control	0.00	-10.53 ± 0.14	15	0.77	-11.34 ± 0.15	15	0.78	n.a.	n.a.
				Mean	**-11.34 ± 0.49**				

[a] 2 σ error based on the best-fit linear regression describing Si dissolution data
[b] 2 σ error
[c] Number of data points included in linear regression

By taking the log of Eq. 5.3 it can be re-written as Eq. 5.4, which provides a linear relationship between dissolution rate and the rate-determining component, in this case [endospores].

Eq. 5.3 $$r_{si} = k_+ \prod_j a_j^{m_j}$$

Eq. 5.4 $$log(r_{Si}) = m_j log(a_j) + log(k_+)$$

We assume an activity coefficient of 1 for endospores and the associated surface bound reactive sites. Is it likely, however, that ionic strength plays a role in the degree to which endospores effect forsterite dissolution. Rates and rate models described herein are only valid at ionic strengths of 25 mM. A more detailed discussion regarding ionic strength is provided in section 5.6.

We plot $log(r_{Si,IS})$ versus $log([endospores])$ and model the data, excluding the 0.05 g L^{-1} endospore affected rates, with a best-fit linear regression (Eq. 5.5, Fig. 5.10). The slope and intercept of the model fit provide the order and rate constant, respectively, describing the effect of indirect endospore-ion adsorption on the rate of forsterite dissolution as a function of endospore concentration.

Eq. 5.5 $$log(r_{Si,IS}) = 0.52(0.06) * log([endopores]) - 10.19(0.04)\ \ (1\sigma),\ I = 25mM, pH\ 7.3$$

5.5.2.2 Direct endospore-mineral adhesion

$r_{Si,o}$ were determined for homogeneous assays based on the best-fit linear regression for dissolution occurring from t=0 to t_{TP} (Table 5.5). Multivariate ANOVA tests indicate $r_{Si,o}$ determined for the three highest endospore concentrations are statistically different ($p \leq 0.05$) from the steady state abiotic dissolution rate. The $r_{Si,o}$ measured for 0.66 g L^{-1} assays are

statistically different ($p \leq 0.05$) from the initial abiotic dissolution rate observed in the homogenous, abiotic controls ($r_{Si,o\ abiotic}$).

We isolate the rate component associated with direct, endospore-forsterite adhesion, $r_{Si,DS(ss)}$ or $r_{Si,DS(int)}$, by subtracting the model derived indirect endospore affected rate ($r_{Si,IS}$) and average steady state abiotic dissolution rate ($r_{Si,abiotic}$) or initial homogeneous abiotic dissolution rate ($r_{Si,o\ abiotic}$), respectively, from $r_{Si,o}$ (Table 5.5). The dependence of $r_{Si,DS,ss}$ and $r_{Si,DS,int}$ on [endospores] is modeled as previously described for $r_{Si,IS}$ (Figs. 5.11 and 5.12). Models exclude 0.05 g L^{-1} $r_{Si,DS}$ values. Best-fit linear models describing $r_{Si,DS(ss)}$ and $r_{Si,DS(int)}$ are provided in Eq. 5.6 and 5.7 (Figs. 5.11 and 5.12).

Eq. 5.6 $$log\left(r_{Si,DS(ss)}\right) = 0.31(0.14) * log([endospore]) - 10.23(0.10)\ \ (1\sigma),\ I = 25mM, pH\ 7.3$$

Eq. 5.7 $$log\left(r_{Si,DS(int)}\right) = 0.78(0.36) * log([endospore]) - 10.38(0.25)\ \ (1\sigma),\ I = 25mM, pH\ 7.3$$

5.5.2.3 Initial rate reconstruction

The complete rate law defining the initial forsterite dissolution rate at pH 7.6 to 7.3 and I= 25 mM in a homogeneous system is provided by Eq. 5.8 and is the sum of $r_{Si,abiotic}$, $r_{Si,IS}$ (Eq. 5.5) and $r_{Si,DS(int)}$ (Eq. 5.7).

Eq. 5.8 $$r_{Si,o} = 10^{-11.33} + 10^{-10.19}[endospore]^{0.52} + 10^{-10.38}[endospore]^{0.78}$$

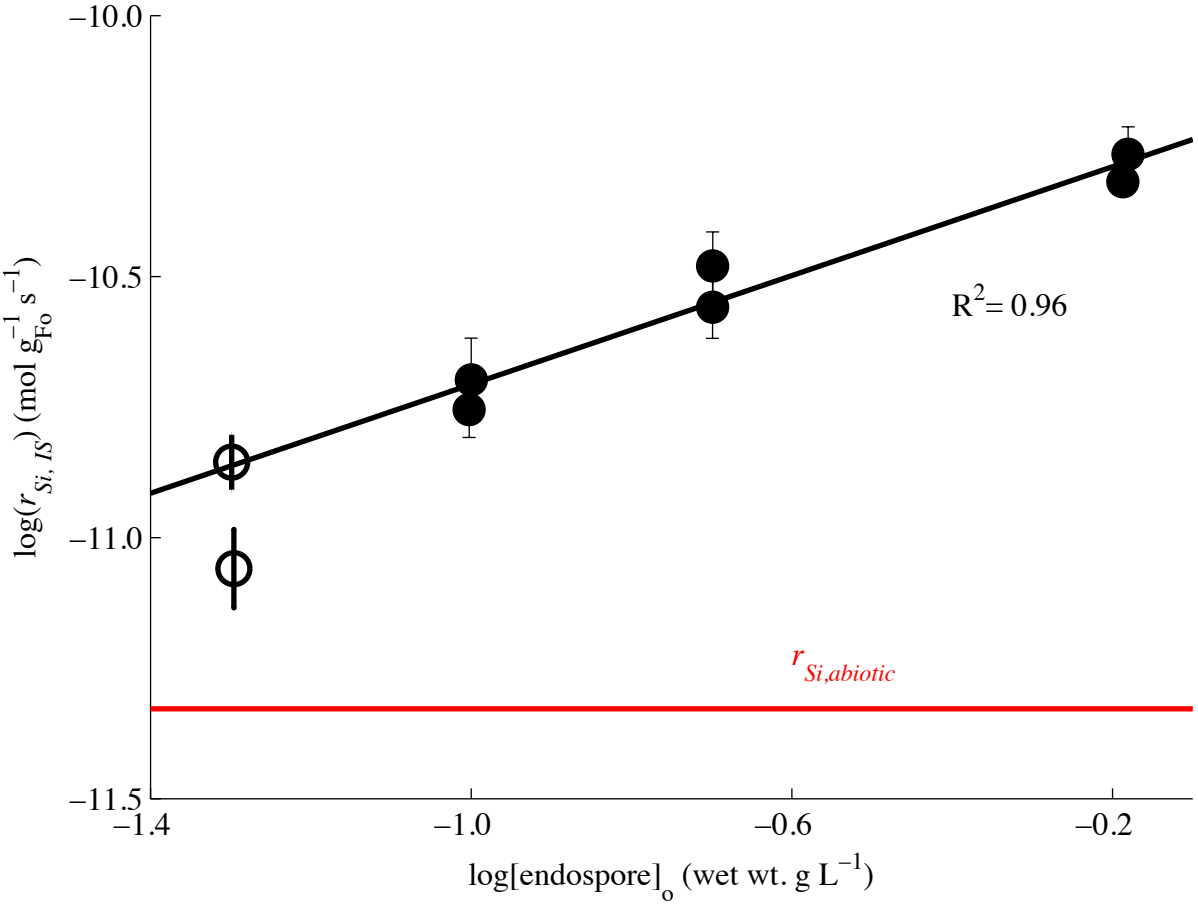

Figure 5.10. Indirect endospore-ion affected dissolution rate as a function of endospore concentration (black circles, 1σ error). The linear regression (black line) solves for the simplified rate law relating dissolution rate to endospore concentration. Data in open circles are excluded from the linear regression. Average abiotic dissolution rate (red line) is provided for comparison.

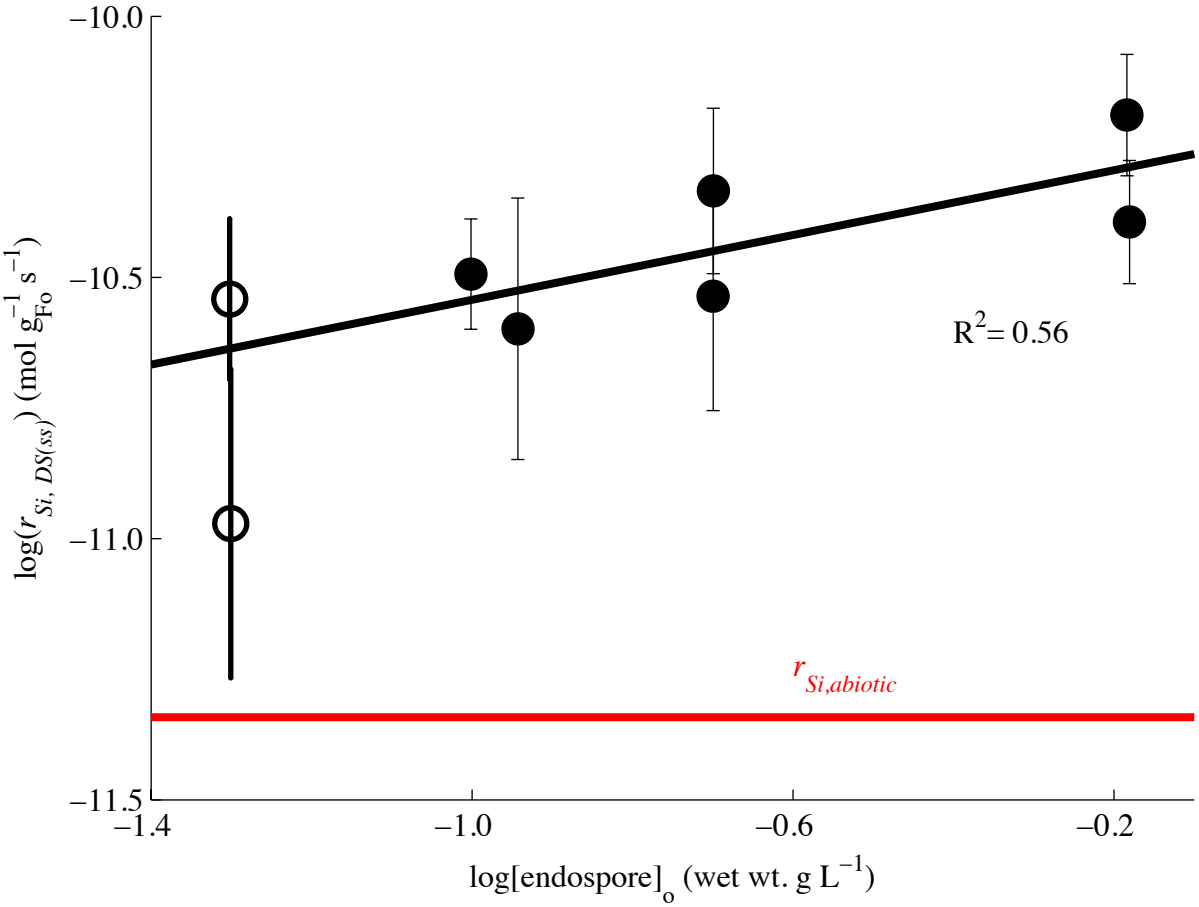

Figure 5.11. Forsterite dissolution rate ascribed to direct endospore-mineral adhesion based on the steady state abiotic dissolution rate ($r_{Si,DS(ss)}$) and presented as a function of endospore concentration (black circles, 1σ error). The linear regression (black line) describes the dependence of rate on endospore concentration according to the simplified rate law. Data in open circles are excluded from the linear regression. Average steady state abiotic dissolution rate (red line) is provided for comparison.

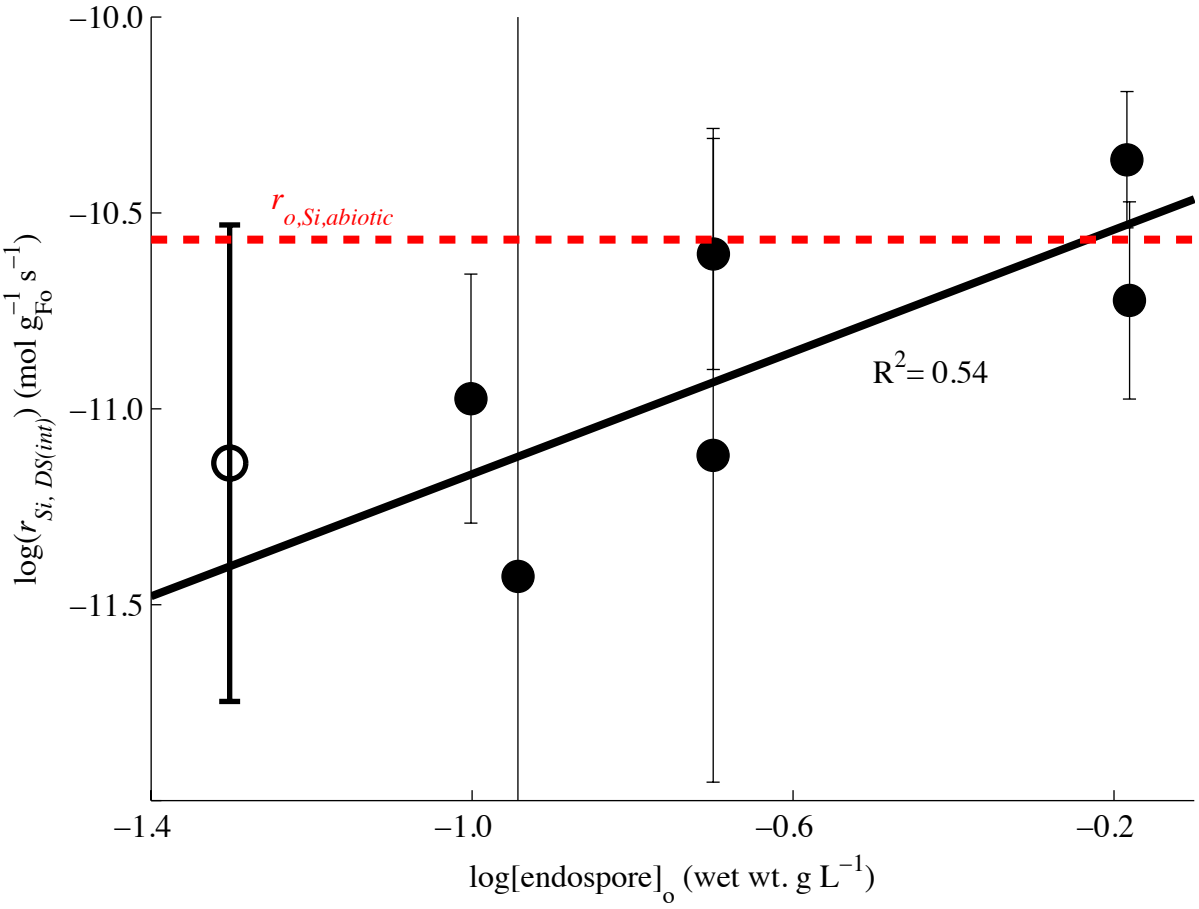

Figure 5.12. Forsterite dissolution rate ascribed to direct endospore-mineral adhesion based on the initial homogeneous abiotic dissolution rate ($r_{Si,DS(int)}$) and presented as a function of endospore concentration (black circles, 1σ error). The linear regression (black line) describes the dependence of rate on endospore concentration according to the simplified rate law. Data in open circles are excluded from the linear regression. Average steady state (solid red line) and initial (dashed red line) abiotic dissolution rates are provided for comparison.

5.5.3 Chemical equilibrium modeling

We utilized PHREEQC in conjunction with the Lawrence Livermore National Lab database to determine the saturation state of Fe, Si and Mg bearing mineral phases corresponding to experimental $[Mg]_{aq}$ and $[Si]_{aq}$ data and $[Fe]_{total}$ for homogeneous and dialysis assays 3H and 3D, respectively (Fig. 5.13). Model inputs included $[Mg]_{aq}$ and $[Si]_{aq}$ as determined from ICP-OES sample analyses (Fig. 5.13, panels C and F). $[Fe]_{total}$ was calculated based on $[Si]_{aq}$ according to the Fe to Si ratio measured in $Fo_{89.5}$ (0.198:1). Homogeneous assay 3H exhibited the highest concentration data of all 20 homogeneous and dialysis assays. Predominant species predicted within the assays includes SiO2 (or $Si(OH)_4$), Mg^{2+}, $Fe(OH)_3$, and $Fe(OH)_2^+$ at one order of magnitude less than its neutral counterpart.

Quartz and chalcedony (SiO_2) became supersaturated in assay 3H after 0.5×10^6 (~6 d) and 3.5×10^6 s (~ 40 d), respectively. Dialysis assay 3D was just under quartz saturation after ~ 45 d incubation and was always undersaturated with respect to chalcedony. Amorphous silica (SiO_2 am) was undersaturated in all assays. Based on these findings is it conceivable that SiO_2 underwent some form of precipitation within assay 3H during the approximately 45 d incubation period discussed herein. Mg is predicted to precipitate out with iron in ferrite-Mg ($MgFe_2O_4$), though the formation of this mineral requires high (90+ °C) temperatures (Omer et al., 2013). Magnesite ($MgCO_3$) is undersaturated in all assays.

The average and maximum $[Fe]_{aq}$ measured for all dissolution assays was 1.2 ± 0.7 μM (1σ) and 4.8 μM, respectively. Aqueous iron concentrations are much lower than the maximum 41 uM $[Fe]_{total}$ predicted for assay 3H, suggesting iron precipitation occurred. A variety of iron mineral phases were oversaturated in both assays. We show the SI for minerals containing both ferric and ferrous iron since iron within forsterite is in the Fe(II) oxidation state (Fig 5.13, panels B and E). We predict ferric iron minerals, in particular goethite (FeOOH) and $Fe(OH)_3$, are the most likely iron precipitates due to the oxidizing conditions within each assay.

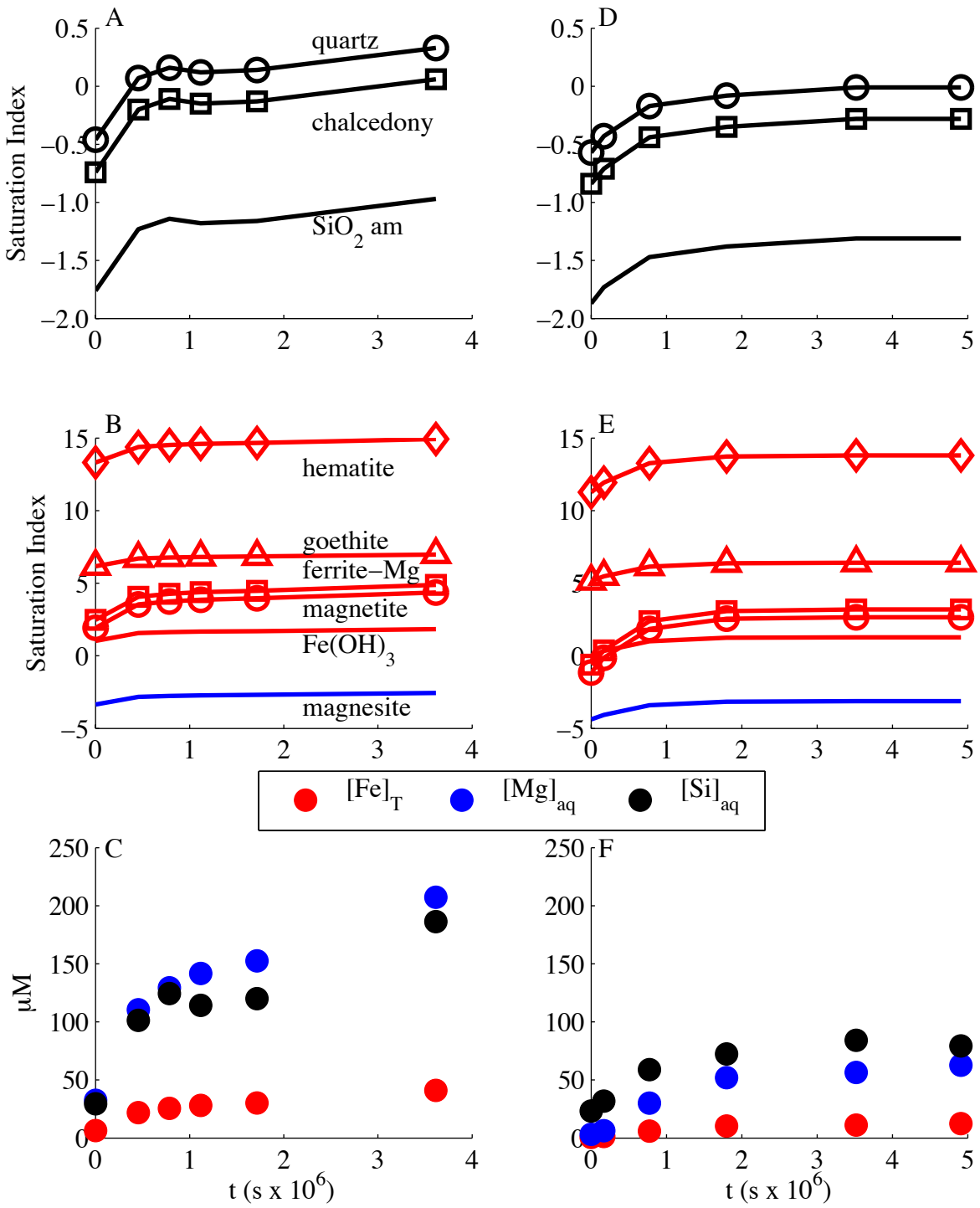

Figure 5.13 Saturation indices (SI) for a selection of mineral phases at or near oversaturation based on the $[Mg]_{aq}$, $[Si]_{aq}$ and predicted $[Fe]_{total}$ for homogeneous assay 3H (panels A-C) and dialysis assay 3D (panels D-F). Silicates are in black, iron bearing minerals are in red, and Mg-phases are in blue, expect for Ferrite-Mg ($MgFe_2O_4$).

Based on the stoichiometry and molar mass of goethite, 41 μM $[Fe]_{total}$ (V_T = 0.36 L) corresponds to 1.3 mg goethite. Assuming the goethite has a density of 3.3 g cm^{-3} and is precipitated as a 1nm thick coating, its maximum surface area would equate to 0.4 m^2 in assay 3H. The predicted, maximum goethite surface area is less for all other assays relative to assay 3H based on the Si dissolution data (see section 5.6 for further discussion).

5.6 Discussion

5.6.1 Abiotic dissolution

We normalized the average abiotic forsterite dissolution rate for all assays to the maximum (5.4 m^2 g^{-1}) and minimum (0.6 m^2 g^{-1}) BET surface area to compare our findings with others. The corresponding abiotic dissolution log rates are -12.1 and -11.1 mol m^{-2} s^{-1}, respectively. Olsen and Rimstidt (2008) predict a log dissolution rate of -10.5 mol m^{-2} s^{-1} at pH 7.5. Pokrovsky and Schott (2000b) measured dissolution log rates from -9.9 to -10.1 at similar pH and aqueous conditions. Wogelius and Walther (1991) determine a log rate of -9.8 for Fo_{91} dissolution at pH 7.4 and standard temperature and pressure (STP). The log rates of abiotic dissolution from this work, while slower by 0.5 to 1 order of magnitude, are on par with the literature values. It is possible that an overall decrease in fine particulates over the course of dissolution, relative to the unreacted forsterite powder (Fig. 5.1) may have altered the total surface area within the early phase of incubation. Furthermore, the high variability in our BET data imparts a large error on the log rate values reported in mol m^{-2} s^{-1}.

It is pertinent to consider abiotic mechanisms of forsterite dissolution to better understand the pathways though which endospores enhance dissolution. The structure of forsterite and other nesosilicates is defined by isolated Si tetrahedra linked though octahedrally coordinated metal ions. This configuration makes them particularly prone to rapid dissolution since breaking weaker Mg-O bonds can undermine the entire mineral structure, releasing both

Mg and Si into solution. At pH < 9 forsterite dissolution is believed to proceed via hydrogen ion attack where two H^+ exchange for Mg^{2+} (Pokrovsky and Schott, 2000a). This mechanism creates an Mg leached and Si rich layer, estimated at < 20 Å thick, where the Si tetrahedra are capable of undergoing dimerization (Pokrovsky and Schott, 2000a, b). Pokrovsky and Schott (2000a) report a pH_{IEP} for fresh Fo_{91} of 4.4. Acid reacted Fo_{91} exhibits a decrease in pH_{IEP} to 2.1, which is similar to that measured for amorphous silica surfaces (Pokrovsky and Schott, 2000a).

5.6.2 Biotic weathering

Both direct, endospore-mineral adhesion and indirect, endospore-ion adsorption enhance forsterite dissolution at pH approximately 7.5 according to Eq. 5.8. The reactive potential of endospore surfaces in our assays is likely due in part to the presence of proton active organic acid moieties. Numerous organic acids and proton active moieties similar to those on the endospore surface are capable of increasing silicate dissolution rates. Olsen and Rimstidt (2008) observed a 6-fold increase in forsterite dissolution in the presence of 1 mM oxalic acid at pH >4.2. Woeglius and Walther measured a 0.75 log unit increase in forsterite dissolution rate in the presence of ascorbic and pthalic acid at pH 4. Pokrovsky et al. (2009) found a wide range of chelators and organic acids capable of enhancing wollastonite ($CaSiO_3$) dissolution, including, but not limited to, chelators such as EDTA, organic acids including citrate and tartrate, and phosphorous ligands in the form of phosphate and metaphosphate. Other research investigating quartz dissolution in the presence of organic acids suggest the formation of both aqueous and surface-bound organo-silicic complexes facilitate quartz dissolution (Bennett, 1991; Bennett et al., 1988).

5.6.2.1 Direct, endospore-forsterite adhesion, dissolution mechanisms

The primary mechanism believed to be responsible for increased silicate dissolution rate in the presence of organic acids is the formation of ligand-mineral surface complexes that lower

the activation energy of dissolution (Bennett et al., 1988; Olsen and Rimstidt, 2008; Pokrovsky et al., 2009). For tectosilicates (SiO_2) these surface complexes must form with mineral surface reactive sites characterized by $Si\text{-}OH_n^{(n-1)}$ groups (Bennett et al., 1988). In silicate minerals containing metal counter ions, aqueous ligands are predicted to complex with metals at the mineral surface (Olsen and Rimstidt, 2008; Pokrovsky et al., 2009). For forsterite, anionic oxygen moieties associated with deprotonated organic acids ($R\text{-}O^-$) can form a reactive complex with Mg exposed at the mineral surface (>Mg, Olsen and Rimstidt, 2008). This complex shifts the electron density from the bridging oxygen in the Si-O-Mg forsterite structure to the >Mg-ligand bond, thereby weakening and ultimately breaking the bridging O bond to form >Mg-O-R and >Si-OH (Olsen and Rimstidt, 2008). For a Si tetrahedral tethered to the mineral structure by only one Si-O-Mg bond, this process would result in the release of Si into solution.

Microbe-mineral adhesion is often discussed in terms of hydrophobic or electrostatic attraction or repulsion between the cell and mineral surface (Yee et al., 2000; Zheng et al., 2001). Parikh and Chorover (2006), however, show that bacterial cell–hematite adhesion involves chemical bond formation between the two surfaces. One of the identified bonds in cell–hematite adhesion is consistent with inner sphere Fe–phosphate or Fe–phosphonate complexation between cell bound phosphate moieties and Fe at the mineral surface. A second reaction, carboxyl protonation, is attributed to cell-bound anionic carboxyl moieties reacting with –OH groups on the mineral surface (Parikh and Chorover, 2006). The inner sphere Fe-phosphate bonds described in cell-hematite adhesion are not unlike the >Mg-O-R complexes attributed to enhanced forsterite dissolution.

Data and models provided in Chapter 4 reveal an affinity for Mg^{2+} adsorption onto the endospore surface at sites $L_{2/4}$, $L_{3/4}$ and $L_{4/4}$. Sites $L_{2/4}$ and $L_{3/4}$ are thermodynamically consistent with phosphate moieties (Chapter 3, Harrold and Gorman-Lewis, 2013) and proton active at the near neutral pH maintained in the forsterite dissolution assays described herein. We propose that direct endospore-forsterite adhesion enhances forsterite dissolution through

the formation of chemical bonds between organic acid moieties, particularly phosphate groups (>P-O^-), and >Mg sites on the endospore and forsterite surfaces, respectively. The formation of >P-O-Mg< complexes acts to lower the activation energy of dissolution as previously described.

The overall surface charge of a particulate plays a large role in dictating colloidal interactions. At pH above 4, the approximate pH_{IEP}, the forsterite surface has a net negative charge. Repulsion between the negatively charged forsterite and endospore surfaces at pH 7.5 likely mitigates the influence of endospore-forsterite adhesion on the dissolution rate. As dissolution progresses and a Si rich surface layer evolves the pH_{IEP} of forsterite drops to 2 (Pokrovsky and Schott, 2000a) and the surface charge at pH 7.5 likely becomes more negative relative to the fresh forsterite surface. Under these conditions it is conceivable that electrostatic repulsion increases between the leached forsterite surface and endospore coat as dissolution progresses, until a steady state leached layer forms. An increase in endospore-forsterite repulsion may contribute to the cessation of biotically enhanced forsterite dissolution observed after approximately 9 days of incubation in the homogeneous assays.

5.6.2.2 Indirect, endospore-ion adsorption dissolution mechanisms

Organic acids can also affect mineral dissolution rates by complexing aqueous dissolution products (Bennett, 1991). This pathway has the potential to enhance dissolution in accordance with Le Chatelier's principle by lowering the activity of dissolution product and pulling the reaction forward as the chemical system attempts to achieve equilibrium. Based on the thermodynamics of forsterite formation and dissolution the Gibbs free energy of dissolution (ΔG_r) is always far from equilibrium under standard temperature and pressure. It is therefore commonly believed that the concentration of aqueous dissolution products does not affect forsterite dissolution rate (Olsen and Rimstidt, 2008; White and Brantley, 1995). This assumption is corroborated by a variety of studies at pH 6.3 (Pokrovsky and Schott, 2000b), 3.8, 2.1 (Rosso and Rimstidt, 2000), and 2 (Oelkers, 2001). Pokrovsky and Schott (2000b),

however, observed that increasing the $[Si]_{aq}$ at pH 9 and 11 inhibits forsterite dissolution due to the formation of a $>Mg\text{-}OH_n^{(n-1)}$ rich surface layer.

We propose that endospore-Mg^{2+} adsorption indirectly enhances the rate of forsterite dissolution due to the removal of aqueous Mg^{2+} from solution. As forsterite dissolved over the first 1-2 days, a steady state, Mg-leached, Si-rich layer likely formed as previously described by Pokrovsky and Schott (2000a) for forsterite dissolution at pH < 9. Si polymerization, however, is most favorable at pH above 7 (Iler, 1979). Consequently, it is possible that the extent of polymerization and depth of the Si-rich, Mg-leached layer reaches a maximum around the pH of dissolution maintained within the assays described herein (~ 7.5). Under these conditions, Mg release, and therefore breakdown of the forsterite structure, could be controlled in part by diffusion of Mg^{2+} through a polymerized, Si-rich layer. Removal of aqueous Mg^{2+} from solution via endospore adsorption increases the chemical gradient between the forsterite dissolution front and bulk solution. This results in an increase in the rate of Mg^{2+} diffusion though the Si-rich layer. As the rate of Mg^{2+} diffusion increases, Si is released from the gel-like layer into solution to maintain a steady state depth. Comparable $[Mg]_{aq}$ in both biotic and abiotic assays despite rapid increases in $[Si]_{aq}$ within the biotic assays is consistent with this theory. Endospore-Mg adsorption is the primary $[Mg]_{aq}$ sink contributing to the observed decrease in Mg:Si ratio with increasing [endospore] in both the homogeneous and dialysis assays (Figs. 5.6 and 5.9).

Endospore adsorption capacity is finite, meaning total Mg^{2+} adsorbed will reach a plateau despite increasing $[Mg^{2+}]_{aq}$ (see Chapter 4). Systems containing mM of Si are capable of enhancing Mg adsorption, potentially though the formation of ternary >Mg-Si-Mg surface complexes (see Chapter 4). $[Si]_{aq}$ observed in forsterite dissolution assays are, however, in the 10^{-6} M range, making it unlikely that Si enhanced Mg adsorption is important in this system. The abrupt cessation of rapid initial dissolution in dialysis as well as homogeneous biotic assays is in accordance with Mg-endospore adsorption reaching a maximum. At the maximum

adsorption potential, endospore surfaces would no longer alter $[Mg]_{aq}$ and the dissolution rate would return to a steady state abiotic dissolution rate as observed after 9 to 12 d of incubation. $[Mg]_{aq}$ in biotic and abiotic, dialysis and homogeneous assays are comparable over the duration of incubation due to Mg-endospore adsorption in the early, rapid dissolution phase. This produces equivalent $[Mg]_{aq}$ chemical gradients in both biotic and abiotic assays after the initial rapid dissolution phase and ultimately enables biotic system to return to an abiotic dissolution rate after cessation of the initial rapid biotic dissolution rate.

According to this mechanism, the dependence of forsterite dissolution rate on the rate of Mg^{2+} diffusion through the Si-rich layer would decrease at pH < 7 where Si polymerization is slower and less favorable and the steady state Si-rich layer would be less polymerized and potentially thinner. The increased activity of H^+ and rate of $2H^+/ Mg^{2+}$ exchange at more acidic pH could further dampen the affect of Mg diffusion on the dissolution rate. In more alkaline solutions (pH > 10) the forsterite surface is characterized by a Mg-hydroxide rich, Si-leached layer (Pokrovsky and Schott, 2000a, b). The influence of $[Mg]_{aq}$ on forsterite dissolution at alkaline pH would likely proceed via a different mechanism.

Endospore-Si adsorption is likely negligible at the ionic strength and pH of our assays (see Chapter 4). Iron oxide precipitates, including the formation of iron oxide coatings on *B. subtilis* cell surfaces, are known to adsorb large amounts of silicic acid at all pH (Fein et al., 2002). The goethite and $Fe(OH)_3$ precipitates predicted to form in all assays (see section 5.4.3) are therefore capable of adsorbing aqueous Si and altering the steady state of the system. A decrease in the activity of aqueous Si could act to destabilize the Mg-leached, Si-rich layer at the forsterite surface and further enhance dissolution. By this mechanism the rate of dissolution would also change as a function of endospore concentration since total iron precipitation will likely increase with the overall mineral dissolution rate. An abundance of negatively charged, endospore surfaces could also support the formation of thin iron oxide coatings (Fein et al., 2002) that maximize the reactive surface area of iron precipitates.

5.7 Conclusions

B. subtilis endospore surface reactivity enhances the rate of forsterite dissolution through both direct and indirect pathways. Direct pathways likely involve the formation of >P-O-Mg< chemical bonds during microbe-mineral adhesion, which destabilize forsterite by lowering the activation energy of dissolution. Endospore-Mg adsorption enhances dissolution via an indirect pathway by lowering the activity of $[Mg^{2+}]_{aq}$ and increasing the chemical gradient between the dissolving mineral front and bulk solution. This increases Mg^{2+} diffusion though an Mg-leached, Si-rich layer thereby enhancing the rate of dissolution. The influence of both indirect and direct rate determining mechanisms is dependent on the concentration of endospores in solution. Forsterite dissolution in dialysis assays returns to an abiotic rate when endospore-Mg^{2+} adsorption reaches a maximum. Homogeneous assays also return to an abiotic rate when endospore-mineral adhesion becomes unfavorable. A third mechanism, involving Si adsorption onto trace iron oxide precipitates may also contribute to enhanced dissolution in the assays described herein.

While there are chemical variations between the surface chemistry of *B. subtilis* endospores and vegetative cells, the pH range and proton adsorption capacity of both surfaces are very similar (Fein et al., 2005; Gorman-Lewis et al., 2006; Harrold and Gorman-Lewis, 2013). This suggests the presence of similar surface bound organic acid moieties and cation adsorption potential (Chapter 4; Borrok et al., 2004; Harrold and Gorman-Lewis, 2013). Further parallels between cell and endospore surface reactivity include a negligible affinity for Si adsorption (see Chapter 4; Fein et al., 2002). Findings by Borrok et al. (2005) show 36 bacterial species, including *B. subtilis* vegetative cells, exhibit remarkably similar surface reactivities. Based on these lines of evidence the endospore surface serves as a first-order proxy for the surfaces of a wide range of vegetative bacterial cells. We conclude that bacterial surface reactivity has the capacity to influence olivine chemical weathering rates. The affect on chemical

weathering rates would be most pronounced in microbe-water-rock systems that support a large microbial biomass. Cell surface promoted mineral dissolution may also benefit microbes in environments with trace nutrient deficiencies.

5.8 References

Bargar, J.R., Tebo, B.M., Villinski, J.E., 2000. In situ characterization of Mn(II) oxidation by spores of the marine Bacillus sp strain SG-1. Geochimica Et Cosmochimica Acta 64, 2775-2778.

Bennett, P., Rogers, J., Choi, W., Hiebert, F., 2001. Silicates, Silicate Weathering, and Microbial Ecology. Geomicrobiology Journal 18, 3-19.

Bennett, P.C., 1991. Quartz dissolution in organic-rich aqueous systems. Geochimica et Cosmochimica Acta 55, 1781-1797.

Bennett, P.C., Melcer, M.E., Siegel, D.I., Hassett, J.P., 1988. The dissolution of quartz in dilute aqueous solutions of organic acids at 25°C. Geochimica et Cosmochimica Acta 52, 1521-1530.

Berner, R.A., Lasaga, A.C., Garrels, R.M., 1983. The carbonate-silicate geochemical cycle and its effect on atmospheric carbon dioxide over the past 100 million years. American Journal of Science American Journal of Science 283, 641-683.

Borrok, D., Fein, J.B., Kulpa, C.F., 2004. Proton and Cd adsorption onto natural bacterial consortia: Testing universal adsorption behavior. Geochimica Et Cosmochimica Acta 68, 3231-3238.

Borrok, D., Turner, B.F., Fein, J.B., 2005. A universal surface complexation framework for modeling proton binding onto bacterial surfaces in geologic settings. Am J Sci 305, 826-853.

Borrok, D.M., Fein, J.B., 2005. The impact of ionic strength on the adsorption of protons, Pb, Cd, and Sr onto the surfaces of Gram negative bacteria: testing non-electrostatic, diffuse, and triple-layer models. Journal of Colloid and Interface Science 286, 110-126.

Daughney, C.J., Fowle, D.A., Fortin, D., 2001. The effect of growth phase on proton and metal adsorption by Bacillus subtilis. Geochimica Et Cosmochimica Acta 65, 1025-1035.

De Vrind, J.P.M., De Vrind-De Jong, E.W., De Voogt, J.-W., H., Westbroek, P., Boogerd, F.C., Rosson, R.A., 1986. Manganese oxidation by spores and spore coats of a marine *Bacillus* species. Applied and Environmental Microbiology 52, 1096-1100.

Ehrlich, H.L., 1996. How microbes influence mineral growth and dissolution. Chemical Geology 132, 5-9.

Fein, J.B., Boily, J.-F., Yee, N., Gorman-Lewis, D., Turner, B.F., 2005. Potentiometric titrations of Bacillus subtilis cells to low pH and a comparison of modeling approaches. Geochimica et Cosmochimica Acta 69, 1123-1132.

Fein, J.B., Scott, S., Rivera, N., 2002. The effect of Fe on Si adsorption by Bacillus subtilis cell walls: insights into non-metabolic bacterial precipitation of silicate minerals. Chemical Geology 182, 265-273.

Gorman-Lewis, D., Fein, J.B., Jensen, M.P., 2006. Enthalpies and entropies of proton and cadmium adsorption onto Bacillus subtilis bacterial cells from calorimetric measurements. Geochimica et Cosmochimica Acta 70, 4862-4873.

Harrold, Z.R., Gorman-Lewis, D., 2013. Thermodynamic analysis of Bacillus subtilis endospore protonation using isothermal titration calorimetry. Geochimica et Cosmochimica Acta 109, 296-305.

Harrold, Z.R., Hertel, M.R., Gorman-Lewis, D., 2011. Optimizing Bacillus subtilis spore isolation and quantifying spore harvest purity. Journal of Microbiological Methods 87, 325-329.

Iler, R.K., 1979. The chemistry of silica : solubility, polymerization, colloid and surface properties, and biochemistry. Wiley, New York.

Kohler, P., Hartmann, J., Wolf-Gladrow, D.A., 2010. Geoengineering potential of artificially enhanced silicate weathering of olivine. Proceedings of the National Academy of Sciences 107, 20228-20233.

Lee, J.-U., Fein, J.B., 2000. Experimental study of the effects of Bacillus subtilis on gibbsite dissolution rates under near-neutral pH and nutrient-poor conditions. Chemical Geology 166, 193-202.

Mandernack, K.W., Post, J., Tebo, B.M., 1995. Manganese mineral formation by bacterial-spores of the marine *Bacillus*, strain SG-1 - Evidence for the direct oxidation of Mn(II) to Mn(IV). Geochimica Et Cosmochimica Acta 59, 4393-4408.

Marczenko, Z., 1976. Spectrophotometric determination of elements. E. Horwood ; Halsted Press, Chichester, Eng.; New York.

Morris, M.C. et. al., 1984. Standard x-ray diffraction powder patterns. Monograph 25, Section 20. U.S. Dept. of Commerce, National Bureau of Standards : For sale by the Supt. of Docs., U.S. G.P.O., Washington, DC, 71

Nagy, K.L., Lasaga, A.C., 1992. Dissolution and precipitation kinetics of gibbsite at 80 deg C and pH 3: The dependence on solution saturation state. Geochimica et Cosmochimica Acta 56, 3093-3111.

Ngwenya, B.T., Magennis, M., Olive, V., Mosselmans, J.F.W., Ellam, R.M., 2009. Discrete Site Surface Complexation Constants for Lanthanide Adsorption to Bacteria As Determined by Experiments and Linear Free Energy Relationships. Environmental Science & Technology 44, 650-656.

Oelkers, E.H., 2001. An experimental study of forsterite dissolution rates as a function of temperature and aqueous Mg and Si concentrations. Chemical Geology 175, 485-494.

Olsen, A.A., Rimstidt, D.J., 2008. Oxalate-promoted forsterite dissolution at low pH. Geochimica et Cosmochimica Acta 72, 1758-1766.

Omer, M., Elbadawi, A., Yassin, O., 2013. Synthesis and Structural Properties of MgFe2O4 Ferrite Nano-particles. Journal of Applied and Industrial Sciences 1, 20-23.

Parikh, S.J., Chorover, J., 2006. ATR-FTIR Spectroscopy Reveals Bond Formation During Bacterial Adhesion to Iron Oxide. Langmuir 22, 8492-8500.

Phoenix, V.R., Konhauser, K.O., Ferris, F.G., 2003. Experimental study of iron and silica immobilization by bacteria in mixed Fe-Si systems: implications for microbial silicification in hot springs. Canadian Journal of Earth Sciences 40, 1669-1678.

Pokrovsky, O.S., Schott, J., 2000a. Forsterite surface composition in aqueous solutions: a combined potentiometric, electrokinetic, and spectroscopic approach. Geochimica et Cosmochimica Acta 64, 3299-3312.

Pokrovsky, O.S., Schott, J., 2000b. Kinetics and mechanism of forsterite dissolution at 25Â°C and pH from 1 to 12. Geochimica et Cosmochimica Acta 64, 3313-3325.

Pokrovsky, O.S., Shirokova, L.S., Bezeneth, P., Schott, J., Golubev, S.V., 2009. Effect of organic ligands and heterotrophic bacteria on wollastonite dissolution kinetics. American Journal of Science 309, 731-772.

Rogers, J.R., Bennett, P.C., 2004. Mineral stimulation of subsurface microorganisms: release of limiting nutrients from silicates. Chemical Geology 203, 91-108.

Rosso, J.J., Rimstidt, J.D., 2000. A high resolution study of forsterite dissolution rates. Geochimica et Cosmochimica Acta 64, 797-811.

Sacks, L.E., Alderton, G., 1961. Behavior of bacterial spores in aqueous polymer two-phase systems. Journal of Bacteriology 82, 331-341.

Setlow, B., Loshon, C., Genest, P., Cowan, A., Setlow, C., Setlow, P., 2002. Mechanisms of killing spores of Bacillus subtilis by acid, alkali and ethanol. Journal of Applied Microbiology 92, 362-375.

Setlow, P., 2006. Spores of *Bacillus subtilis*: their resistance to and killing by radiation, heat and chemicals. Journal of Applied Microbiology 101, 514-525.

Siala, A., Hill, I.R., Gray, T.R.G., 1974. Populations of Spore-forming Bacteria in an Acid Forest Soil, with Special Reference to Bacillus subtilis. J Gen Microbiol 81, 183-190.

Song, W., Ogawa, N., Oguchi, C.T., Hatta, T., Matsukura, Y., 2007. Effect of Bacillus subtilis on granite weathering: A laboratory experiment. CATENA 70, 275-281.

Stumm, W., 1990. Aquatic chemical kinetics : reaction rates of processes in natural waters. Wiley, New York.

Vandevivere, P., Welch, S.A., Ullman, W.J., Kirchman, D.L., 1994. Enhanced Dissolution of Silicate Minerals by Bacteria at Near-Neutral pH. Microbial Ecology 27, 241-251.

White, A.F., Brantley, S.L., 1995. Chemical weathering rates of silicate minerals. Mineralogical Society of America, Washington, D.C.

Whitman, W.B., Coleman, D.C., Wiebe, W.J., 1998. Prokaryotes: The unseen majority. Proceedings of the National Academy of Sciences 95, 6578-6583.

Wightman, P.G., Fein, J.B., 2004. The effect of bacterial cell wall adsorption on mineral solubilities. Chemical Geology 212, 247-254.

Wogelius, R.A., Walther, J.V., 1991. Olivine dissolution at 25 deg C: Effects of pH, CO2, and organic acids. Geochimica et Cosmochimica Acta 55, 943-954.

Yee, N., Fein, J.B., Daughney, C.J., 2000. Experimental study of the pH, ionic strength, and reversibility behavior of bacteria-mineral adsorption. Geochimica et Cosmochimica Acta 64, 609-617.

Zheng, X., Arps, P.J., Smith, R.W., 2001. Adhesion of two bacteria onto dolomite and apatite: their effect on dolomite depression in anionic flotation. International Journal of Mineral Processing 62, 159-172.

Chapter 6: Conclusions

Microbial biomass plays a critical role in the movement and cycling of dissolved ions through the environment. Divulging how and to what extent microbe-ion interactions drive low-temperature aqueous geochemical processes is instrumental to our understanding of water-rock systems. Microbe-ion adsorption is one such pathway capable of influencing the activity of aqueous major and trace ions. Most investigations focus on the adsorption behavior of trace metals onto vegetative bacterial cell surfaces. The surface reactivity of endospores, however, is poorly constrained. Furthermore, the effect of microbial surface reactivity on major ion activities and primary silicate dissolution rates is a widely unstudied phenomenon with potentially large geochemical impacts. This dissertation develops a method for generating a pure endospore biomass that enables focused experimentation regarding endospore surface reactivity in water-rock systems. Endospore surface reactivity is quantified and modeled to produce a robust thermodynamic definition of discrete adsorption sites. We then test the ability for endospore adsorption to impact the activities of two major ions found in forsterite, Mg and Si. Finally, endospores are utilized as a first-order proxy to isolate the influence of microbial surface reactivity on the rate of forsterite dissolution. Together this body of work fills in numerous knowledge gaps regarding microbial surface reactivity and advances our understanding of microbe-mineral interactions.

The culturing methods described in Chapter 2 successfully induce *Bacillus subtilis* sporulation and produce milligrams of endospore biomass free of vegetative cell residue. Further purification is achieved using a refined version of the two-phase separatory solution described by Sacks and Alderton (1961). A semi-automated process for determining the purity of the final endospore biomass provides a method that enables quality control. These methods are published in the Journal of Microbiological Methods (Harrold et al., 2011). Together, the

methods described in Chapter 2 enable experimentation critical to investigating the surface reactivity of *B. subtilis* endospores and understanding their influence on geochemical processes.

Chapter 3 provides the most robust analysis of endospore surface reactivity to date. Data include synchronized potentiometric titration and isothermal titration calorimetry (ITC) data corresponding to *B. subtilis* endospore surface protonation from pH 3 to 9. Results show net endospore proton adsorption is exothermic and occurs over the entire pH range studied. We model the potentiometric titration data according to non-electrostatic surface complexation theory, which defines surface protonation according to balanced chemical equations describing discrete proton active sites. A four-site non-electrostatic surface complexation model (NE-SCM) provides the best fit to the potentiometric titration results but fails to describe the ITC data. To remedy this discrepancy we use a five-site NE-SCM to describe both the potentiometric titration and ITC data. A significantly better fit to the highly sensitive ITC data justifies the use of a five-site model despite being under-constrained by the potentiometric titration results. Conducting simultaneous potentiometric titration and ITC analyses is a novel approach to investigating microbial surface reactivity that provides a more robust thermodynamic definition of surface reactivity than the individual analyses. The NE-SCMs describing endospore surface protonation herein include site concentrations, equilibrium constants, enthalpies, entropies and the Gibbs free energy of protonation for discrete proton active sites on the endospore surface. Site-specific thermodynamics of endospore protonation suggest the presence of reactive carboxyl, phosphate and thiol groups on the endospore surface. Hydroxyl, phenol or amine groups may contribute to proton adsorption at high pH (> 7.5). Endospore adsorption capacity and behavior is comparable to their vegetative cell counterpart suggesting similar organic acid moieties are responsible for endospore and cell surface adsorption. This research is published in Geochimica et Cosmochimica Acta (Harrold and Gorman-Lewis, 2013) and enables quantitative analysis of environmentally relevant endospore-ion interactions in both laboratory and macro-scale systems.

Chapter 4 investigates *B. subtilis* endospore Mg and Si adsorption over a wide range of pH and adsorbent to adsorbate ratios as well as adsorption behavior in aqueous systems containing both Mg and Si. Despite exhibiting both hydrophobic and hydrophilic surface properties, Si adsorption to the endospore surface is negligible under all pH and endospore to adsorbate ratios studied. This behavior is similar to that observed for *B. subtilis* vegetative cells (Fein et al., 2002). Mg-endospore adsorption however, increases with increasing pH, $[Mg]_{total}$ and $[Si]_{total}$. pH dependent Mg adsorption likely increases with increasing pH as organic acid moieties on the endospore surface sequentially deprotonate and expose anionic oxygen ligands capable of complexing Mg^{2+}. Increasing the $[Mg]_{total}$ to endospore ratio increases adsorption until maximum adsorption is achieved and the adsorption edge plateaus. We modeled pH dependent Mg adsorption according to the 4-site NE-SCM described in Chapter 3. Both 1_{site}:1_{Mg} and 2_{site}:1_{Mg} stoichiometric adsorption onto sites $L_{2/4}$, $L_{3/4}$ and $L_{4/4}$ provided a good fit to the data. These models were then fit to the adsorption data from variable adsorbate to adsorbent ratio assays at pH approximately 7.2. The 1_{site}:1_{Mg} stoichiometry model provided a good fit to the low $[Mg]_{total}$ data but failed to describe the adsorption plateau. A 2_{site}:1_{Mg} adsorption stoichiometry was able to describe the adsorption plateau but not the low $[Mg]_{total}$ data. It is possible that both 1_{site}:1_{Mg} and 2_{site}:1_{Mg} adsorption stoichiometry contribute to overall Mg-endospore adsorption behavior. Systems containing both Mg and Si do not appreciably enhance Si adsorption. However, increases in $[Si]_{total}$ enhance Mg adsorption. It is possible that ternary >Mg-Si-Mg complexes are responsible for enhanced Mg adsorption in the presence of Si. Assuming ternary complexes form, the concomitant increase in Si adsorption is within the analytical error of the Si data, rendering it undetectable. Findings from Chapter 4 suggest endospore–Mg and –Si adsorption behavior is similar to that of their vegetative cell counterpart. Endospores are more likely to affect low-temperature aqueous geochemical systems through direct Mg-endospore adsorption than direct Si-endospore adsorption. Their

adsorptive influence on [Si] is likely restricted to the formation of ternary metal-Si complexes. These interactions are particularly relevant to mineral dissolution and precipitation processes involving Mg and Si.

The metabolic dormancy and structural integrity of endospores in oligotrophic environments makes them an ideal candidate for studying the influence of microbial surfaces on low-temperature aqueous geochemical processes. Chapter 5 explores the affect of microbial surfaces on the rate of forsterite dissolution at near-neutral pH by using *B. subtilis* endospores as a first order proxy for vegetative cell surfaces. Dialysis and homogeneous assays isolate the affects of both direct and indirect dissolution pathways corresponding to microbe-mineral adhesion and microbe-ion adsorption, respectively. The initial rate of forsterite dissolution increases in the presence of endospores in both dialysis and homogeneous assays. Dissolution rates return to an abiotic steady state rate after the initial rapid biotic dissolution phase. The initial biotic dissolution rate components for both indirect and direct dissolution pathways correlate with endospore concentration and are modeled according to a simplified rate law. Endospore-ion adsorption likely enhances dissolution by adsorbing Mg and increasing the chemical gradient across a Si-rich, Mg-leached layer that acts as a diffusion barrier between the forsterite dissolution front and bulk solution at near-neutral pH. Mg-endospore adsorption data provided in Chapter 4 and Mg:Si ratios below stoichiometric forsterite dissolution in biotic assays support this theory. Direct endospore-forsterite adsorption may include the formation of Mg-phosphate bonds between the endospore and mineral surfaces. These bonds can shift electron density within the mineral structure, destabilizing the forsterite and ultimately leading to enhanced dissolution. Based on these findings, microbial surface reactivity is capable of influencing the rate of primary silicate dissolution in microbe-water-rock systems at near-neutral pH.

This dissertation provides the first detailed thermodynamic models describing endospore surface reactivity and enabling comparison to their vegetative cell counterpart. The

influence of direct *B. subtilis* endospore adsorption on major element activities is most likely associated with major cation adsorption and, to a much lesser extent, Si adsorption. Ternary metal-Si complexes are the most likely mechanism driving Si-endospore adsorption in aqueous systems. These reactions have implications regarding microfossil formation and preservation. In low-temperature aqueous geochemical systems *B. subtilis* endospore-Mg adsorption and mineral adhesion are capable of enhancing forsterite dissolution at near-neutral pH. Although a broad understanding of bacterial endospore coat reactivity across species and genera is still lacking, this work illustrates the fundamental influence endospores can have on geochemical reactions and provides an investigative model for future studies. Based on the commonalities between *B. subtilis* endospore and vegetative cell surface reactivity, it is possible that a wide range of microbial cells are capable of enhancing primary mineral dissolution rates through surface mediated pathways. This suggests that the mere presence of microbes is capable of manipulating fundamental geochemical processes, regardless of their metabolic activity.

References

Fein, J.B., Scott, S., Rivera, N., 2002. The effect of Fe on Si adsorption by Bacillus subtilis cell walls: insights into non-metabolic bacterial precipitation of silicate minerals. Chemical Geology 182, 265-273.

Harrold, Z.R., Gorman-Lewis, D., 2013. Thermodynamic analysis of Bacillus subtilis endospore protonation using isothermal titration calorimetry. Geochimica et Cosmochimica Acta 109, 296-305.

Harrold, Z.R., Hertel, M.R., Gorman-Lewis, D., 2011. Optimizing Bacillus subtilis spore isolation and quantifying spore harvest purity. Journal of Microbiological Methods 87, 325-329.

Sacks, L.E., Alderton, G., 1961. Behavior of bacterial spores in aqueous polymer two-phase systems. Journal of Bacteriology 82, 331-341.